**UNIVERSITÀ DEGLI STUDI DI PARMA**

*Dottorato di Ricerca in Tecnologie dell'Informazione*

*XXIX Ciclo*

# Automated IMU-based Motion Analysis for Clinical Applications: the Parkinson's Disease and Post-stroke Cases

Coordinatore:

*Chiar.mo Prof. Marco Locatelli*

Tutor:

*Chiar.mo Prof. Gianluigi Ferrari*

Dottorando: *Federico Parisi*

Dicembre 2016

*To the ones that provided,*
*to the ones that inspired,*
*to curiosity.*

# Table of Contents

# List of Figures

# List of Tables

# Introduction

*Technology is nothing.*
*What's important is that you have a faith in people, that they're basically good and smart, and if you give them tools, they'll do wonderful things with them.*

– Steve Jobs

Motion is a fundamental component of our everyday life. Population ageing, in place especially in the developed countries in the last decades, has made increasingly present the issues related to elderly people's mobility as preserving the ability to move without difficulties and independently is crucial for maintaining a good life quality level. Therefore, the interest of the scientific community in motor-impairing diseases which are more likely to occur in the elderly population, such as Parkinson's Disease (PD) and stroke, has grown steadily in recent years.

The analysis of motor performance is a key aspect of many clinical assessment processes but often clinicians can rely only of qualitative analysis and on their experience. Technology can contribute consistently in helping medical personnel to provide more accurate and reliable diagnoses and to define more effective therapies. Human motion analysis techniques, for example, are often used in clinical applications to quantitatively characterize patients' movements during specific motor tasks. Classical motion analysis systems, based on optical, magnetic, or mechanic technologies, are accurate and reliable but, on the other hand, they are expensive, require external infrastructures and specifically trained personnel. Inertial Measurement Units (IMUs)-based motion analysis systems are lately becoming the most adopted alter-

native because they are easy-to-use, flexible, cost-effective, unobtrusive and can be used in free living environment.

In this thesis, a unified approach, relying on IMU-based motion sensing, has been used to develop a system for the automatic assessment of functional motor tasks, with particular focus on gait, in both PD [1, 2, 3, 4] and post-stroke [5] populations. The proposed systems have been designed to be: (i) low-cost and low complexity, using Body Sensor Networks (BSNs) formed by only few inertial nodes; (ii) accurate and objective in the kinematic characterization of specific motor tasks (validation of the developed algorithms through comparison with gold standard technologies); (iii) "smart", exploiting machine learning techniques for providing motor performance automatic scoring, which mimic clinicians' evaluation criteria, together with meaningful high level and aggregate information; (iv) tele-health ready, being suitable for remote and long-term monitoring of patients outside the clinics. The results obtained in both systems demonstrate that IMU-based motion analysis, especially when supported by machine learning techniques, represents a powerful tool for enhancing the quality of the clinical assessment process both within and outside the clinics.

# Chapter 1

# IMU-based Motion Analysis for clinical applications

*I move, therefore I am.*

– Haruki Murakami

## 1.1 Motion Analysis

The study of motion has always been fascinating topic. It is an interdisciplinary subject, involving not only scientific disciplines, such as mathematics, physics, geometry, and medicine, but also philosophy and arts. As for many modern sciences, the early attempts to describe in a logical and organized way animals' movement began in ancient Greece. Aristotle (384-322 B.C.) is universally recognized as the "Father of Kinesiology" (i.e., the science of human motion) and the first biomechanist. In his book "De Motu Animalium" (On the Movement of Animals), he described locomotion in the animal kingdom, the mechanisms of gait and the geometrical action of muscles. During the Roman Empire, Claudius Galen gained a deep knowledge of human body and motion practicing surgery on gladiators and wrote the "On the Func-

tion of the Parts", the first book on physiology, which stayed as the world's standard medical text for the next 1,400 years.

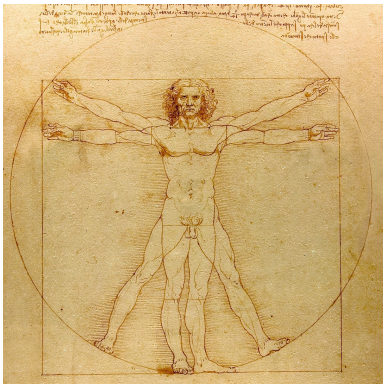

Figure 1.1: Vitruvian Man by Leonardo Da Vinci (∼1490)

No further progression was made until the Renaissance, when Leonardo da Vinci (1452-1519) described human anatomy and motion as mechanical systems including soft tissue, joints, muscles, bones, ligaments, tendons, and cartilage (Figure 1.1). Few years later, Andrea Vesalius (1524-1564) published "De Humani Corporis Fabrica Libri Septem" (On the Structure of the Human Body), in which he debated and reformulated the theories by Galen, arousing new interest in the study of the human body. Galileo Galilei (1564-1643), father of the scientific method, was also interested in biomechanics and derived insights on the bones' structure and allometry (i.e., the science that studies change in organisms in relation to proportional changes in body size).

Following the principles set by Galileo, Giovanni Alfonso Borelli (1608- 1679) began his investigation into the science of animal movements around 1657. He achieved important scientific results, such as the first experiments in gait analysis, the determination of the human center of gravity position, and the concept of the musculoskeletal system as a set of levers that magnified motion rather than force (many years before Newton actually produced his laws of motion). These achievements were collected in his great treatise called, in honor of Aristotle's work, "De Motu Animalium" [6], and make him the key figure of modern biomechanics (Figure 1.2).

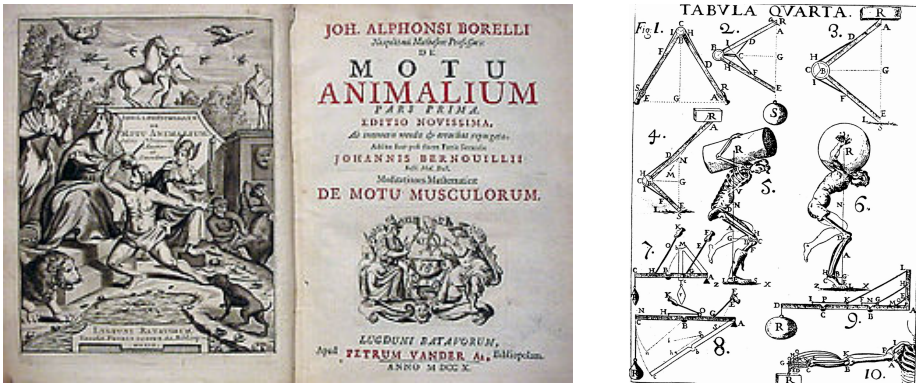


(a) (b)

Figure 1.2: Borelli's treatise "De Motu Animalium": (a) Cover and (b) an extract table on leg joints.

In the following centuries, few sporadic contributions were given to the field. In 19th century, the advent of photography and cinematography laid the foundation for modern motion analysis. Some of notable names of this period were: the Weber brothers, who pioneered today's gait analysis; the French astronomer Pierre Janssen (1824-1907), who invented a multi-exposure camera for chronophotographic experiments, allowing a recording of several phases of motion in the same photo; Étienne-Jules Marey (1830-1904), who first correlated ground reaction forces with movement and accurately record the progression of the human limbs while walking (Figure 1.3 (a)); Eadweard Muybridge, known for his pioneering work on animal locomotion (Figure 1.3 (b)); Christian Wilhelm Braune and his student Otto Fischer, who conducted research involving the position of the center of gravity in the human body and its various segments and advanced the studies on human gait (Figure 1.3 (c)).

Starting from the 20th century, biomechanics became a worldwide recognized discipline and, driven by advances in technology, it has constantly evolved to present days. In the following section, the main approaches used nowadays for human motion analysis are further described.

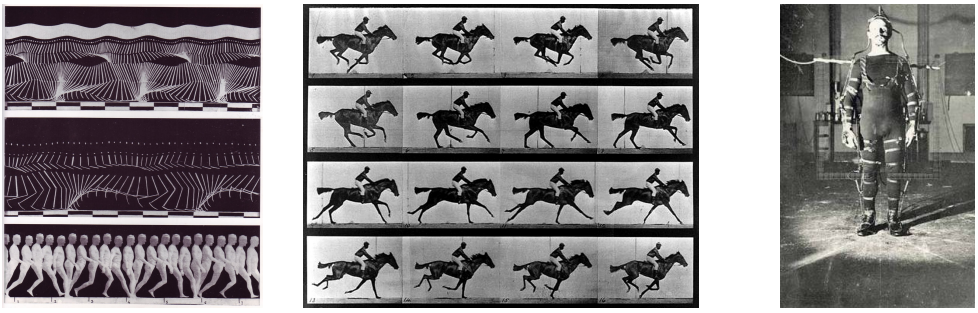

(a) (b) (c)

Figure 1.3: Motion Analysis in 19th century: (a) Marey's studies on human gait using chronophotography; (b) the famous "Horse in Motion" picture by Eadweard Muybridge (1886); (c) the first 3D gait analysis system by Braune and Fischer.

### 1.1.1 Human Motion Analysis Technologies

Many different methods for tracking and analyzing motion are currently available. In general, the process of recording movements of objects or people through technological tools is commonly known as *Motion Capture* (mo-cap). Mo-cap systems are based on various technologies and are used in several contexts. The study of human motion in biomedical applications has always been the leading sector for motion capture: the first modern mo-cap systems used photogrammetric analysis for characterizing body movements and then, as the technology matured, they were applied to different fields, such as military, entertainment, sports, and robotics.

#### Optical Mo-cap

The most commonly used mo-cap approach, more than 150 years after Marey's studies, is still based on optical devices. Optical-based systems rely on the data acquired by two or more calibrated image sensors in order to compute the position of an object or a subject in a 3-dimensional space. To achieve this goal, cameras are used in conjunction with specific markers attached to the moving body.

Markers can be passive or active. In the first case, markers are coated with a retroreflective material and reflects the light (generally in the infrared spectrum) generated

(a)

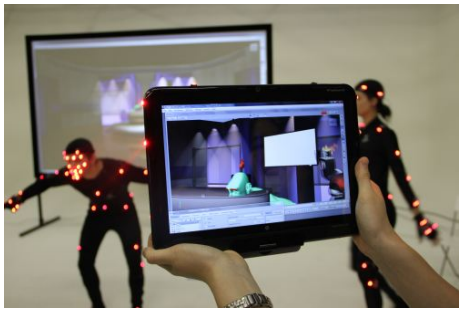

(b)

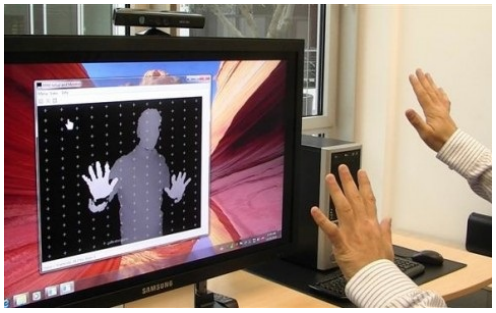

(c)

Figure 1.4: Optical Mo-cap: (a) a passive marker-based system by Vicon Motion Systems Ltd. (UK, `http://www.vicon.com`); (b) a system based on active markers by PhaseSpace Inc. (CA, USA, `http://www.phasespace.com`); (c) hands tracking using a Kinect device by Microsoft (WA, USA, `http://www.microsoft.com`).

by sources placed in correspondence to cameras lens. A variable amount of cameras (from 2 to 300 or more) captures images in which markers appear as bright dots on a dark background. By processing these images and using triangulations techniques it is possible to derive the 3D position of each marker in a calibrated volume. Since all markers have the same aspect on the acquired images, this approach is often subject to the problem of marker swapping, which can be partially reduced using proper software tools and manual clean-up of the data. Nevertheless, an accuracy of 1 mm with a limited number of cameras can be easy reached. An example of commercial passive marker-based mo-cap systems is shown in Figure 1.4 (a). In the active marker case,

the light source is placed directly on the markers, which often are LEDs emitting (colored) visible or infrared light. The cameras infrastructure detects the makers correspondence in multiple images and triangulates the relative positions of each point. This approach is more reliable and stable because the light generated by LEDs can be tuned in order be easily picked up by cameras, enabling them to reach accuracies in the order of 0.1 mm within the calibrated volume. A commercial active-marker system for motion capture is shown in Figure 1.4 (b). In general, marker-based optical mo-cap is considered the gold standard in motion capture because it is highly accurate, minimally intrusive, and adaptable to different applications. The main disadvantages of this approach are: (i) the need of an external infrastructure and specifically trained personnel, which limit its usability in a non-structured environment; (ii) its complexity and high cost; (iii) the long time required for setup, calibration, and data cleaning procedures.

Lately, different techniques for reconstructing motion from images without the need of wearing special equipment for tracking have appeared. These systems are based mostly on the use of structured light patterns (e.g., the Kinect by Microsoft, shown in Figure 1.4 (c)), stereoscopy or depth cameras. Although marker-less system are more affordable and flexible than the marker-based systems, the performance achieved by these methods is still not comparable with state of the art approaches. Finally, further limitations that both categories of optical mo-cap share is the sensitivity to light conditions and occlusions, which can generate artifacts, and the need to stay within the limited volume of space that the cameras can capture.

### Non-optical Mo-cap

Many alternatives to optical mo-cap system are available, which usually tend to sacrifice some accuracy in favor of higher flexibility and usability. Some of the non-optical technologies used for motion capture are described in the following list:

- *Electromechanical*: exoskeletons/armatures worn over the subject which can measure directly joint angles and body relative motion through rods connected by potentiometers. These kind of systems are real-time, relatively low-cost,

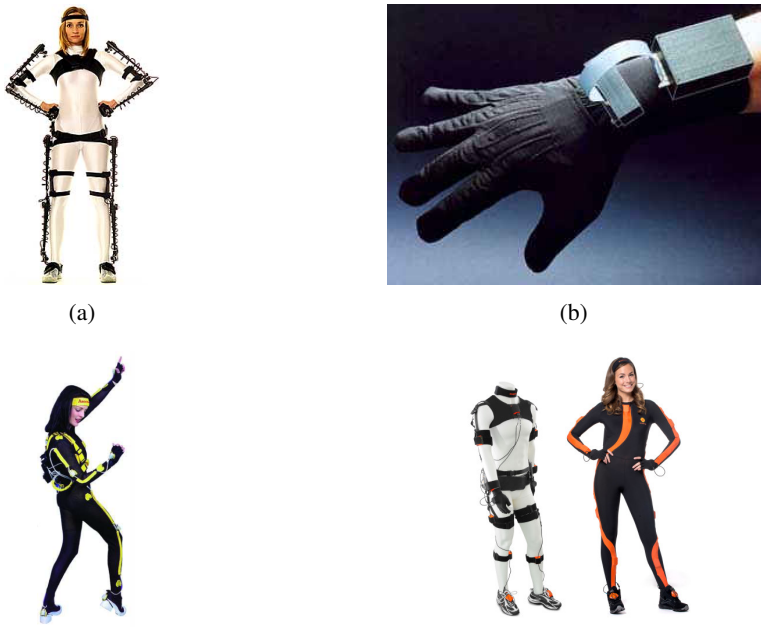

(a) (b)

(c) (d)

Figure 1.5: Alternatives to optical mo-cap: (a) the Gypsy 7 mechanical suite and (b) the 5DT Data Glove 14 Ultra, both by Meta Motion (CA, USA, `http://www.metamotion.com`); (c) the MotionStar magnetic system by Ascension Technology Corp. (VT, USA, `http://www.ascension-tech.com`); (d) the Xsens MVN inertial mo-cap suite (The Netherlands, `http://www.xsens.com`).

free-of-occlusion, and highly-accurate but are also sensitive to soft tissue artifacts, can limit the user's movements, they require to be calibrated for each subject, and have problems to reconstruct the motion of joints with multiple degree of freedom (e.g., the shoulder). An example of a mechanical motion capture system is shown in Figure 1.5 (a).

- *Optical Fiber*: flexible optical fibers are attached to the subject; body movements bend the fibers, inducing an attenuation in the light measured by the fiber-optic sensors, which is proportional to the movement amplitude. This technique permits real-time and inexpensive data acquisition, but it is suitable for capturing only the motion of limited parts of the body, such as the hands

(see Figure 1.5 (b)).

- *Electromagnetic*: body-worn magnetic sensors measure the changing in the flux of a magnetic field (usually formed by three orthogonal coils) generated by a transmitter. By measuring the relative intensity of the voltage or current of the three coils, it is possible to measure positions and orientations of the wearable trackers with a good level of accuracy. The main limitations of this technology are the limited capture volume, the high cost, and the interference problems caused by proximity of ferromagnetic materials. A commercial electromagnetic mo-cap system is shown in Figure 1.5 (c).

- *Acoustic*: triangulation of sonic or ultrasonic sound waves time-of-flight is used to measure the distance between acoustic pulse transmitters and receivers attached to the user's body at different time instants. Acoustic mo-cap systems are low-cost, flexible, and not obtrusive but, due to the physics of sound waves, they require to have a line-of-sight between emitters and receivers, are susceptible to interference (echoing effects), have a low transmission rate, and a limited measurement accuracy.

- *Inertial*: a variable amount of IMUs, equipped with 3-dimensional accelerometers, gyroscopes, and often magnetometers, are attached to rigid segments of the user's body, through Velcro straps or using specific Lycra suites. Exploiting biomechanical models and sensor fusion, the position and the orientation of monitored segments can be derived, usually building a skeleton model of the subject. Additional details about IMUs and inertial data processing are provided in Section 1.2. Inertial-based solutions are becoming the second most popular mo-cap technology, after optical systems, because they allow the collection of motion data in a variety of non-structured environments, they are self-contained, cost-effective, portable, and easy-to-use. The main drawbacks of this approach are related to noise and drift phenomena, which can lower the accuracy of the measures on the long period. In Figure 1.5 (d), a commercial product for full-body inertial mo-cap is shown.

- *Hybrid*: all the methods described so far have both advantages and disadvantages. In order to overcome the drawbacks of a specific technology and provide more robust and accurate measurements, hybrid approaches, which combine two or more of the previously described sensing methods, have recently been proposed. Example of hybrid systems are based on the combination of optical and inertial [7, 8] or magnetic[9], inertial and Global Position System (GPS) [10, 11], magnetic[12], or acoustic [13].

### Other Technologies

**Force Platforms** The methods described so far aim at characterizing human motion from a kinematic point of view. In other words, they provide measures for describing body movements (displacement, velocity, joint angles, etc.), without considering the causes. In some applications, however, it can be useful to consider also the kinetic aspect of motion, i.e., the forces that cause it. In gait or posture analyses, for example, the study of the interaction between Ground Reaction Forces (GRFs) and human body can help clinicians in quantifying more accurately balance and walking abilities of a patient. In order to measure precisely GRFs, force platforms (or force plates) are commonly used. These sensors are usually based on different technologies (strain gauges, piezoelectric sensors, capacitance gauges, piezoresistive, etc.) and can provide mono or multi dimensional representation of the measured forces [14]. Force platforms are often used in combination with optical mo-cap system in gait analysis laboratories.

**Electromyography** Electromyography (EMG) is a technique for recording and assessing the electrical activity produced by skeletal muscles through electrodes, placed on the skin surface. It provides an indirect indication of the muscle functions that can not be measured directly since it occurs below the skin and the subcutaneous tissues. EMG is commonly used as diagnostics tool for identifying neuromuscular diseases (e.g., dystrophies and neuropathies) or disorders of motor control. In the context of human motion analysis, (multichannel) EMG allows to detect muscles activation and provide timing information which can aid physicians in analyzing the subject motor

condition. Also in this case, the combined use of EMG and optical [15] or inertial [16] mo-cap technologies has been proposed for different clinical applications.

## 1.2 Inertial Sensing

As anticipated in Section 1.1.1, inertial sensing is becoming increasingly popular in human motion analysis and in a variety of different applications. The advance in Micro Electro Mechanical Systems (MEMS) has enabled miniaturization, cost reduction, and performance enhancement of inertial sensors and their spread in many fields beside the biomedical one, such as military, entrainment, robotics, sports, and control systems, as shown in Figure 1.6.

Usually, the term inertial sensors refers to sensing devices which use the principle of inertia (i.e., the tendency of a body to maintain its translational or rotation motion unless its state is disturbed by an external force or torque, respectively) to measure physical quantities. In the following, the main characteristics of inertial sensors, namely accelerometers and gyroscopes, are presented. Moreover, a brief description of sensors (e.g., magnetometers) and techniques (e.g., sensor fusion and orientation filters), used for improving the motion tracking performance of purely inertial systems, is provided.

### 1.2.1 Accelerometers

An accelerometer is an inertial sensor which can measure accelerations. In its simplest representation, a single-axis accelerometer can be considered as a spring-mass system, as shown in Figure 1.7.

A proof mass ($m$) is suspended in a rigid structure and is connected to a spring. When a force is applied to the object, it is possible to compute the acceleration exploiting two physical principles: the Newton's second law and the Hooke's law. The former express the relationship between a force $F$ (dimension: [N]), a mass $m$ (dimension: [kg]), and an acceleration $a$ (dimension: [m/s$^2$]), according to the following equation:

$$F = ma. \tag{1.1}$$

(a)

(b)

(c)

(d)

(e)


(f)

Figure 1.6: Examples of applications for inertial sensors: (a) Unmanned Aerial Vehicles (UAVs) use inertial sensor for automatic tracking and navigation; (b), (c), (d) inertial sensing for entrainment: console gaming, virtual reality, and smartphones; (e) fitness trackers for performance monitoring in sports; (f) a humanoid robot (ASIMO by Honda) which uses inertial sensors for controlling balance and mobility.

The latter states that a spring, when compressed or stretched, will generate a force $F$ (dimension: [N]) which is proportional to the displacement $x$ (dimension: [m]) from its rest position. The Hooke's law can be formally expressed as follows:

$$F = kx. \tag{1.2}$$

where $k$ (dimension: [N/m]) is a positive real constant, which depends from the physical characteristics of the spring. If the system undergoes an acceleration, a proportional force will be produced according to the second Newton's law. This force will cause a displacement of the mass and, consequently, a compression or expansion of

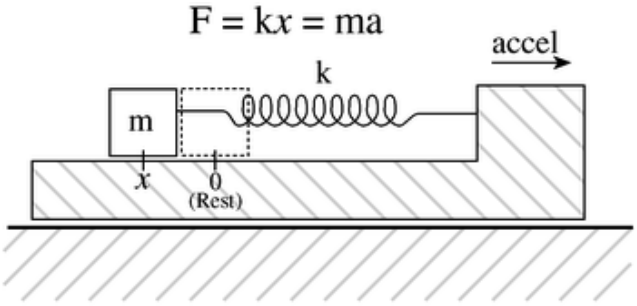


Figure 1.7: Mass-Spring system used for measuring acceleration (image credit: `http://www.ccrma.stanford.edu`).

the spring, under the following constrain:

$$F = ma = kx \tag{1.3}$$

which can be also expressed as:

$$a = \frac{kx}{m}. \tag{1.4}$$

The relation given in 1.4 allows us to quantify the system acceleration measuring the displacement of a mass connected to a spring. In order to obtain a multiple axes measurement of the acceleration, this mechanism needs to be replicated along each of the required axes.

The majority of commercially available accelerometers rely on the following methods for converting the mechanical motion in an electric signal:

- *Piezoelectric, piezoresistive, and capacitive*. A specific material/electrical component is used for measuring the displacement of the proof mass and generate a proportional electrical output. In particular, piezoelectric accelerometers use piezoelectric materials (e.g., quartz) to generate a tiny electric signal in response to a mechanical stress; piezoresistive accelerometers use piezoresistors, i.e., electrical components which change their resistivity properties when undergoes a mechanical strain; capacitive accelerometers measure changes in the capacitance of a capacitor, caused by variations in the distance between two metal plates, which move proportionally to the applied acceleration.

- *Hall-effect*. This kind of accelerometers exploit the Hall effect (i.e, the production of a potential difference across a conductor, namely the Hall element, carrying an electric current when a magnetic field is applied in a direction perpendicular to that of the current flow). The Hall element is attached to a spring with a seismic mass deflecting because of the forces due to acceleration. The element moves in a nonuniform, linear-gradient-intensity magnetic field. Under these conditions, the generated transverse Hall voltage is proportional to the measured acceleration.

- *MEMS*. This technology allows the production of low-cost, miniaturized, robust, low-power, flexible, and accurate accelerometers and it is currently the most used manufacturing method. MEMS-based accelerometers exploit different technologies. One of the most widespread operational principles consists in a miniaturized versions of a capacitive accelerometer: this approach relies typically on a structure that uses two capacitors formed by a movable plate held between two fixed plates. Under zero net force, the two capacitors are equal but a change in force will cause the movable plate to shift closer to one of the fixed plates, increasing the capacitance, and further away from the other fixed reducing that capacitance. This difference in capacitance is detected and amplified to produce a voltage proportional to the acceleration. A schematic representation of a capacitive MEMS accelerometer is shown in Figure 1.8 (a). The dimensions of the structure are in the order of microns (Figure 1.8 (b)). A detailed description of MEMS-based accelerometers is given in [17].

### 1.2.2 Gyroscopes

Gyroscopes are inertial sensors able to measure angular motion. In its classical concept, invented by Foucault in 1852, a (mechanical) gyroscope is formed by a spinning wheel or disc suspended in light supporting rings called gimbals. The gimbals have nearly-frictionless bearings which isolate the central disc from outside torque and allow the rotors to have additional degrees of rotational freedom. When the wheel

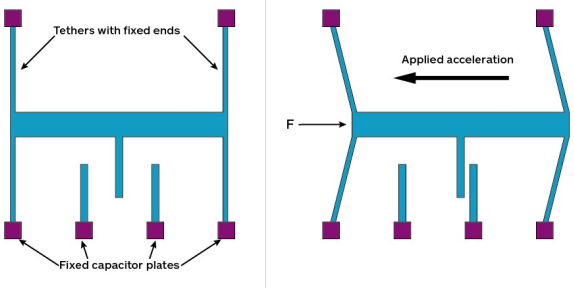


(a)

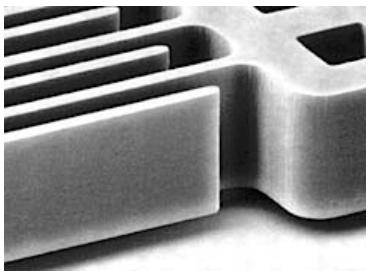

(b)

Figure 1.8: A capacitive MEMS accelerometer: (a) a schematic representation of its operating principle (image credit: `http://www.globalspec.com`); (b) a detail of a 20 microns thick single-crystal comb structure (image credit: `http://www.sensorsmag.com`).

is spun on its axis at high speeds, it tends to maintain a constant orientation, according to Newton's second law, which states that the angular momentum of a body will remain unchanged unless it is acted upon by a torque. When an external torque is applied, the gimbals will try to reorient to keep the spin axis of the rotor in the same direction. Quantifying the entity of the precession phenomenon, it is possible to measure the angular velocity of the rotation induced by the applied torque. The fundamental equation describing the behavior of the gyroscope is the following:

$$\boldsymbol{\tau} = \frac{d\boldsymbol{L}}{dt} = \frac{d(I\boldsymbol{\omega})}{dt} = I\boldsymbol{\alpha} \tag{1.5}$$

where: $\boldsymbol{\tau}$ (dimension: [N·m]) is a vector representing the torque of the gyro-

scope; $\boldsymbol{L}$ (dimension: [N·m·s]) is its angular momentum; $I$ (dimension: [kg·m$^2$]) is a scalar and represents its moment of inertia; $\boldsymbol{\omega}$ (dimension: [rad/s]) and $\boldsymbol{\alpha}$ (dimension: [rad/s$^2$]) are the angular velocity and acceleration of the gyroscope, respectively. Mechanical gyroscopes, however, are expensive, fragile, cumbersome, and, consequently, not suitable for many practical applications. Different alternative approaches, based mostly on optical methods or on the properties of vibrating structures, are currently available. In particular, as for the accelerometers, MEMS-based gyroscopes are becoming increasingly popular because they are small, inexpensive, energy-efficient, and robust. These sensors use a vibrating structure to determine the angular velocity, exploiting the physical principle for which a vibrating element tends to continue vibrating also of its support structure is rotating. The Coriolis effect generates a force (i.e., Coriolis apparent force, $\boldsymbol{F}_C$), on the support structure. By sensing this force, it is possible to compute the rotation rate $\boldsymbol{\omega}$ (dimension: [rad/s]) according to the following expression:

$$\boldsymbol{F}_C = -2m(\boldsymbol{\omega} \times \boldsymbol{v}) \tag{1.6}$$

where $m$ (dimension: [kg]) is the mass of the vibrating element and $\boldsymbol{v}$ (dimension: [m/s]) is its velocity. Further details on the characteristics of MEMS-based gyroscopes are provided in [17].

Other types of gyroscopes, based on different operational principles, which are usually very reliable and accurate but also expensive, are:

- Gyrostat;
- Ring Laser Gyroscope (RLG);
- Fiber Optic Gyroscope (FOG);
- Dynamically Tuned Gyroscope (DTG);
- gyroscope based on the Magneto-Hydro-Dynamics (MHD) effect;
- electro-chemical gyroscope (based on Molecular Electronic Transducer, MET, technology);

- London moment gyroscope.

### 1.2.3 Magnetometers

Magnetometers are sensors that measure either the (scalar) intensity or the vector components (magnitude and direction) of a magnetic field. Although they are not inertial sensors, since they do not rely on the inertia principle, they are often used in combination with accelerometers and gyroscopes, forming multi-sensor platforms, such as IMUs and Magnetic, Angular Rate, and Gravity (MARG) sensors. Also in this case, there exists a wide variety of magnetometers categories, which differ depending on performance, capabilities, costs, and operational principles. Among the others, some of the technologies used in modern magnetometers are:

- SQUID (Superconducting Quantum Interference Device) [Scalar/Vector];
- Optical Magnetometry [Scalar];
- Proton precession magnetometer[Scalar];
- Magnetoresistive devices [Vector];
- Fluxgate [Vector];
- Spin-exchange relaxation-free (SERF) atomic [Vector];
- Hall effect [Vector].

MEMS technology is, once again, the most adopted for the production of magnetometers used in practical applications. MEMS-based magnetic sensors relies on the mechanical motion of the MEMS structure due to the Lorentz force acting on the current-carrying conductor in the magnetic field. The mechanical motion of the micro-structure can be sensed either electronically or optically. An extensive review on the most common technologies used for magnetic field sensing are described and compared in [18].

### 1.2.4 Sensor Fusion

As highlighted in the previous section, MEMS-based sensors are currently the most used in the majority of industrial, medical, and consumer applications because of their cost and energy effectiveness, miniaturized size, and robustness. Nevertheless, beside these positive characteristics, MEMS IMUs have also some limitations: depending on the manufacturing process and the target application area, their costs, performance, and reliability can vary consistently, even by several orders of magnitude. Usually, the main error sources and factors which limit MEMS sensors' performance are:

- *drift*: the change in absolute error over time. It can have a very high impact, if not adequately corrected, on long term measurements since signals acquired by IMUs are often integrated over time to compute angles (from angular velocities) or double integrated to compute positions (from accelerations), introducing a constant error which grows linearly or quadratically with time;
- *constant bias*: average error measured when the sensor is at rest;
- *bias stability*: thermal and/or flicker noise have a time-variable influence on the sensor output. A bias stability measurement describes how the bias of a device may change over a specified period of time;
- *Calibration errors*: errors in scale factors, alignments and output linearities;
- *Magnetic interference and disturbance*: errors in the measure of a magnetic field introduced by external sources including electrical appliances, metal furniture and metal structures within a buildings construction.

In order to overcome the intrinsic limitations of each sensing device and the lack of accuracy and stability, a good strategy consists in combining the measurement by multiple sensors using a sensor fusion approach.

An application in which the use of sensor fusion allows to achieve better performance compared to those obtained using single sensors is the estimation of the three-dimensional orientation of a sensing node. Integration of the raw gyroscope signal, for example, leads to the accumulation of a consistent amount of error after a

limited time and can only provide relative angles. Accelerometers and magnetometers can be used for identifying absolute references for the orientation, such as the direction of the gravity or the Earth's magnetic field, but they are both susceptible to noise. Combining the data acquired by gyroscope, accelerometer, and magnetometer (they have to be triaxial), it is possible to provide a complete measurement of orientation relative to the direction of gravity and the Earth's magnetic field. Systems able to provide this information are usually called Attitude and Heading Reference System (AHRS) and can be used in many different contexts, such as in a navigation system for computing yaw, pitch, and roll angles of an aircraft or in a clinic for computing the 3-dimensional orientation of a body segment.

The state of the art techniques used for implementing orientation filters, i.e., algorithms able to estimate and track the orientation through the optimal fusion of gyroscope, accelerometer and magnetometer measurements, are based on Kalman filters. A Kalman Filter (KF) is a statistical, recursive estimation technique that uses a series of noisy measurements observed over time and produces estimates of the process state through an iterative prediction/correction approach, by using Bayesian inference and estimating a joint probability distribution over the variables for each time frame [19]. It is an optimal estimator if the noise components are Gaussian and the transition matrices are linear. For non-linear systems and non-Gaussian noise, there are variations of the standard KF, such as Extended Kalman Filter (EKF) and the Unscented Kalman Filter (UKF), which allow to achieve good but sub-optimal performance. The KF and its variants have been successfully used as bases in many orientations filters [20, 21, 22, 23] and solutions based on KFs have been also integrated in many commercial products thanks to their accuracy and effectiveness. The main drawbacks of this approach are its complex implementation and the high computational power needed for the linearizion procedure, required in almost all the real-world applications. Different alternative methods have been proposed in the literature based, for instance, on particle [24] or complementary [25] filters or , fuzzy processing [26]. In this thesis, the orientation filter developed by Madgwick [27] has been used. It is a computational efficient and easily tunable algorithm which employs a quaternion representation of the orientation and is not subject to the problematic

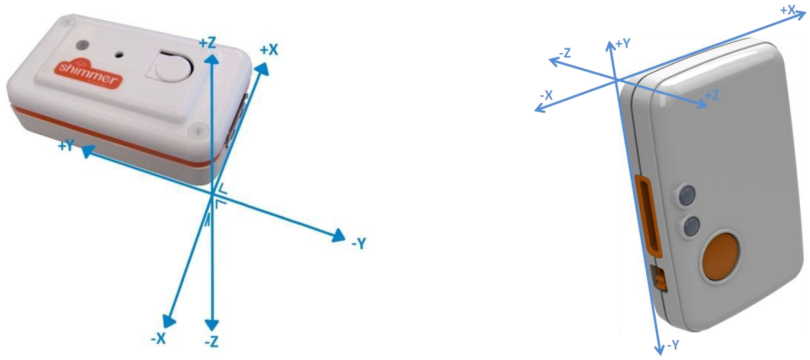


(a) (b)

Figure 1.9: Shimmer nodes and their reference systems: (a) Shimmer2r IMU and (b) Shimmer3 IMU.

singularities associated with an Euler angle representation (i.e., gimbal lock). The use of an optimized gradient descent procedure, an on-line magnetic distortion compensation algorithm, and a gyroscope drift bias compensation technique, allows this orientation filter to achieve performance comparable to the most accurate Kalman-based solutions with considerably less computational power and complexity.

### 1.2.5 The Shimmer Platform

In this work, an inertial-based BSN, in various configurations, has been adopted as mo-cap tool. To maintain homogeneity across the different applications, two versions of the same sensor platform provided by Shimmer (Sensing Health with Intelligence, Modularity, Mobility, and Experimental Reusability) (`http://www.shimmersensing.com/`, [28]) have been used. A brief description of both versions of Shimmer IMUs is given in the following.

#### The Shimmer2r IMU

The first generation of Shimmer devices used in this work, with its coordinate reference system, is shown in Figure 1.9 (a). It is a small and low-power wireless IMU, equipped with: a TI MSP430 CPU (up to 8 MHz), with 10 KB RAM and 48 KB

Flash memory; Bluetooth (Roving Networks RN-42) and IEEE 802.15.4-compliant (TI CC2420) radios; an integrated (up to 2 GB) microSD card slot; 3 colored status LEDs; a 450 mAh rechargeable Li-ion battery; and a triaxial accelerometer (Freescale MMA7361). Moreover, the device is designed so that different external sensing modules can be easily connected. The 9DoF Kinematic Sensor expansion module, which is supplied with a triaxial gyroscope (InvenSense 500 series) and a triaxial magnetometer (Honeywell HMC5843), has been used. The device support different sampling rates (up to 1024 Hz) and can be easily attached to body segments through Velcro straps.

#### The Shimmer3 IMU

In the updated version of Shimmer IMUs, called Shimmer3, size has been reduced and the set of integrated sensors has been enlarged, increasing its overall performance and usability. In the new configuration, the device is equipped with: a 24 MHz MSP430 CPU, with 16 KB RAM and 256 KB of Flash memory; a low-noise triaxial analog accelerometer (Kionix KXRB5-2042); integrated digital wide range accelerometer and magnetometer (STMicroelectronics LSM303DLHC); an integrated digital gyroscope (Invensense MPU-9150); a relative pressure sensor (Altimeter); and a Temperature sensor. The battery capacity and the Bluetooth radio have been kept unchanged compared to the previous version whereas the SD slot has been updated to support up to 32 GB of data storage. The maximum supported sampling rate is 1024 Hz.

## 1.3 Clinical Applications

Motion analysis is widely used in clinical environments for many different applications, such as the quantification of both normal and pathological movements, the assessment of impairments level in patients affected by various neuro-motor diseases, the planning and the monitoring of rehabilitation strategies, the evaluation of interventions effectiveness, and so on.

Classical measurement systems are limited because they cannot measure the dynamic component of the movements without limiting them. Gaining information about the characteristics of motion with laboratory solutions, such as optoelectronic or electromagnetic mo-cap systems, is not always feasible due to the high costs and complexity of these acquisition tools. Moreover, they have several additional limitations: (i) patients need to be in ad-hoc laboratories in the clinic; (ii) the operating field and acquisition area are limited; (iii) environmental interferences and occlusion phenomena can occur and this results in very long post-processing and data cleaning operations; (iv) specifically trained personnel is needed to run the acquisitions.

As anticipated in Section 1.2, the advances in MEMS technologies have allowed the use of inertial-based sensors also in the field of motion analysis. These small-sized, low-powered, easy-to-use, and affordable sensors can provide accurate, dynamic 3-dimensional measures of body movements, without the constrain of the classical technologies. Different studies have proven the validity of inertial sensing for mo-cap in clinical environments through comparison with gold standard technologies [29, 30, 31]. In the following, the main categories of clinical applications in which inertial-based mo-cap has been successfully applied are briefly described, in increasing order of abstraction.

### 1.3.1 Quantification of Body Movements

Mo-cap techniques are often used for measuring and characterizing movements of specific body segments or parts, such as upper [32, 33, 34] and lower [35, 36] limbs, trunk [37, 38], head [39], etc. The objective quantification of these body movements can help clinicians in a variety of contexts, such as the assessment of the efficacy of rehabilitations strategies or of the level of severity of a particular medical condition, the diagnosis of movement disorders, the progression of post-intervention recovery, and so on.

### 1.3.2 Characterization of Specific Motor Tasks/Symptoms

The mere measurements of the position/orientation of body segment/joint is often not sufficient for providing meaningful information to clinicians. In these cases, a higher level analysis is required for characterizing in a proper way specific movements, activities, or motor symptoms. In the assessment process of motor impairing disease, for instance, functional motor task are defined by clinical scales in order to help the medical personnel to achieve a more objective evaluation. Processed and aggregated information about the performance of a patient in a particular task, extracted by the raw kinematic measures, can be more interpretable by clinicians than a confused collection of numbers and parameters. Usually, the processing pipeline starts from a set of low-level features extracted from the signals acquired by the wearable sensors; then, the features are processed or aggregated, often through machine learning techniques, in order to provide high-level and more intelligible data. Some examples of applications which aim at characterizing specific movements or motor symptoms are: the evaluation of well-defined functional tasks, such as those of the UPDRS [40, 41, 42] or other clinical scales [43, 44]; the monitoring of specific motor symptoms, such as tremor [45], dyskinesia [46], bradykinesia [47], and freezing of gait [48]; the analysis of gait. Since the latter is the motor task on which we focused the most in this thesis, a specific section is dedicated in the following to its detailed description.

#### Gait Analysis

Gait Analysis (GA) is the systematic study of human locomotion. It finds application in many different fields, such as in sports, rehabilitation, and health diagnostics [49]. In particular, clinical GA is the process by which quantitative information is collected in order to detect and understand gait abnormalities and guide clinicians' treatment decisions. It can be used, for instance, to assess spastic gait in patients with partial paralysis, cerebral palsy, Parkinson's disease, or neuromuscular disorders or for monitoring the patient's healing progress in post-stroke or post-surgery rehabilitation. As anticipated in Section 1.1, the study of animal gait began more than 2000 years

ago with Aristotle and continued across the centuries until today, thanks to the contributions of great scientific personalities, such as Giovanni Alfonso Borelli, in 17th century, Christian Wilhelm Braune, Otto Fischer, Eadweard Muybridge, and Étienne-Jules Marey, in between 19th and 20th centuries. Initially, only limited amounts of data could be collected and processed, because of limitations in tools and models used to interpret the results. In the latter part of the 20th century, however, gait analysis technology began to improve significantly, increasing the potential for clinical application of gait analysis. Modern computer-based clinical gait analysis has developed increasingly since the late 70s, when the availability of commercial video-camera systems allowed the conduction of detailed and individual studies within acceptable time and cost constraints. Optical technologies, in fact, were the first to be used in gait laboratories and they are, still today, the golden standard approach, due to their accuracy and reliability [50]. Nevertheless, optical GA has the limitations described in Section 1.1.1 for vision-based mo-cap systems, namely, the need of specific laboratories and highly-specialized personnel, high-costs, lengthy set up and post-processing times, and a limited acquisition volume, which make the system unusable outside the clinics. Other technologies used for GA are based on foot switches [51], electromyography (EMG) [52], and force platforms [53]. These methods are often used in combination with optical systems and, although they are accurate and provide highly detailed information on the quality of gait, they have several drawbacks and can not be used for a long-term and continuous assessment of patients. IMU-based GA is currently the most adopted alternative approach, because it is cost-effective, reliable, and easy-to-use. Different works, focusing on this sensing technology for GA, have appeared in the both medical and engineering literature in recent years.They differ in many aspects related , for example, to the kind, the number, and the positioning of the sensors used for collecting the data, the methods used for their processing, the level of detail of the analysis, and so on. In general, we can distinguish the following main categories of approaches: accelerometer-based and gyroscope-based. One of the first works which took advantage of the accelerometric approach was conducted in [54]. Two accelerometers mounted on the patient's thighs were used for gait temporal features estimation. In [55], an analysis of spatio-temporal gait param-

eters during overground walking based upon a method that needs only the measure of lower trunk acceleration is presented. A single IMU placed on the patient's pelvis has been used in [56] to perform an accurate determination of foot contact instances and to estimate bilateral step length. A wavelet-based approach was developed to identify intervals of interest where gait event candidates were searched in the accelerometer signals. Then, a combination of a Kalman filter and an optimally filtered direct and reverse integration applied to the IMU signals was used to calculate the pelvis displacement along the direction of motion and to measure the step length and the traversed distance.

The approach based on gyroscopes is the mostly used. In 1997, Miyazaki described a system for a long-term monitoring of step length and walking velocity in patient with gait disabilities, using a gyroscope attached on the thigh [57]. Tong et al. investigated the possibility of using uni-axial gyroscopes to develop a simple portable GA system, using four gyroscopes (two mounted on the shanks and two on the thighs) [58]. In [59], Aminian et al. used a similar configuration of nodes to evaluate gait characteristics. The temporal features were extracted using the angular rate signal of the shanks while the spatial parameters were estimated using a double pendulum model that involves both the shanks and the thighs segments. Bart et al. [60] used a shoe-mounted gyroscope and a Dynamic Time Warping algorithm for detecting accurately gait events in both healthy and parkinsonian subjects. In some cases, both accelerometers and gyroscopes have been used for segmenting gait phases and extract spatio-temporal parameters: in the system described in [61], Sabatini et al. used a foot mounted IMU to estimate gait events, step length and walking speed; in [62], a comparison between accelerometers and gyroscope-based gait segmentation algorithms is performed, showing that both approaches have similar performance compared to gold standard methods based on foot switches. Another possible attempt to classify gait analysis approaches through inertial sensing may be based on the number of sensors used in the BSN. Undoubtedly, a single-sensor approach is simpler, more suitable for long-term monitoring in free living conditions, more comfortable for the patient, and less obtrusive, although it has to sacrifice part of the accuracy and the detail level of the analysis. On the other hand, a multi sensor

approach can be more accurate, providing a more complete set of parameters, but implicates higher complexity, costs, and movement limitations. A recent and accurate review of common approaches used for IMU-based gait analysis is provided in [63].

Independently from the used methods and sensors, the analysis of gait patterns aims at providing clinicians quantitative measures that characterize a subject's walking performance under different points of view: most of the GA algorithms provide temporal and spatial parameters associated to gait cycles [59, 64, 55]; others allows to quantify the symmetry and the regularity of steps/strides [65]; some methods highlight the kinematic features of gait patterns, such as range of rotation of lower limbs segments [66], or the kinetic aspect, showing the forces involved in gait movements [67].

In general, spatio-temporal parameters are the most meaningful under a clinical point of view. The first step needed for computing them consists in segmenting gait, which is a complex movement that involves many muscles and joints, into simpler blocks, denoted as *gait cycles*. Two fundamental events per leg are needed to identify a complete gait cycle and all the other temporal parameters which define the different gait phases: the Heel Strike ($HS$) (i.e., the instant at which the foot touches the ground) and the Toe-Off ($TO$) (i.e., the instant at which the foot leaves the ground). In particular, a gait cycle starts with the $HS$ of a foot and ends with the following $HS$ of the same foot. The complete sequence of events, considering for example a gait cycle starting with the right leg (Figure 1.10), is the following: right $HS$ ($HS_R$), left $TO$ ($TO_L$), left $HS$ ($HS_L$), right $TO$ ($TO_R$), right $HS$ ($HS_R$).

Once all the $HS$s and $TO$s have been identified for both legs, the following temporal parameters can be calculated for the $k$-th gait cycle.

- Gait Cycle Time ($GCT$) (dimension: [s]): the time interval between the $HS$ of a foot to the next $HS$ of the same foot. In particular:

$$GCT_{R/L}(k) = HS_{R/L}(k+1) - HS_{R/L}(k).$$

- Stance Time ($ST$) (adimensional, % of GCT): the time percentage (relative to the corresponding gait cycle) during which a foot is in contact with the ground.

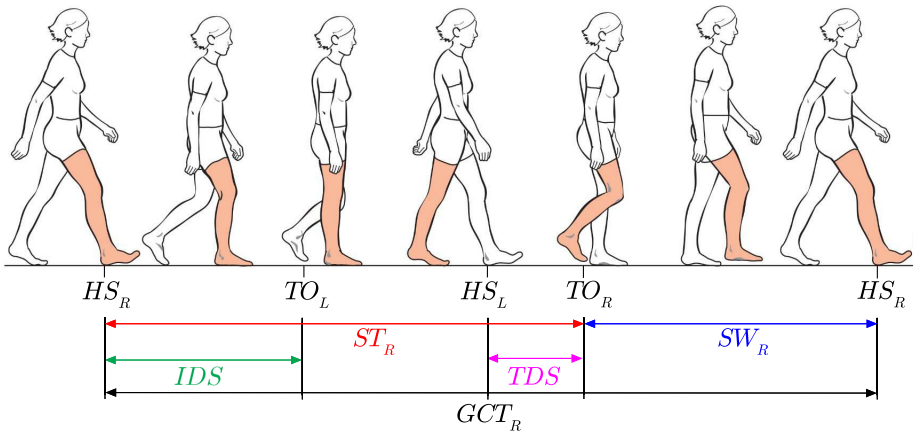


Figure 1.10: Segmentation of a (right) gait cycle (image credit: `http://www.studyblue.com`).

In particular:

$$ST_{R/L}(k) = 100 \times \frac{TO_{R/L}(k) - HS_{R/L}(k)}{GCT_{R/L}(k)}.$$

- Swing Time ($SW$) (adimensional, % of GCT): the time percentage (relative to the considered gait cycle) during which a foot is not in contact with the ground. In particular:

$$SW_{R/L}(k) = 100 - ST_{R/L}(k).$$

- Double Support ($DS$) (adimensional, % of GCT): the time percentage (relative to the considered gait cycle) during which both feet are in contact with the ground. This happens twice during a gait cycle: at the beginning and at the end of one foot's stance phase. The first DS phase is denoted as Initial Double Support ($IDS$) and the second one is denoted as Terminal Double Support ($TDS$). They can be expressed as follows:

$$IDS(k) = 100 \times \frac{TO_L(k) - HS_R(k)}{GCT(k)}$$

$$TDS(k) = 100 \times \frac{TO_R(k) - HS_L(k)}{GCT(k)}.$$

Finally, the DS can be given the following expression:

$$DS(k) = IDS(k) + TDS(k).$$

A quantity related to DS, denoted as Limp, is defined as follows:

$$Limp(k) = |IDS(k) - TDS(k)|.$$

For what concerns the spatial parameters, the most commonly considered for gait characterization are the following.

- Stride Length ($SL_{R/L}$) (adimensional: % of subject's height): the distance traveled from the $HS$ of one foot to the following $HS$ of the same foot (i.e., a stride).
- Stride Velocity ($SV_{R/L}$) (dimension: [% of subject's height/s]): the average linear velocity of a foot during a stride.
- Step Length ($StepL_{R/L}$) (adimensional: % of subject's height): the distance traveled from the $HS$ of one foot to the $HS$ of the other foot (i.e., a step).
- Step Velocity ($StepV_{R/L}$) (dimension: [% of subject's height/s]): the average linear velocity of a foot during a step.

A visual representation of stride/step lengths is shown in Figure 1.11

### 1.3.3 Activity Detection and Classification

The highest abstraction level of human motion analysis consists in determining if the user is performing an action (*detection*) and, if yes, what kind of action (*classification*). The availability of a system capable of automatically classifying the physical activity performed by a human subject is extremely attractive for many applications in the field of health-care monitoring and for developing advanced human-machine interfaces. Defining the sequence of a patient's actions across the entire day, in fact, can provide extremely meaningful information in various contexts, such as

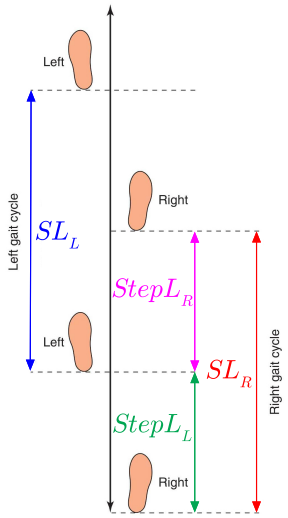


Figure 1.11: Visual representation of stride/step lengths (image credit: `http://www.studyblue.com`).

the monitoring of symptoms severity fluctuations on the long-term for Parkinson's Disease patients [68, 16], the effectiveness of a rehabilitation strategy in the post-intervention period [69, 70], to monitor the physical condition and to encourage an healthy lifestyle in obese subjects [71], or a safety system to prevent and detect falls for elderly people [72, 73, 74]. Most of the cited approaches use the signals acquired by single or multiple accelerometers attached to different body segments (usually, trunk, wrists, or ankles) in combination with machine learning techniques (simple supervised learning methods, relying on various classifiers, such as SVM, *k*NN, Random Forest, etc., or dynamic methods, such as Hidden Markov Models (HMMs) or deep neural networks), in order train an automatic system able to identify and distinguish between a set of predefined activities. A detailed review of the available literature on the use of inertial sensors for the detection and classification of physical activities is provided by Yang et al. in [75].

## 1.4 Thesis Outline

In this thesis, we focuses on the characterization of specific motor tasks in PD and post-stroke patients, relying on inertial-based BSNs, advanced signal processing techniques, and machine learning. In particular, the manuscript is structured as follows:

- **Chapter 2:** ***Automatic Assessment of Gait in Parkinson's Disease using a Low-complexity IMU-based BSN.*** In this chapter, a system, based on a BSN formed by three IMUs, for the quantitative characterization of the *gait* task in Parkinsonians is presented. A novel gait segmentation algorithm is also proposed as a starting point for the computation of temporal parameters. Additional features in both time and frequency domains are extracted and analyzed, trying to highlight the connection between them and the clinical evaluation by the medical personnel. Exploiting machine learning techniques, a classification system able to provide an automatic assessment of patients' motor performance mimicking the evaluation criteria by the clinicians is also implemented and exhaustively tested. The performances achieved in the kinematic characterization of gait and its automatic evaluation are finally discussed and commented.

- **Chapter 3:** ***Kinematic Characterization and Comparative Outlook of UPDRS scoring in Multiple Motor Tasks for PD.*** The approach described in the previous chapter for the *gait* task has been extended to two additional functional motor tasks defined in the UPDRS clinical evaluation scale: the *leg agility* and the *sit-to-stand*. Using a unique BSN, kinematic features are specifically extracted for each task and used, together with the assessments provided by three expert neurologists, for training an automatic evaluation system. The achieved classification performance is investigated and the correlations between tasks, in terms of UPDRS scoring, are analyzed. Finally, the suitability of the proposed system for real applications in e-health scenarios is discussed.

- **Chapter 4:** ***Quantitative Evaluation of Gait in Post-stroke patients.*** Two solutions for objective and accurate characterization of gait in post-stroke patients are described in this chapter. The first approach relies on a multi-sensor

BSN but, due to its complexity, is only briefly detailed. The second system is based on a single IMU mounted on the patient's back and is deeply investigated. A novel algorithm for robust gait segmentation is proposed, relying on per-subject automatic calibration procedures, which allow the system to deal with the asymmetry and irregularity of the hemiparetic gait. A complete set of spatio-temporal parameters is extracted and validated against an optoelectronic system. Finally, the possible future extensions of the current approach are discussed.

# Chapter 2

# Automatic Assessment of Gait in Parkinson's Disease using a Low-complexity IMU-based BSN

*Walking gets the feet moving, the blood moving, the mind moving.*
*And movement is life.*

– Carrie Latet

Walking is a fundamental activity of our everyday life. Although it may appear as a natural and an easy task, in reality, it is a complex action which involves musculoskeletal, neurologic, and cardiovascular systems. For this reason, the clinical study of human gait, as anticipated in Chapter 1, can provide valuable information to medical personnel across the whole clinical assessment process, from the diagnosis to the post-intervention rehabilitation, of several motor-impairing diseases. In Parkinson's Disease, the analysis of gait patterns is extremely useful for quantifying the motor symptoms severity and the response to medications of a patient. In this chapter, the a novel implemented system for the objective and automatic evaluations of gait in Parkinsonians, is described, validated, and experimentally investigated.

## 2.1 Introduction

### 2.1.1 Parkinson's Disease

Parkinson's Disease (PD) is a chronic and progressive neuro-degenerative condition in which the death of dopamine-secreting cells, located mostly in a region of the brain called *substantia nigra*, is responsible for a gradual impairment of the motor system. In industrialized countries, PD affects about 0.3% of the whole population and its prevalence increases up to 4% in people over age 80 [76]. Although the disorder was firstly described by the English doctor James Parkinson in his monograph *Essay on the Shaking Palsy* in 1817, the exact causes of the disease's onset are still unclear and have been often associated with a combination of environmental [77] and genetic [78] factors. The most evident manifestation of the disease, since the early stage, is the appearance of primary motor symptoms such as tremors, bradykinesia (i.e., slowness of movement), rigidity, postural instability, and gait impairments, but patients can also experiment non-motor symptoms, such as depression, sleep disturbance, anxiety, dementia, and many other. A careful physical examination and an accurate medical history of each patient is required in order to detect the core motor symptoms and to diagnose the presence of the disease. Moreover, when the disorder has been diagnosed, the typical management of the symptoms is based on the use of dopaminergic drugs, such as Levodopa or dopamine agonist. A patient-centric therapy is required in order to maximize the efficacy of the medications and minimize the impact of the side effects, such as dyskinesia and motor fluctuations, which can even worsen the deficiencies induced by the disease itself. When drug therapies are not sufficient or the related complications are too severe, Deep Brain Stimulation (DBS), i.e., a neurosurgical procedure in which implanted electrodes stimulate specific brain regions, can be considered as an option for managing motor symptoms. In most cases, during the clinical assessment process, physicians can only rely on their experience, on qualitative and sporadic clinical observations, which may be not representative of the actual disease status. For these reasons, an accurate, quantitative and continuous monitoring of the symptoms should be required in order to define an effective and patient-focused therapy.

### 2.1.2 Unified Parkinson's Disease Rating Scale

To improve the quality of symptoms' assessment, different standardized, semi-quantitative evaluation scales have been introduced to help clinicians to achieve a more objective analysis of the disease progression. Above all, the Movement Disorder Society - Unified Parkinson's Disease Rating Scale (MDS-UPDRS) [79] is the most commonly used scale in the clinical study of the PD. The MDS-UPDRS[1] aims to follow the longitudinal course of the disease and define specific tasks in order to assess different aspects of the disorder. In particular, it focuses on the evaluation of the following elements:

1. Part I: non-motor experiences of daily living (13 items);
2. Part II: motor experiences of daily living (13 items);
3. Part III: motor examination (18 items);
4. Part IV: motor complications (6 items).

Each task is evaluated providing an increasing discrete score between 0, which means no impairment, and 4, which means severe difficulties in performing the item. Several studies have pointed out a good test-retest reliability for the global UPDRS score but this scale still present some limits in clinical trials. Some of these limitations are: the need for specifically trained neurologist to assign the UPDRS score; the inter-intra rater variability [80]; the discrete nature of the UPDRS scores, which is not optimal to detect minimal changes during the disease progression [81]; and the difficulty to convey a concise score, especially when several movement components (such as speed, amplitude, hesitations, etc.) should be taken into account for the evaluation. In order to improve the UPDRS assessment reliability, monitoring the variations in symptoms severity and medication response in a more consistent way, the frequency and the duration of clinical trials should be increased [82]. Obviously, this solution

[1] For brevity, we refer at the MDS-UPDRS simply using the abbreviation UPDRS in the following. We remark, however, that it has to be distinguished by the original UPDRS, revised by the Movement Disorder Society in 2007.

is not always feasible or practical. Additional information on the disease condition outside the clinic are usually collected by asking patients to keep motor diaries while at home. However, this tool is often unreliable because of non-optimal compliance in the patient record keeping, recall bias or weak self-assessment skill due to cognitive impairment, that is often associated with late stages of PD [83]. It is clear that a tool which allows physicians to pursue a continuous, frequent, non-invasive, and objective monitoring of PD patients, in both clinical and domestic environments, would make it possible to overcome the majority of the limitations of current evaluation methods.

### 2.1.3 The VRehab Project

The use of motion analysis techniques, as described in Section 1.1, can provide clinicians those objective and quantitative measurements needed for an accurate characterization of patients' motor performance. At the same time, advent of new, miniaturized, low-cost, and unobtrusive motion-sensing devices, such as IMUs and the Microsoft Kinect, has extended the possibilities of performing an analysis of the movements on a longer temporal frame and outside the clinics. Based on these two ideas, the *Virtual Reality in the Assessment and TeleRehabilitation of Parkinsons Disease and Post-Stroke Disabilities*[2] (*VRehab*) project began in 2009. Different Italian academic (Università di Parma, Università di Torino, Politecnico di Milano, and Università del Piemonte Orientale), medical (Istituto Auxologico Italiano IRCCS, and Maggiore della Carità University Hospital of Novara), and industrial (Telecom Italia) realities took part in the project with the common aim to investigate the feasibility of a remote and affordable e-health system for the automatic evaluation of functional motor task and the monitoring of rehabilitation strategies in both PD and Post-Stroke populations. These goals are pursued by autonomous research groups working on smaller sub-projects, through different strategies, such as: the use of BSNs and external sensing devices for the monitoring of the motor performance; machine learning techniques for providing medical personnel high level information on patients' conditions; gamification of functional motor task, for both evaluation and rehabilitation

[2]Project supported by the Italian Ministry of Health (RF-2009-1472190).

purposes; virtual reality for creating immersive digital environments which can increase patients engagement. The work presented in this chapter, undertaken within the VRehab project and involving Università di Parma, Istituto Auxologico Italiano, Politecnico di Milano, and Telecom Italia, focuses specifically on the Gait (G) task of the UPDRS.

### 2.1.4 The UPDRS Gait Task

#### Task Description

In [79], the G task is defined by MDS as follows: the patient is asked to walk, at his/her preferred speed, away from the examiner for at least 10 m and in straight line, then to turn around and return to the starting point. This exercise should be performed in an obstacle-free environment and the initial/final acceleration phases should be discarded to avoid border effects in the analysis. The parameters of interest are those strictly related to the gait characteristics, such as: the stride/step amplitude and speed; the cadence; the gait cycle time; parameters related to the turning phase; the variability between left and right steps; and the arm swing. Freezing of gait should not be considered in the evaluation, if present, since it is addressed by a separate UPDRS item. The arm swing has not been considered in this work as well, as no sensor is placed on the upper limbs.

#### UPDRS Evaluation

Based on the observation of the gait characteristics suggested by the MDS, during a trial, physicians assign the patient an integer score between 0 and 4. In particular: a UPDRS score equal to 0 corresponds to normal walking; UPDRS score 1 is assigned to patients who can walk independently but present some minor impairments; UPDRS score 2 is given to subjects who can still walk unaided but with substantial deficits, such as slow walking, short steps, and festination; finally, UPDRS score equal to 3 and 4 are assigned to patients who cannot walk without the help of another person (or an assistance device) or who cannot walk at all, respectively. The evaluation of the G task is usually performed without the support of any technological

instrument so that the neurologist assesses the task in a qualitative way and relies especially on his/her experience and training. Therefore, assessments may vary from neurologist to neurologist (inter-rater variability) or from one evaluation session to another by the same neurologist (intra-rater variability) [80].

### 2.1.5 Chapter Contribution

In this chapter, a novel approach for the objective characterization of gait in PD patients is presented [1, 3]. Relevant kinematic features are extracted through an IMU-based BSN, formed by only three nodes (one on the chest and one per thigh). Then, the relationship between the extracted features and the UPDRS scores assigned by neurologists are investigated. Finally, a classification system for the automatic assessment of the UPDRS score in the G task is proposed and discussed.

## 2.2 Related Work

Gait is undoubtedly the motor task that mostly affects PD patients' lifestyle and independence, being representative of the global ability of patients to perform complex movements and also very sensitive to fluctuations between the periods in which the drug's effect is active and those in which it is not (ON-OFF state fluctuations). For these reasons, GA in Parkinsonians, as well as in many other gait-impairing pathologies, is extremely useful for providing clinicians a detailed picture of the general motor performance of a patient and, as denoted in Section1.3.2, it is a widely studied field. Several works have appeared in the literature focusing on the quantitative assessment of gait in PD patients. Most of them put their emphasis on the use of inertial-based wearable sensors for measuring the movement characteristics.

In [84], Salarian et al. proposed and validated against a reference system a clinical GA method based on the use of multiple gyroscopes attached to both lower (thighs and shanks) and upper (wrists) limbs. They extracted spatio-temporal parameters from controls and PD patients with DBS and compared the gait performance between the two groups. Additionally, they assessed the variations in gait features in the parkinsonian subgroup between the periods in which the brain stimulation was

ON and those in which was OFF, showing the efficacy of DBS in improving the walking abilities. Cancela et al.[85] used a single belt mounted accelerometer to analyze the differences between parkinsonian and healthy gait, showing that, through their signal processing approach, a single sensor was not enough for providing an accurate and subject-independent evaluation. Mariani et al [86] implemented a novel system based on wearable sensors on-shoe which provides outcome measures characterizing PD motor symptoms during Timed Up and Go (TUG) and gait tests. They introduced non-conventional spatio-temporal parameters and achieved an accuracy in the estimation of stride length and velocity of $1.3 \pm 3.0$ cm and $2.8 \pm 2.4$ cm/s, respectively. Also in [87], signals were collected through IMUs mounted on the shoes and processed to extract representative features in both control and PD patients. A pattern recognition algorithm was applied later on to select the most meaningful features and classify automatically the trials, distinguishing between healthy and pathological gait and quantifying the impairments severity according to the UPDRS and H&Y scales. In [88], a system based on gyroscopes mounted on the shanks was presented. Through a validation with a optoelectronic system and a force platform, the authors showed that their approach allows to achieve good performance in detecting gait cycles and computing temporal parameters, also in PD patients experimenting shuffling gait. The estimation of spatial features, although, was not sufficiently accurate. Moore et al.[89] focused on the long-term monitoring of parkinsonian gait characteristics, acquiring data continuously for 10 hours in a free living environment. A specific per-subject calibration procedure was used to compute stride length from accelometric data collected by IMUs placed on the shanks. The variations in stride length across the day were used to analyze and model the fluctuations of efficacy related to Levodopa therapy. Beside the cited works, several other research studies exist in the literature about GA for Parkinsonians. Some of the main limitations of the existing approaches are: (i) the use of complex BSNs with many sensing nodes, which can easily become intrusive and limit patients movements, especially in a free-living environment; (ii) the quantity and the quality of the measures provided for the characterization of gait, often not detailed and accurate enough for achieving a reliable assessment of the impairments level; (iii) the lack of high level “intelligence”,

which can automatically derive insights on patients' motor performance, trying to mimic the judging criteria by the medical personnel, offering them additional and aggregate information that can help the evaluation process; (iv) the lack of flexibility, for instance, in reusing the same BSN for the characterization and the assessment of other functional motor tasks. The approach proposed in this work aims at overcoming these limitations using: (i) a low-cost and low-complexity BSN, formed by 3 IMUs, suitable for the assessment of multiple UPDRS functional tasks; (ii) both newly developed and well-known techniques for the extraction of a complete set of gait parameters; (iii) machine learning methods to train a classification system able to automatically assess patients motor performance.

## 2.3 Experimental Set-up

In this section, the hardware configuration, the set of subjects, and the acquisition procedures used in the experimental tests are described.

### 2.3.1 Hardware

The BSN used for the data collection is formed by Shimmer 2r IMUs–the technical details of the sensing platform are provided in 1.2.5. The nodes stream data, from the integrated accelerometer, gyroscope, and magnetometer, wirelessly (via a Bluetooth radio interface) to a personal computer, where signal processing and data analysis are performed using the MATLAB framework (The MathWorks, Inc., USA, `http://www.mathworks.com/products/matlab.html`). The sampling rate, denoted as $f$, is set to 102.4 Hz because it is the closest, in the set of the sampling rates supported by the Shimmer platform, to the usual sampling frequency (namely, 100 Hz) of an optoelectronic reference system. For assessing the accuracy and the reliability of the inertial signals, indeed, a validation study has been performed in a preliminary stage of the project, acquiring simultaneously data from the IMUs and an optical mo-cap system by Vicon (Vicon, Oxford, U.K.). The latter is considered a gold standard in clinical motion analysis and it is able to provide the 3D coordinates,

within a calibrated moving volume, of passive markers positioned on specific anatomical landmarks of the subject, with an average accuracy of approximately 0.2 mm.

### 2.3.2 Subjects

The set of subjects involved in the study consists in 34 Parkinsonians (22 males and 12 females), with average age equal to 67.4 years (max = 79 years, min = 31 years) and standard deviation equal to 11.6 years. The average Modified Hoehn and Yahr (H&Y) Scale score for the patients was 1.6 (standard deviation equal to 0.47, minimum score equal to 1, maximum score equal to 3) on the 1-to-5 scale (higher scores indicate more severe impairments and more advanced stages of the disease). Furthermore, 4 healthy controls, with average age equal to 65.5 years and standard deviation equal to 2.88 years, labeled with an UPDRS score equal to 0 in all the trials, have also been included in the set of subjects as a benchmark and to increase the rating range. The number of healthy controls has been limited to 4 in order to avoid the polarization of the observed results towards the UPDRS 0 class because of the motor performance of non-Parkinsonian (i.e., healthy) subjects.

### 2.3.3 Acquisition Procedure

The BSN configuration designed for the data acquisition is shown in Figure 2.1 (a). It consists in three Shimmer 2r nodes, one per thigh, one on the chest, attached to the body with Velcro straps. As anticipated in Section 2.2, the reasons behind this choice, which may seem counterintuitive, considering that most of the work in the literature places the sensors on the feet, the shanks, or the ankles, are dictated by the fact that we aim at obtaining a minimal (in terms of number of sensors) but flexible configuration, suitable for the evaluation of multiple functional motor tasks defined in the UPDRS (in addition to the G task), such as leg agility, sit-to-stand, postural stability, etc. This would allow physicians to analyze, with the same BSN, different tasks without changing the configuration of the nodes, thus: minimizing the patients' stress; simplifying the acquisition procedure; and allowing sequential execution of the tasks. Moreover, the IMUs' placement facilitates the extraction of kinematic pa-

(a) (b)

Figure 2.1: The proposed BSN: (a) the actual configuration used for the data acquisition in the clinics; (b) in combination with the reflective markers of the optoelectronic reference system during the validation process.

rameters through the measurement of angular velocities, inclinations, and accelerations. These measurements are more accurate and reliable than measuring positions or displacements, which are derived from the formers and usually introduce additional errors in the data analysis. The Shimmer nodes are oriented trying to align the $x$ axis of the their reference system (shown in Figure 1.9 (a)) to the upward-downward direction, the $y$ axis to the right-left direction, and the $z$ axis with the antero-posterior direction.

The acquisition procedure followed in the clinic for the data collection is the following: in each trial, the examiner asks the patient to walk, at his/her preferred speed, in an obstacle-free environment for a variable distance between 7 m and 15 m and then to turn around and go back to the starting point. The acquisitions have been taken in different locations and, due to the lack of space, it has not always been possible to perform the G task walking continuously for at least 10 m, as the MDS suggests. However, even in the few cases in which the shortest distance (7 m) was traveled, the minimum number of complete gait cycles per leg was between 2 and 4 (after

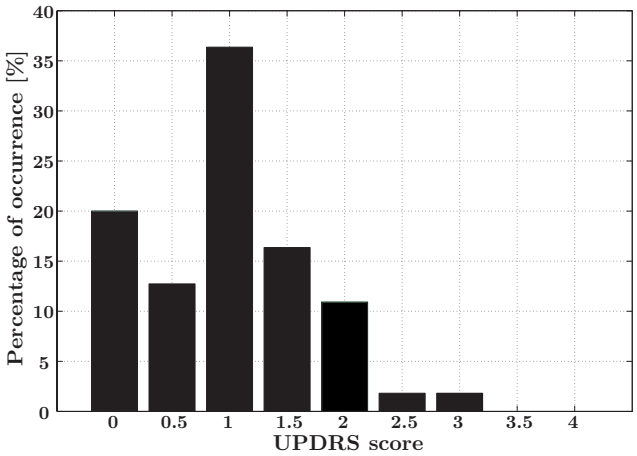


Figure 2.2: Distribution of the 55 UPDRS scores assigned to the G task trials.

discarding the acceleration and deceleration phases) in both directions, leading to a minimum total number of complete gait cycles per leg between 4 and 8 in the entire trial. The obtained results (presented in the following) show that this minimum number of gait cycles is sufficient to estimate accurately the gait parameters. Moreover, this number is consistent with the number of gait cycles considered in classical GA systems based on other technologies, which have usually a limited acquisition area.

The total amount of gait trials collected was 55 (from 34 Parkinsonians and 4 control subjects), as some PD patients performed the task on different medication states (ON/OFF) or in distinct acquisition sessions. In order to reduce the low-resolution effects caused by the discrete nature of the UPDRS and increase the homogeneity and the range of the assessment, the collected data have been evaluated by expert neurologists, using a non-integer scale with intermediate scores ($\cdot.5$) to label the trials in which the neurologists were undecided between consecutive (integer) UPDRS classes. All the exercise sessions were also recorded using a portable video camera for off-line manual controls. The distribution of the 55 UPDRS scores assigned to the G task trails is shown in Figure 2.2

For what concerns the validation procedure, synchronized inertial and optical data have been collected for a heterogeneous subset of 5 subjects, including both

healthy subjects (3) and Parkinsonians (2), using the testbed configuration shown in Figure 2.1 (b). Further details on the optoelectronic-based validation can be found in [30].

## 2.4 Gait Characterization

In this section, the methods used for the characterization of parkinsonian gait, in both time and frequency domains, are described.

### 2.4.1 Gait Features in the Time Domain

We first analyze gait patterns in the time domain. A novel algorithm for gait segmentation is proposed as the basis for the computation of spatio-temporal parameters and kinematic variables. Additional features based on the autocorrelation of the accelerometric signals are also considered in order to detect periodicity and symmetry in walking patterns.

#### Temporal Parameters

As extensively discussed in Section 1.3.2, despite its complexity, gait has a significant rhythmic and periodic component and it is possible to segment it in simpler blocks, called gait cycles. In order to identify them and all the other gait phases, it is necessary to accurately detect the $HS$ and $TO$ events, for both legs. To this end, we propose a novel approach, based on proper processing of accelerometric signals acquired by the chest-mounted IMU.

By following a heuristic approach, a preliminary visual investigation was performed manually detecting and labeling the $HS$ and $TO$ events in the inertial signals, using synchronized optoelectronic data as ground truth. We observed that $HS$ events are usually located in proximity of negative and positive peaks in vertical and frontal accelerations, respectively. Physically, this is due to the fact that, just before the $HS$ instant, the trunk reaches the maximum vertical acceleration intensity (with negative

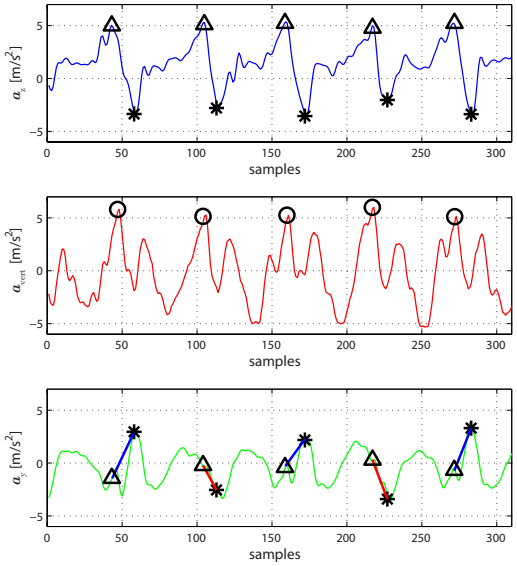


(a) Healthy Subject

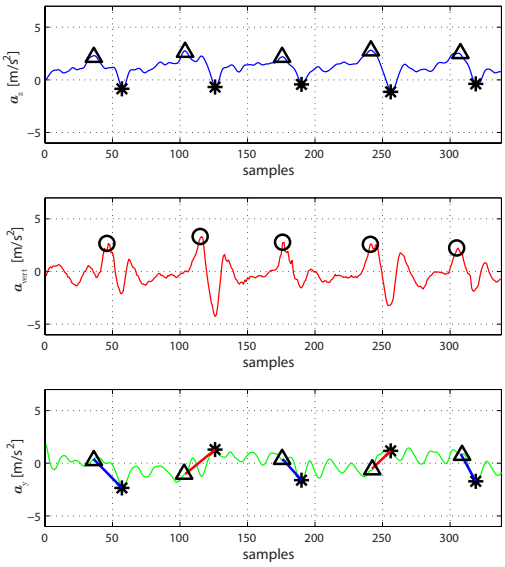


(b) PD Subject

Figure 2.3: Accelerometric signals recorded through the chest-mounted IMU for: (a) a healthy subject and (b) a PD patient with mild symptoms (UPDRS score equal to 1.5). Circles represents peaks in the linear vertical acceleration $a_{\text{vert}}$. Triangles and asterisks on the antero-posterior acceleration $a_z$ denote, respectively, $HS$ and $TO$ events. In the medio-lateral acceleration $a_y$ $HS$ points are connected with following $TO$ points by a line whose slope allows to discriminate left leg (blue line, positive slope) from right leg features (red line, negative slope).

sign because the body is falling toward the ground) and also the maximum frontal acceleration (because the body is moving forward and then suddenly decelerates after the foot contact). In a preliminary version of the algorithm [1], the negative peaks in vertical acceleration were chosen to estimate the $HS$ instants because the acceleration in the upward-downward direction is usually sharper and more robust to inter-subject variability of gait patterns than the one in the antero-posterior direction. In order to achieve a better $HS$ detection accuracy, the current version of the algorithm takes into account both vertical and frontal acceleration components. In particular, the peaks in a preprocessed version of the vertical acceleration have been used to define a limited region in which peaks in frontal acceleration, corresponding to the actual $HS$ events, are searched. The estimation of the $TO$ instants and the automatic labeling of the right/left events are performed considering the local minima after the $HS$s in the antero-posterior acceleration and the projection of $HS$s' and $TO$s' instants in the medio-lateral acceleration, respectively.

Two examples of typical trunk acceleration patterns for a healthy subject and a Parkinsonian are shown in Figure 2.3, where the interval between samples, denoted as $\Delta$, is equal to $\frac{1}{f} = 9.76$ ms, and the vertical, the medio-lateral, and the antero-posterior components of the acceleration are denoted as $\boldsymbol{a}_{\mathrm{x}}$, $\boldsymbol{a}_{\mathrm{y}}$, and $\boldsymbol{a}_{\mathrm{z}}$, respectively. Although accelerations in the normally walking subject are more defined and have wider excursions, the described signals characteristics can be easily observed also in the accelerometric data recorded for the PD patient. The automatic procedure used for the estimation of the $HS$ and $TO$ events can be detailed as follows. First of all, the raw accelerometric signals are low-pass filtered to reduce the high frequency noise component, using a fourth-order zero-lag Butterworth filter with bandwidth equal to 20 Hz. The raw accelerations measured by the IMU include always a component due to the gravity. In our case, an imperfect alignment of the sensors with the direction of the gravity may cause attenuation in the measured vertical acceleration $\boldsymbol{a}_{\mathrm{x}}$. In order to avoid this effect, the 3-dimensional orientation of the Shimmer node, in the Earth's frame (i.e., the reference system in which the $x$ axis points toward the magnetic north, the $y$ axis points toward east, and the $z$ axis points downward, toward the center of the Earth, according to the direction of the gravity), is estimated through the orientation

filter developed by Madgwick [27] and introduced in Section 1.2.4. The contribution of the gravity (9.81 m/s$^2$ in the $z$ axis) is then subtracted from the acceleration component in the Earth frame's $z$ axis: the effective linear vertical acceleration, denoted as $\boldsymbol{a}_{\text{vert}}$, is thus obtained. Since $\boldsymbol{a}_{\text{vert}}$ refers to the Earth frame, downward accelerations are positive, whereas upward accelerations are negative. For this reason, as shown in the second row of both plots in Figure 2.3, while the body is falling towards the ground (i.e., just before an $HS$ event) the values of $\boldsymbol{a}_{\text{vert}}$ reach positive peaks, which represent good candidates for estimating an approximate region in which the actual $HS$s should be searched. The first step of the peaks selection procedure in $\boldsymbol{a}_{\text{vert}}$ consists in low-pass filtering the signal (using a fourth-order zero-lag Butterworth filter with cut-off frequency set to 5 Hz) and in shifting it, by adding a quantity equal to the minimum value (with sign) of $\boldsymbol{a}_{\text{vert}}$ measured in the entire trial, in order to have only positive values. Moreover, since we observed that the highest peaks were always higher than 1 m/s$^2$, the obtained signal is squared to magnify further highest peaks. The resulting signal, denoted as $\boldsymbol{a}_{\text{preproc}}$, is analyzed to extract instants of the highest positive peaks, generally denoted as $\boldsymbol{peak}_{\text{vert}} = \{peak_{\text{vert}}(j)\}_{j=1}^{N_{peaks}}$, where $N_{peaks}$ is the number of highest peaks in the trial, which approximately identify the $HS$ instants. In particular, in order to detect only the correct peaks and discard those related to other gait cycle's phases (different from the $HS$ instants), the MATLAB function *findpeaks(data, 'MinPeakHeight',* $Th_{height}$*, 'MinPeakDistance',* $Th_{distance}$*)* is used, where: $data$ is the signal in which the peaks should be searched ($\boldsymbol{a}_{\text{preproc}}$ in this case); ('MinPeakHeight',$Th_{height}$) and ('MinPeakDistance',$Th_{distance}$) are (name, value) pair arguments, which impose constraints for refining the peaks' selection procedure. More specifically: the former imposes to consider as possible candidates for peak instants only the positive peaks in $\boldsymbol{a}_{\text{preproc}}$ with a height greater than a threshold, denoted as $Th_{height}$ (dimension: [m/s$^2$]), whereas all the others are discarded; the latter imposes that the distances (in terms of samples) between consecutive selected peaks, i.e., $\{peak_{\text{vert}}(j) - peak_{\text{vert}}(j-1)\}_{j=2}^{N_{peaks}}$, are larger than another threshold, denoted as $Th_{distance}$ (dimension: [s]), to avoid considering, as valid, peaks higher than $Th_{height}$ but pair-wise too close to represent consecutive $HS$ events.

The values of $Th_{height}$ and $Th_{distance}$ are chosen on the basis of experimental

observations of trunk acceleration patterns in both healthy and parkinsonian subjects and are set to 25% of the maximum value of $\boldsymbol{a}_{\text{preproc}}$, within a whole trial, and to 40 samples[3] (approximately 390 ms), respectively.

For each instant $peak_{\text{vert}}(j) \quad (j = 1,...,N_{peaks})$, the peaks in antero-posterior acceleration, coinciding with the actual $HS$ instants, are searched in the interval ($peak_{\text{vert}}(j) - 250$ ms, $peak_{\text{vert}}(j) + 50$ ms) and labeled as $\{peak_{HS}(j)\}$. Similarly, local minima in the antero-posterior acceleration are searched inside the interval ($peak_{HS}(j)$, $peak_{HS}(j) + 250$ ms). The nearest one, after $peak_{HS}(j)$, is selected as $TO$. The final step of the algorithms consists in labeling the detected $HS$s and $TO$s as events belonging to right or left gait cycles. To this end, the slope $m$ of the line passing through the value of the medio-lateral acceleration sample, corresponding to the instant of the first detected $HS$ (denoted as $HS_1$), and the value of the sample coinciding with the following $TO$ instant (denoted as $TO_1$), is considered. If $m \geq 0$, then a left gait cycle is starting, so that $HS_1$ is labeled as $HS_L$ and the contralateral $TO_1$ as $TO_R$; if $m \leq 0$, $HS_1$ is labeled as $HS_R$ and $TO_1$ as $TO_L$. The following $HS$ and $TO$ are labeled consequently, alternating right and left labels.

When the complete sequence of $HS$ and $TO$ instants is identified, the temporal parameters described in Section 1.3.2 can easily computed.

### Spatial Parameters

As for the temporal features, step/stride length and velocity are estimated using only the accelerometer placed on the chest. The computation of spatial parameters exploiting trunk-accelerometry is a widely studied topic. An comprehensive comparison between different step length estimators, relying on trunk-mounted accelerometers and various mathematical model for linking trunk movements with the forward displacement, is provided by Alvarez et al. in [90]. We chose to adopt, among the others, the approach proposed by Zijlstra [55], which simply considers human gait as an inverted pendulum in which the vertical displacement $h$ (dimension: [m]) of the Center of Mass (CoM) can be used to estimate the forward distance $D$ (dimension: [m])

[3] We reasonably assume that the time intervals between consecutive steps are always longer than 0.39 s for both healthy controls and PD patients.

traversed at each step. Usually, while a person is walking, the CoM lies within the pelvis but its movements have often been approximated using a sensor device placed in proximity of the second sacral vertebrae. In the same way, we assume that the vertical displacement of the sensor attached to the chest and the one of the CoM are similar. The relationship between vertical and forward displacements is given by the following equation:

$$D = 2K\sqrt{2\ell h - h^2} \tag{2.1}$$

where $\ell$ is the leg length (dimension: [m]) and $K$ is an empirically calibrated constant (adimensional). The vertical displacement $h$ can be obtained by double integration of the linear vertical acceleration $\boldsymbol{a}_{\text{vert}} = \{a_{\text{vert}}(i)\}_{i=0}^{N-1}$ (dimension: [m/s$^2$]), where $N$ is the length of the signal $\boldsymbol{a}_{\text{vert}}$. More precisely, the vertical velocity $\boldsymbol{v}_{\text{vert}} = \{v_{\text{vert}}(i)\}_{i=0}^{N-1}$ (dimension: [m/s]) of the trunk at the $i$-th sample can be computed as

$$v_{\text{vert}}(i) = v_{\text{vert}}(i-1) + a_{\text{vert}}(i)\Delta \quad i = 1,...,N-1$$

where: $v_{\text{vert}}(0)$ is assumed to be equal to 0; $\Delta$ corresponds the sampling period (dimension: [s]); and . Then, the position $\boldsymbol{p}_{\text{vert}} = \{p_{\text{vert}}(i)\}_{i=0}^{N-1}$ (dimension: [m]) of the trunk at the $i$-th sample can be expressed as

$$p_{\text{vert}}(i) = p_{\text{vert}}(i-1) + v_{\text{vert}}(i)\Delta \quad i = 1,...,N-1$$

where $p_{\text{vert}}(0)$ is set to 0. The position data $\boldsymbol{p}_{\text{vert}}$ are finally high-pass filtered (using a fourth-order zero-lag Butterworth filter with cut-off frequency set to 0.1 Hz), to remove integration drift, and the total displacement amplitude is then calculated as the difference between the maximum and the minimum values of the trunk position during each step cycle (i.e., the time interval between the $HS$ of one foot and the $HS$ of the other foot). Considering the $k$-th gait cycle, the vertical displacement of the trunk for the right step ($h_R(k)$, dimension: [m]) can be given by the following expression:

$$h_R(k) = \max_{i=HS_R(k)}^{HS_L(k)} p_{\text{vert}}(i) - \min_{i=HS_R(k)}^{HS_L(k)} p_{\text{vert}}(i)$$

where $HS_R(k)$ ($HS_L(k)$) indicates the first sample of the $k$-th $HS$ for the right (left) leg. The value of the vertical displacement during a left step ($h_L(k)$) can be calculated in the same way. The step lengths ($StepL_{R/L}$) are estimated using (2.1). The step velocities ($StepV_{R/L}$) are obtained from the step lengths and the duration of the step cycles. The parameters associated to strides, namely, $SL_{R/L}$ and $SV_{R/L}$, are obtained by adding the values of the features associated with the right and left steps for each gait cycle, as shown in Figure 1.11. Finally, all the values for the spatial parameters, which are initially calculated in meters, are expressed as percentage of the height of the considered subject–this is an expedient for minimizing errors related to different leg lengths.

### Additional Features

*Thigh's Range of Rotation*

Useful information for the clinical evaluation of gait, beside those provided by spatio-temporal parameters, can be obtained by measuring joint angles and segment inclinations in lower limbs [91]. The used sensor configuration (including one node per thigh) allows us to retrieve only the data regarding the flexion/extension of the thighs. In this case, the signal acquired by the gyroscopes of the IMUs placed on the thighs is used. The measured angular velocity can be integrated, during each gait cycle, in order to find the instantaneous (relative) inclination angle of the thighs' segments. From the thigh angular velocity signal $\omega = \{\omega(i)\}_{i=0}^{N_\omega-1}$ (dimension: [deg/s]), where $N_\omega$ is the length of the signal $\omega$, and the sampling period $\Delta$, the value of the angle $\theta = \{\theta(i)\}_{i=0}^{N_\omega-1}$ (dimension: [deg]) can be calculated for the $i$-th sample using a discrete integration method:

$$\theta(i) = \theta(i-1) + \omega(i)\Delta \qquad i = 1,...,N_\omega - 1.$$

The initial angle $\theta(0)$, at the beginning of each cycle, is set to zero. The Range of Rotation (RoR) (dimension: [deg]) of the right thigh, denoted as $Thigh\ RoR_R$, within the $k$-th gait cycle, is assumed to be equal to the difference between the maximum

and the minimum values of the instantaneous angle, i.e.:

$$Thigh\ RoR_R(k) = \max_{i=HS_R(k)}^{HS_R(k+1)} \theta(i) - \min_{i=HS_R(k)}^{HS_R(k+1)} \theta(i).$$

$Thigh\ RoR_L$ can be calculated in the same way. Additionally, we measured, for each gait cycle, the maximum value of the angular velocity, denoted as Max $\omega_{R/L}$, for both thighs.

*Autocorrelation-based Features*

Further insights on gait characteristics, such as its symmetry and regularity, can be derived from the periodic properties of body movements during walking. In [92], the autocorrelation of accelerometric signals, recorded with a trunk-mounted sensor, has been used for extracting intuitive but meaningful gait features. A brief overview of the algorithm used to calculate these parameters is now presented.

The raw autocorrelation coefficient $A$ of the linear vertical trunk acceleration $\boldsymbol{a}_{\text{vert}}$, defined as the sum of the products between each sample $a_{\text{vert}}(i) \quad (i = 0, 1, ..., N-1)$ and its time lagged replication $a_{\text{vert}}(i+m)$, is computed as follows:

$$A(m) = \sum_{i=1}^{N-|m|} a_{\text{vert}}(i) a_{\text{vert}}(i+m)$$

where the lag parameter $m$ represents the phase shift (in terms of samples) and may be any positive integer smaller than $N$. The unbiased[4] autocorrelation can be calculated dividing $A(m)$ by the number of samples representing the overlapping part of the time series and the time-lagged replication, i.e.:

$$A_{\text{unbiased}}(m) = \frac{A(m)}{N-|m|}.$$

The autocorrelation $A_{\text{unbiased}}(m)$ is shown for both (a) a healthy subject and (b) a PD patient (UPDRS score equal to 2) in Figure 2.4. Only the right half portion of the

[4]We use the unbiased autocorrelation to avoid the attenuations in amplitudes due to the increasing value of the lag parameter $m$ that occur in the biased version of the autocorrelation.

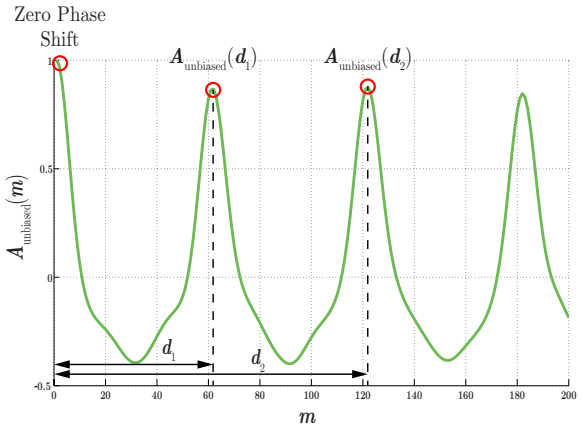


(a)

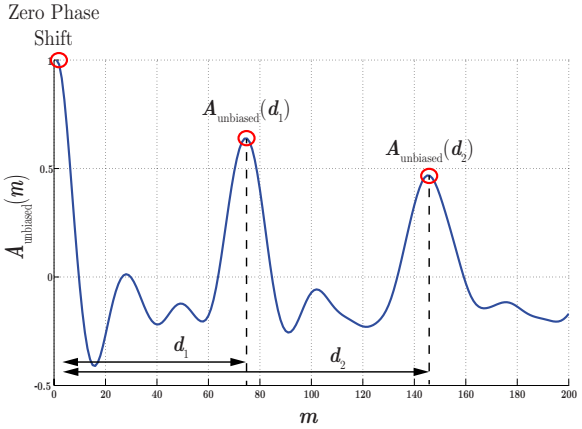


(b)

Figure 2.4: Unbiased autocorrelation sequences computed from the vertical trunk acceleration for: (a) a healthy subject and (b) a PD patient (UPDRS equal to 2).

autocorrelation sequence, properly normalized to 1, has been considered because of its symmetry with respect to the zero phase shift.

In both subfigures, it can be observed that, besides the maximum at the zero phase shift ($m = 0$), the amplitude of the autocorrelation coefficient presents several peaks for increasing values of $m$. The peak after the zero phase shift represents the

first dominant period $d_1$ and the phase shift associated with the steps periodicity. The amplitude of the autocorrelation coefficient in this point, denoted as $A_{\text{unbiased}}(d_1)$, is representative of the regularity of the vertical acceleration signal between steps. This is due to the fact that the amplitude of the autocorrelation at a certain point will be large if the original signal presents regular patterns with a periodicity similar to the phase shift corresponding to the considered point. Similarly, the peak after $d_1$ indicates the second dominant period $d_2$, which corresponds to the stride phase shift. The value of the autocorrelation $A_{\text{unbiased}}(d_2)$ is representative of the stride regularity.

Starting from the values of $A_{\text{unbiased}}$ in $d_1$ and $d_2$, the following features can be derived:

- Cadence ($C$) (dimension: [steps/minute]): number of steps per minute. In particular:

$$C = \frac{60f}{d_1}$$

  where $f$ is the sampling rate (dimension: [sample/s]) at which the accelerometer signal has been recorded (see Section 2.3.1).

- Regularity ($R$) (adimensional): representative of the periodicity of the subject's steps/strides. In particular:

$$R_{\text{step}} = A_{\text{unbiased}}(d_1)$$

$$R_{\text{stride}} = A_{\text{unbiased}}(d_2).$$

  The closer to 1 $R_{\text{step/stride}}$, the higher the regularity in steps/strides.

- Symmetry ($S$) (adimensional): ratio between step and stride regularities. In particular:

$$S = \frac{A_{\text{unbiased}}(d_1)}{A_{\text{unbiased}}(d_2)}.$$

  Values of $S$ close to 1 indicate a high symmetry between steps and strides.

### 2.4.2 Gait Features in the Frequency Domain

Features computed in the time domain are extremely useful for providing detailed information to physicians, especially on a stride by stride scale. An analysis in the frequency domain, instead, similarly to those derived by the autocorrelation, can be more representative of the overall characteristics related to a whole gait trial.

For simplicity, the estimated vertical linear acceleration ($\boldsymbol{a}_{\text{vert}}$), the lateral ($\boldsymbol{a}_{\text{y}}$), and antero-posterior ($\boldsymbol{a}_{\text{z}}$) components of the trunk acceleration are considered for the computation of frequency domain features. The signals are preliminary filtered with a fourth-order zero-lag Butterworth filter with bandwidth equal to 20 Hz and properly segmented in order to exclude initial and final acceleration/deceleration phases and to avoid the introduction of additional noise. The Discrete Fourier Transforms (DFTs) of the signals are computed using a Fast Fourier Transform (FFT) algorithm for each GT trial. Considering the linear vertical acceleration $\boldsymbol{a}_{\text{vert}}$, the $k$-th component of the spectrum $\boldsymbol{X}_{a_{\text{vert}}} = \{X_{a_{\text{vert}}}(k)\}_{k=0}^{N-1}$ can be computed as follows:

$$X_{a_{\text{vert}}}(k) = \sum_{n=0}^{N-1} a_{\text{vert}}(n) e^{-jk\frac{2\pi}{N}n} \qquad k = 0,\ldots,N-1.$$

The corresponding amplitude spectrum, denoted as $\boldsymbol{X}_{\text{ampl},a_{\text{vert}}}$, is obtained by dividing the absolute value of $\boldsymbol{X}_{a_{\text{vert}}}$ by $N$:

$$\boldsymbol{X}_{\text{ampl},a_{\text{vert}}} = \frac{|\boldsymbol{X}_{a_{\text{vert}}}|}{N}.$$

In the same way, the spectra of the lateral ($\boldsymbol{X}_{a_{\text{y}}} = \{X_{a_{\text{y}}}(k)\}_{k=0}^{N-1}$) and the antero-posterior ($\boldsymbol{X}_{a_{\text{z}}} = \{X_{a_{\text{z}}}(k)\}_{k=0}^{N-1}$) accelerations can be computed.

In Figure 2.5, the amplitude spectra $\boldsymbol{X}_{\text{ampl},a_{\text{vert}}}$, $\boldsymbol{X}_{\text{ampl},a_{\text{y}}}$, and $\boldsymbol{X}_{\text{ampl},a_{\text{z}}}$, associated with all the 55 G task trials, are shown. The spectra have been grouped according to the UPDRS score assigned to the trials by neurologists and sorted in ascending order (from UPDRS 0 to 3). It can be observed that spectrum amplitude peaks are centered in correspondence to step frequency (approximately around 2 Hz) and their magnitudes tend to decrease moving from low to high UPDRS values (from left to right): the higher the UPDRS, the "less powerful" the movement. This intuitive consideration can be translated into a new feature representative of the "power" of the

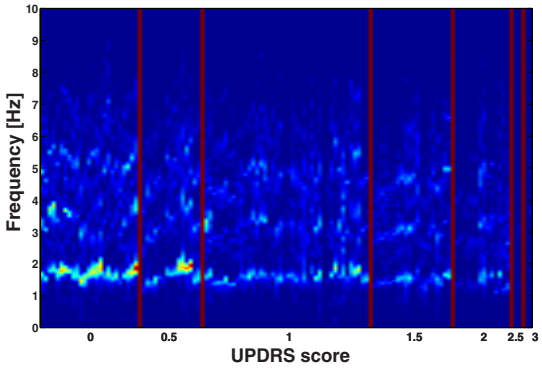


(a) $\boldsymbol{X}_{\text{ampl},a_{\text{vert}}}$

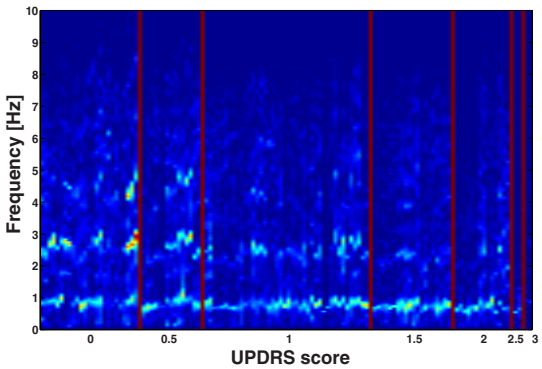


(b) $\boldsymbol{X}_{\text{ampl},a_{\text{y}}}$

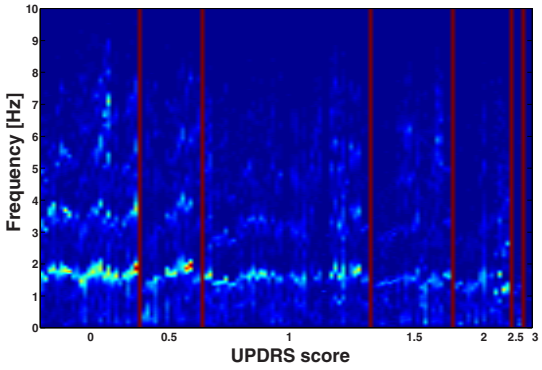


(c) $\boldsymbol{X}_{\text{ampl},a_{\text{z}}}$

Figure 2.5: Visual representation of the amplitude spectra of all the 55 gait trials for: (a) the linear vertical trunk acceleration $\boldsymbol{a}_{\text{vert}}$, (b) the lateral trunk acceleration $\boldsymbol{a}_{\text{y}}$, and (c) the frontal trunk acceleration $\boldsymbol{a}_{\text{z}}$. Each vertical line correspond to a trial, which are sorted in ascending order and grouped by UPDRS scores (from 0 to 3), separated by a vertical red line. The magnitude of the spectrum is mapped to a color that ranges from blue (lowest values) to red (highest values).

movement. For the signal $a_{\text{vert}}$, we define the spectrum power $P_{a_{\text{vert}}}$ as follows:

$$P_{a_{\text{vert}}} \triangleq \frac{1}{N}\sum_{k=0}^{N-1}(X_{a_{\text{vert}}}(k))^2.$$

Similarly, the spectrum powers of $\boldsymbol{X}_{\text{ampl},a_y}$, denoted as $P_{a_y}$, and of $\boldsymbol{X}_{\text{ampl},a_z}$, denoted as $P_{a_z}$, are computed. Finally, the feature $P_{\text{sum}}$, which takes into account the power of all the components, is computed as follows:

$$P_{\text{sum}} = P_{a_{\text{vert}}} + P_{a_y} + P_{a_z}.$$

### 2.4.3 Overall Features

In Table 2.1 and Table 2.2, a summary of the 29 features computed with the methods described in the previous section is provided for ease of readability.[5]

## 2.5 Results and Discussion

### 2.5.1 System Validation

In order to estimate the accuracy and the reliability of the considered features, a validation procedure has been carried out comparing the parameters extracted through the precessing of inertial signals with those computed using the gold standard opto-electronic reference system (Vicon). In particular, the estimation errors, defined as the difference between the values obtained by the IMU-based and the ground truth system, of spatio-temporal parameters have been analyzed, as shown in Table 2.3. The average error for the detection of $HS$ and $TO$ instants is equal to approximately 10 ms (1 sample considering the sampling rate equal to 102.4 Hz) and it is comparable or, in same cases, better than the one obtained with other approaches, based on both trunk-mounted IMUs [56, 55] and sensors placed on lower limbs [59, 61, 84]. Moreover, this error seems to be systematic and could be corrected in a later stage.

[5] For some features, only the formula associated with the right leg is shown. The formula for the left leg is straight forward.

Table 2.1: Summary of the considered spatio-temporal parameters.

| Feature | Dimension | Formula |
|---|---|---|
| | Temporal Features | |
| Gait Cycle Time: the time interval between the $HS$ of a foot to the next $HS$ of the same foot. | s | $GCT_{R/L}(k) = HS_{R/L}(k+1) - HS_{R/L}(k)$ |
| Stance Time: portion of the GCT during which a foot is in contact with the ground. | % | $ST_{R/L}(k) = 100 \times \frac{TO_{R/L}(k) - HS_{R/L}(k)}{GCT_{R/L}(k)}$ |
| Swing Time: portion of the GCT during which a foot is not in contact with the ground. | % | $SW_{R/L}(k) = 100 - ST_{R/L}(k)$ |
| Initial Double Support: portion of the GCT during which both feet are in contact with the ground (in the first step of the gait cycle). | % | $IDS(k) = 100 \times \frac{TO_L(k) - HS_R(k)}{GCT(k)}$ |
| Terminal Double Support: portion of the GCT during which both feet are in contact with the ground (in the second step of the gait cycle). | % | $TDS(k) = 100 \times \frac{TO_R(k) - HS_L(k)}{GCT(k)}$ |
| Double Support: total portion of the GCT during which both feet are in contact with the ground. | % | $DS(k) = IDS(k) + TDS(k)$ |
| Limp: difference between IDS and TDS in the same gait cycle (absolute value). | % | $Limp(k) = \lvert IDS(k) - TDS(k) \rvert$ |
| | Spatial Features | |
| Stride Length: distance travelled during a complete gait cycle. | % of subject's height | $SL(k) = StepL_R(k) + StepL_L(k)$ |
| Stride Velocity: the average linear velocity of a foot during a gait cycle. | % of subject's height/s | $SV(k) = \frac{SL(k)}{GCT(k)}$ |
| Step Length: distance traveled from the $HS$ of one foot to the $HS$ of the contralateral foot (step cycle). | % of subject's height | $StepL_{R/L}(k) = K2\sqrt{2\ell h_{R/L}(k) - h_{R/L}(k)^2}$ |
| Step Velocity: the average linear velocity of a foot during a step cycle | % of subject's height/s | $StepV_R(k) = \frac{StepL_R}{HS_L(k) - HS_R(k)}$ |

Table 2.2: Summary of the additional features computed in the time domain and those extracted in the frequency domain.

| Additional Features | | |
|---|---|---|
| Thigh Range of Rotation: maximum flexion/extension excursion of the thighs. | deg | $Thigh \;\; RoR_R(k) = \max_{i \in GCT_R(k)} \theta(i) - \min_{i \in GCT_R(k)} \theta(i)$ |
| Maximum Angular Velocity: maximum value of a thigh's angular velocity in a gait cycle. | deg/s | $\text{Max } \omega_R(k) = \max_{i \in GCT_R(k)} \omega(i)$ |
| Cadence: step number per minute. | steps/minute | $C = \frac{60f}{d_1}$ |
| Step Regularity: measure representative of step periodicity. | adimensional | $R_{\text{step}} = A_{\text{unbiased}}(d_1)$ |
| Stride Regularity: measure representative of stride periodicity. | adimensional | $R_{\text{stride}} = A_{\text{unbiased}}(d_2)$ |
| Symmetry: ratio between step and stride regularity. | adimensional | $S = \frac{A_{\text{unbiased}}(d_1)}{A_{\text{unbiased}}(d_2)}$ |
| **Features in the Frequency Domain** | | |
| Spectrum Power for the linear vertical acceleration. | adimensional | $P_{a_{\text{vert}}} = \frac{1}{N}\sum_{k=0}^{N-1}(X_{a_{\text{vert}}}(k))^2$ |
| Spectrum Power for the mediolateral acceleration. | adimensional | $P_{a_{\text{y}}} = \frac{1}{N}\sum_{k=0}^{N-1}(X_{a_{\text{y}}}(k))^2$ |
| Spectrum Power for the anteroposterior acceleration. | adimensional | $P_{a_{\text{z}}} = \frac{1}{N}\sum_{k=0}^{N-1}(X_{a_{\text{z}}}(k))^2$ |
| Total Spectrum Power. | adimensional | $P_{\text{sum}} = P_{a_{\text{vert}}} + P_{a_{\text{y}}} + P_{a_{\text{z}}}$ |

Given the accuracy in the detection of the fundamental gait events, it is straight forward that also the derived temporal parameters are highly accurate, showing an error which can be considered negligible for the purpose of this work. For what concerns spatial parameters, the performance of the developed system is aligned to step/stride length estimators presented in the literature, even though, in our case, the analysis has been performed on both healthy persons and PD patients. The validation of thighs' inclination has already been performed in [30], showing a very good correlation (Pearson's correlation coefficient equal to 0.98) between thighs' angles computed with the IMUs and the Vicon system. Features based on the autocorrelation and computed in the frequency domain have not been considered in the validation process, since the optoelectronic system is not able to compute them directly and, thus, is no possible to do a valid comparison.

Table 2.3: Estimation errors for relevant spatio-temporal parameters.

| Parameter | Mean | STD |
|---|---|---|
| $HS$ | 8.22 ms | 17.6 ms |
| $TO$ | 6.83 ms | 26.33 ms |
| $GCT_R$ | 0 ms | 13.81 ms |
| $GCT_L$ | 16.27 ms | 28.74 ms |
| $ST_R$ | -0.03 % | 3.46 % |
| $ST_L$ | -1.62 % | 1.23 % |
| $DS$ | -0.55 % | 4.63 % |
| $C$ | 0.7 steps/min | 1.8 steps/min |
| $SL$ | 4.23 cm | 4.94 cm |

### 2.5.2 Features Analysis

In order to achieve the ultimate goal of defining a protocol for the automatic UPDRS evaluation of gait in Parkinsonians, in this section, the relationship between the computed gait features and the UPDRS scoring by clinicians is investigated.

In Figure 2.6 (a), a radar plot representing the values of all the 29 features, averaged over all trials belonging to each UPDRS class and properly normalized between 0 and 1 (the maximum value of each feature corresponds to 1), is shown. It can be observed that some of the displayed parameters reveal clear monotonic trends as functions of the UPDRS score. For ease of visualization, in the following we consider only a subset of the 29 features, trying to maintain the relevant information about the gait characteristics and reducing redundancy, since features associated to similar measures show similar trends. The parameters with right and left components have been replaced with the arithmetic average of the two values. For instance, the new feature $GCT_{\text{mean}}$ is computed by averaging $GCT_R$ and $GCT_L$. The resulting subset consists in 11 features, namely $\{GCT_{\text{mean}}, ST_{\text{mean}}, DS, Limp, SL, StepV_{\text{mean}}, C, R_{\text{step}}, S, Thigh\ RoR_{\text{mean}}, P_{\text{sum}}\}$. The average values of the features in the reduced set, averaged, over all trials, for each UPDRS class, are shown in Figure 2.6 (b) through a radar plot.

For both the complete and the reduced sets of features, it is possible to observe that the values of temporal parameters, such as $GCT$, $ST$, and $DS$, are generally increasing accordingly to the UPDRS class, as observed also in [84]. It is intuitive that subjects with gait impairments tend to walk more slowly, to remain longer in the stance and double support phases, and, consequently, to be able to perform less steps in fixed time interval (lower values in cadence $C$). Furthermore, in the plots it can be noticed that some features belonging to UPDRS class 3 show values in contrast with the expected trend. This is due o the fact that subjects who present *festinating gait*, i.e., an alteration in gait pattern typical of Parkinsonians, characterised by a quickening and shortening of normal strides, perform short steps with a very high cadence, thus leading to low values of temporal parameters even for high UPDRS scores. Spatial features and the variables related to the thighs' range of movements show clear decreasing trends for increasing values of the UPDRS score, with a consistent reduction between values belonging to UPDRS class 0 and those of UPDRS classes 2.5 or 3. This result is consistent with clinical observations of Parkinsonian walking, in which patients with increasing gait impairments perform shorter steps, with reduced velocity and reveal, in general, a more limited movement range in lower

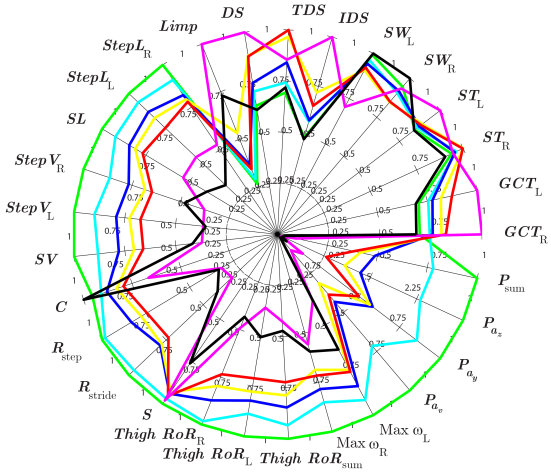


(a)

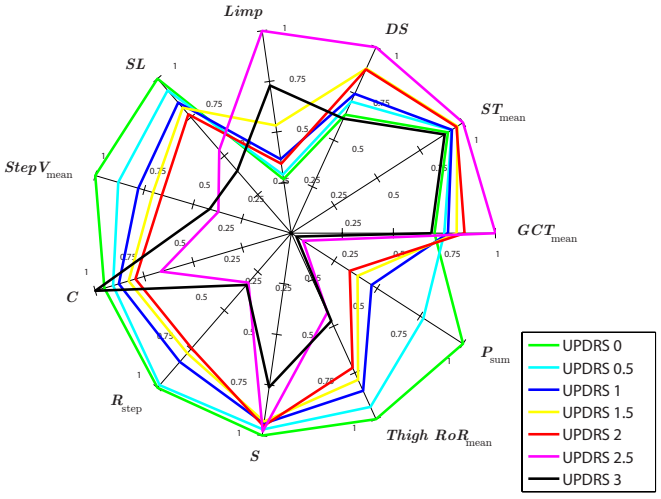


(b)

Figure 2.6: Average normalized values, for each UPDRS class, of: (a) all the estimated features; (b) the reduced set of gait parameters.

limbs [93, 94]. In the same way, $R_{\text{step/stride}}$, which is a feature representative of the homogeneity of the rhythmic component of gait, tends to decrease of almost 70% from normal walking subjects to patients with high UPDRS score. The symmetry of walking, expressed by the feature $S$, maintains, instead, a low variability across all UPDRS classes, except for the UPDRS 3 subject: this seems to be more related to the single subject walking characteristics than to the entire scoring cluster. The features extracted in the frequency domain show a high correlation with the UPDRS score, with a clear monotonic decreasing trend and a range excursion of almost 95% between the lowest (0) and the highest (3) UPDRS classes. This behavior is due to the fact that the overall "power" related to the subject's movements during the G task decreases consistently when the amplitude, the velocity, the symmetry, and the regularity of steps is reduced.

In Figure 2.7, two illustrative examples of pair of features which allow to identify clear "parametric trajectories" linked to the UPDRS scoring are presented. In both plots, each point, whose coordinates are given by the pair of features considered, corresponds to a trial and is colored in accordance to the UPDRS score assigned to the patient. For each UPDRS score cluster, the centroid is denoted by a star marker (of the same color of its UPDRS class). Furthermore, all centroids are connected by a black piece-wise line, which highlights the parameters' trend for increasing UPDRS scores. Finally, the (red) exponential curve, obtained by minimum mean square error fitting and representing a smoothed version of the centroids' trajectory, is also shown. The first figure (Figure 2.7 (a)) shows, on the same 2-dimensional plane, all the stride length/power sum pairs $\{(SL_i, P_{\text{sum},i})\}_{i=1}^{55}$ for all gait trials. A smooth trajectory toward the bottom-left corner for increasing values of the UPDRS score can be noticed, since both stride length and spectrum total power decrease. Similarly, in Figure 2.7 (b) the pairs $\{(R_{\text{step,i}}, Thigh\ RoR_{\text{mean},i})\}_{i=1}^{55}$ are shown on the same 2-dimensional plane. The centroids identify a sharp decreasing trajectory toward the bottom-left corner, which corresponds to a more limited thighs range of movements and a lower step regularity. The presence of a few outliers in both plots is partially attributable to the fact that neurologists take into account, for the assignment of the UPDRS score, also other qualitative observations, such as the arms swing, which

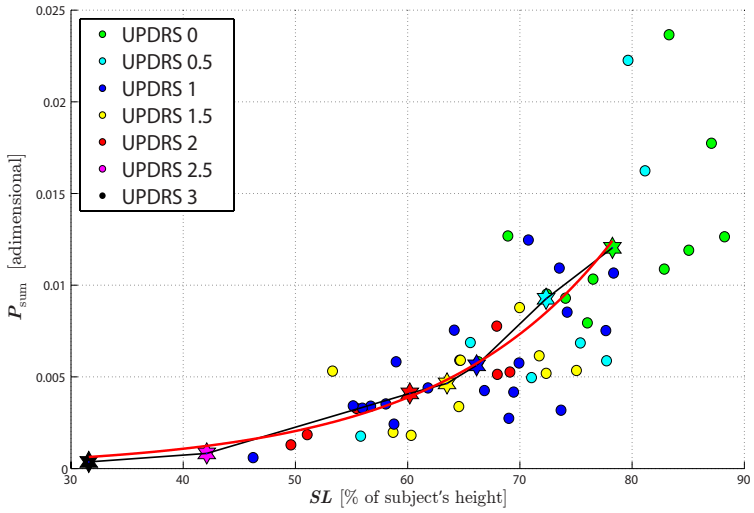


(a)

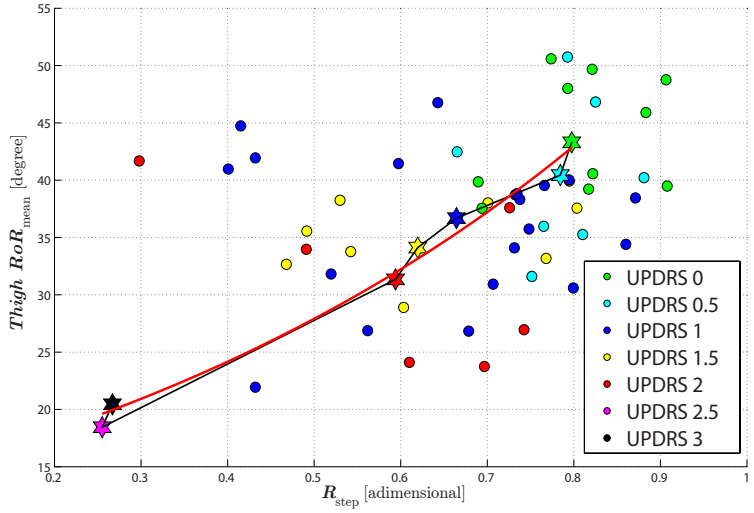


(b)

Figure 2.7: 2-dimensional visualization of pair of features in relation to the UPDRS scores. In (a) the $\{(SL_i, P_{\text{sum},i})\}_{i=1}^{55}$ pairs are considered while in (b) the $\{(R_{\text{step},i}, Thigh\ RoR_{\text{mean},i})\}_{i=1}^{55}$ pairs are displayed. Each point represents a single G task trial and is colored in accordance to its UPDRS score. The centroids of the UPDRS score clusters are shown as colored stars and linked with a black piece-wise line. The red curve is a smoothed (exponential) version of the piece-wise line.

cannot be recorded with the used BSN.

These findings show that there is strong relationship between many of the features computed with the proposed inertial BSN and the UPDRS evaluation by neurologists. Motivated by this, in the next section, we investigate the feasibility of a classification system for the automatic UPDRS assessment of the G task in PD patients.

### 2.5.3 Automatic UPDRS Evaluation

Following a common approach used in machine learning, we further processed the 11-element subset of parameters using Principal Component Analysis (PCA), which allows us to reduce data dimensionality while retaining most of the variability (i.e., information content) of the initial data [95]. Then, we used both the original and PCA-projected feature datasets and the UPDRS scores by the neurologists for the supervised training of an automatic classification system. Three well-know classifiers, in increasing order of complexity, have been considered: Nearest Centroid Classifier (NCC), $k$ Nearest Neighbors ($k$NN), and Support Vector Machine (SVM) [95]. A brief description of the approach used by each method for the classification of a new (unlabeled) sample is given in the following.

- NCC: the new point is labeled with the same label of the nearest centroid. Euclidean distances between pairs of points are considered. To this end, centroids must be computed for all training samples of each class.

- $k$NN: the new point is assigned to the class which includes the majority of the $k$ nearest (in terms of Euclidean distances) neighbors of the sample point. The nearest neighbors are searched among all training samples, thus, the computational efficiency of this method decreases with increasing values of $k$. In the case of tie-breaks, (i.e., when two or more classes contain the same number of samples among the k nearest neighbors), the closest point is used to break the tie and its class is then chosen.

- SVM: the label of the new sample is determined by considering the decision region in which the point lies. These multi-dimensional space partitions are

defined, during a training phase, by considering the hyperplane that maximizes the separation between the training samples belonging to two different classes. Since in our problem we deal with more than two classes. the training procedure needs to be repeated for each pair of classes, using multiple one-vs-all steps for the definition of the separation hyperplanes.

The performance analysis of the automatic system has been carried out considering: (i) all the combination of the 11 features;[6] (ii) increasing number of the principal components (from 1 to 11). When the $k$NN classification method is used, the considered value of $k$ ranges from 0 to 10. In order to avoid overfitting and to increase the generality of the evaluation, a leave-one-out cross-validation method has been adopted. It consists in using each point of the original dataset, in turn, as the new (unknown) point to be classified, while training the classifier with the remaining points.

The output of the classification procedure is an estimated UPDRS score, denoted as $\widehat{u}$ for each sample corresponding to a G task trial. The absolute UPDRS classification error is defined as follows:

$$e \triangleq |\widehat{u} - u|$$

where $u$ is the actual UPDRS score assigned to trials by a neurologist.

In Figure 2.8 (a), the average (over all the possible parametric configurations) Cumulative Distribution Functions (CDFs) of the error $e$, obtained by using each classifier on both original and PCA-projected data are shown. The Area under the Curve (AuC) is selected as a representative performance metric. It can be observed that, on average, almost all the classification methods achieve similar results. The best accuracy is reached by the $k$NN algorithm applied on the original dataset, closely followed by SVM and NCC on the same dataset. The use of PCA seems to slightly worsen the classification performance. The CDF which maximizes the AuC, i.e., guarantees the best performance, corresponds to the system using $k$NN, with $k = 6$, on the subset of features $\{ST_{\text{mean}}, StepV_{\text{mean}}, S\}$. With this configuration, the system classifies cor-

[6] We considered the reduced set of features for convenience but experimental results showed that performing the same analysis on the entire set of features does not increase the classification performance.

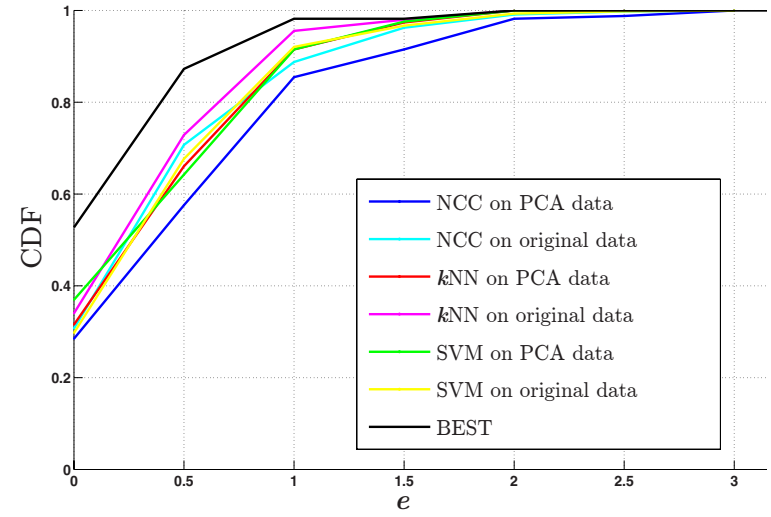


(a)

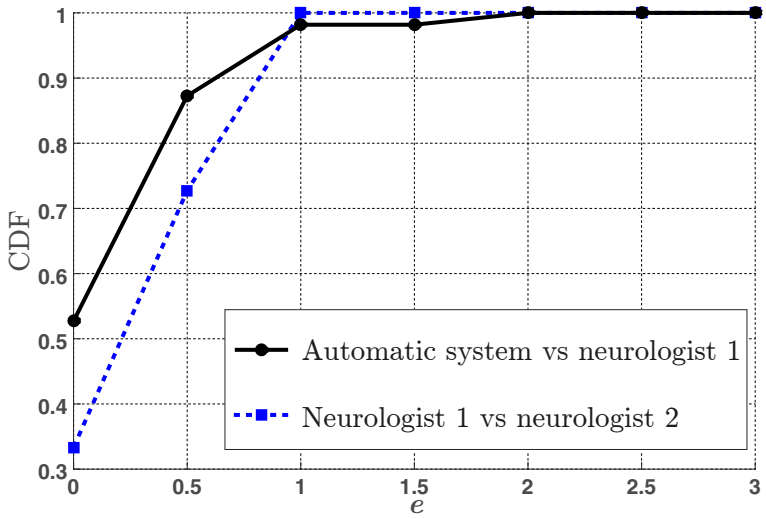


(b)

Figure 2.8: (a) Average CDFs of the absolute error $e$ evaluated applying NCC, $k$NN, and SVM on both original and PCA-projected data. The black solid line represents the best CDF, obtained using $k$NN on the combination of features ($ST_{mean}$, $StepV_{mean}$, $S$) and with $k$ = 6. (b) Comparison between the CDF of the automatic classification error $e$ (i.e., the absolute difference between the (best) score by the automatic system and the score by one of the neurologists) and the absolute difference in the UPDRS scoring between two neurologists.

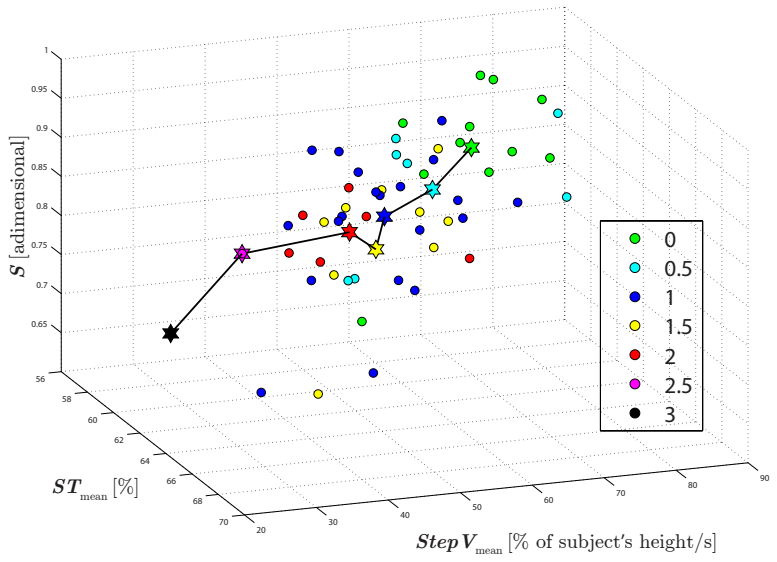


Figure 2.9: 3-dimensional representation of the points $\{(ST_{\text{mean},i}, StepV_{\text{mean},i}, S_i)\}_{i=1}^{55}$ associated with the features that achieved the best performance. Each point represents a single GT trial and is colored in accordance to its UPDRS score. The centroids of the UPDRS score clusters are shown as colored stars and linked by a black piece-wise line.

rectly (with $e = 0$) approximately 53% of the trials and with $e \leq 1$ almost the entire set of G task samples (about 98%).

An attempt to graphically visualize, in a 3-dimensional space, the features triplets $\{ST_{\text{mean},i}, StepV_{\text{mean},i}, S_i\}_{i=1}^{55}$, which allow to achieve the best classification performance show by the black solid line in Figure 2.8 (a), is shown in Figure 2.9. Each point corresponds to a trial and centroids are calculated by averaging the features' values among samples belonging to the same UPDRS class. Even though the trajectory identified by the centroids is not as smooth as the trajectories in Figure 2.7, a clear trend emerges and allows a good separation between UPDRS classes.

To better understand the impact of these results in a clinical setting, in Figure 2.8 (b), the CDF of the error $e$, defined as the (absolute) difference between the UPDRS scores assigned by the automatic system and the neurologist, is compared with the

CDF of the (absolute) difference $d$ between the UPDRS evaluations by two different neurologists. The latter curve, in particular, is representative of the inter-rater variability and shows a perfect accordance between the two physicians only in 34% of the cases, although the maximum difference between the two evaluations is always below one UPDRS score. Similarly, the error between the automatic system and the neurologist is below one and equal to 0 (no error) in 98% and 53% of the cases, respectively. This demonstrate that the performance achieved by the developed system compares favorably with typical inter/intra-rater variability which can affect neurologists' decisions while assigning UPDRS scores to PD patients [80]. In other words, the proposed automatic classification system is "accurate" enough to mimic the evaluation performance of medical personnel and is suitable for real-world clinical and tele-health applications.

## 2.6 Conclusion

In this chapter, an exhaustive analysis of gait in Parkinsonians have been presented. A simple BSN formed by three wearable IMUs has been used for computing a complete set of features, in both time and frequency domains. In particular, a novel algorithm for gait phases segmentation and the estimation of temporal parameters, relying on a single trunk-mounted accelerometer, has been developed and validated. An in-depth investigation of the connection between the measured kinematic variables and the UPDRS scores assigned to patients by neurologists has been carried out, showing a strong relationships between some gait parameters, such as $SL$, $StepV$, $R_{\text{step}}$, $Thigh\ ROR$ and $P_{sum}$, and the patient's impairments level, accordingly to clinical observations. Finally, an automatic UPDRS scoring system, able to assign an estimated UPDRS score mimicking the evaluation criteria of physicians, has been developed through well-known machine learning techniques. The achieved performance compares favorably with the inter/intra-rater variability observed between different neurologists. Obviously, further investigations on the accuracy and the reliability of the proposed system (using a larger set of patients, a more uniform distribution of scores across all the UPDRS classes, and additional evaluations by more neurolo-

gists) should be required to make the performance analysis more meaningful from a statistical point of view. Nevertheless, the obtained results show that the designed system can provide an added value to the clinical evaluation of the PD, in both clinics and at patients' home. For example, the development of a telemedicine systems for remote monitoring of PD patients could allow the quantitative measurement of motor fluctuations multiple times throughout the day (unlike the usual time-limited evaluation performed in the clinics), providing the neurologists with a more reliable clinical "picture" of the patient and allowing more accurate symptoms' assessment and management. Moreover, the possibility to integrate in the same system the automatic evaluation of different UPDRS tasks through the same simple BSN, represents a key point for the deployment of practical applications in a real-world e-health scenario. In the next chapter, the extension of our approach to multiple UPDRS tasks is discussed.

# Chapter 3

# Kinematic Characterization and Comparative Outlook of UPDRS scoring in Multiple Motor Tasks for PD

*I often say now I don't have any choice whether or not I have Parkinson's, but surrounding that non-choice is a million other choices that I can make.*

– Michael J. Fox

In Chapter 2, a novel approach for an in-depth characterization of gait in Parkinsonians have been presented. It relies on a simple BSN, formed by only 3 IMUs, for the extraction of a complete set of gait features and on machine learning techniques for the implementation of an automatic assessment tool, able to assign an estimated UPDRS score to patients' motor performance, following the evaluation criteria of neurologists. The main strength of the designed system, beside its low-complexity, is its flexibility. In this chapter, always within the context of the *VRehab* project (see Section 2.1.3, we extend the analysis carried out for the G task to two additional

UPDRS items, namely the Leg Agility (LA) and the Sit-to-Stand (S2S) tasks, giving particular emphasis to their kinematic characterization, to the performance evaluation of the automatic scoring system, to the comparative analysis of the three tasks, and, finally, to the opportunities that such a system can offer in the context of telemedicine.

## 3.1 Introduction

In Section 2.1.1, we have pointed out that the current strategies used for managing PD motor symptoms, such as those based on the use of dopaminergic drugs, are often inadequate and worsen their efficacy over time, introducing in some cases motor complications which can affect patient's independence more than the disease itself. An accurate and continuous monitoring of the symptoms' progression and treatment effect might help to increase therapies' efficacy but, currently, most of the clinical evaluations are carried out through sporadic and qualitative observations of patient's motor impairment level in the clinics, which provide physicians just a limited and inaccurate picture of the actual disease progression. A more objective evaluation can be achieved using semi-quantitative rating scales, such as the UPDRS, described in Section 2.1.2 but, even exploiting these tools, many drawbacks remain. Among the others, an important limitation of current evaluation methods is the inability to monitor and accurately quantify changes in motor symptoms' severity across a long time frame, which is fundamental for fully charactering the patient's response to medications and adjusting the therapy consequently, minimizing the undesired effects. To this end, the approach presented in the previous chapter for the G task case, represents a suitable solution because it is able to quantitatively characterize motor performance and symptoms severity, in an automatic and nn-invasive way, which would allow multiple evaluation sessions across the day and would provide a more detailed and up-to-date view on the patient's condition. Obviously, by including in the evaluation different functional motor tasks, a wider and more detailed description of the disease status can be achieved. In this chapter, in addition to the G task, the LA and the S2S tasks are considered.

### 3.1.1 The Leg Agilit, Sit-to-Stand, and Gait UPDRS Tasks

The LA, Arising from Chair,[1] and G tasks correspond to the items 3.8, 3.9, and 3.10 of the MDS-UPDRS document [79].

The choice of these particular tasks was influenced by the need to keep the BSN as simple as possible, maximizing at the same time the number of tasks which could be analyzed without changing the sensors' placement. The selected tasks are particularly suitable for the considered unified analysis and clinically relevant for a comprehensive evaluation of the patients' symptoms, as they refer to different aspects of PD (for example, LA is related to bradykinesia while S2S and G are associated with posture/deambulation symptoms). The evaluation of UPDRS motor tasks is usually performed without the support of any technological instrument so that the neurologist assesses the task in a qualitative way and relies especially on his/her experience and training. Therefore, assessments may vary from neurologist to neurologist (inter-rater variability) or from one to another evaluation session by the same neurologist (intra-rater variability) [80]. In the following, a brief description of each task is provided.

#### Leg Agility Task

Table 3.1: UPDRS mapping for LA task.

| UPDRS | Amplitude | Hesitations | Interruptions | Slowing | Freezing |
|---|---|---|---|---|---|
| 0 | nearly constant | no | 0 | 0 | 0 |
| 1 | decrements near the end | slight | $\geq 1$ | 1,2 | 0 |
| 2 | decrements midway | mild | - | 3,4,5 | 0 |
| 3 | decrements after first tap | moderate | - | $\geq 6$ | $\geq 1$ |
| 4 | always minimal or null | severe | - | always | - |

In the LA task, the patient is asked to sit on a chair provided with rigid backrest and armrests. The patient must place both his/her feet on the floor in a comfortable position. The exercise consists in alternately raising up and stomping the feet on the ground, as high and as fast as possible. Ten repetitions per leg must be performed

[1] For consistency other works in the literature [96, 97], in the following we denote the Arising from Chair task as S2S task.

while sitting on the chair in order to test each leg separately (in the following, we will distinguish between Right LA (RLA) and Left LA (LLA) tasks).[2] The examiner should first train the patient, showing him/her the correct execution of the exercise, stopping as soon as the patient starts. The significant parameters that have to be measured, independently for each leg, are the speed, the regularity, and the amplitude of the movement. In Table 3.1, an attempt to map the characteristics of the LA task, which the examiner should consider for the assessment of the patient's performance, to the UPDRS scores is shown. We recall that UPDRS scores are integers values, ranging from 0, which means that the patient is able to perform the task normally and with no impairments, to 4, which means that the patient has severe difficulties in performing the exercise or is not able to perform it at all.

### Sit-to-Stand Task

Table 3.2: UPDRS mapping for S2S task.

| UPDRS | Failed attempts | Use of armrests | Slowing | Move forward on chair |
|---|---|---|---|---|
| 0 | 0 failed attempts | no | no | no |
| 1 | $\geq 1$ failed attempts | no | yes | yes |
| 2 | 0 failed attempts | yes | - | - |
| 3 | $\geq 1$ failed attempts | yes | - | - |
| 4 | not able to stand up alone | | | |

In the S2S task, the patient is asked to sit on a straight-backed chair with armrests. The exercise consists in crossing the arms across the chest (in order to avoid their use in the movement) and getting up from the chair. In the case of failure, the patient can retry to raise up to two more times. If still unsuccessful, the patient can move forward on the chair to facilitate the movement or, in case of another failure, he/she can use the armrests to stand up. After a maximum of three failed trials, the patient can move forward on the chair to facilitate the movement. If the patient is still not able to stand up, he/she is allowed to push off using his/her hands on the armrests. After a maximum of three unsuccessful trials with the help of the arms, the examiner can

[2] When not specified, LA refers to the general task, including both RLA and LLA trials.

eventually help the patient to stand up. The mapping between the key characteristics of the S2S task and UPDRS scores is shown in Table 3.2.

### Gait Task

Table 3.3: UPDRS mapping for G task.

| UPDRS | Independent walking | Impairments level |
|---|---|---|
| 0 | yes | no impairments |
| 1 | yes | minor impairments |
| 2 | yes | substantial impairments |
| 3 | no | assistance device needed for safe walking |
| 4 | no | cannot walk at all or only with another person's assistance |

The description of the G task and the main aspects that the examiner should take into account for assigning an UPDRS score in this task have been provided in Section 2.1.4. Similarly to the LA and S2S cases, a possible mapping between the task characteristics and the UPDRS evaluation is shown in Table 3.3.

## 3.1.2 Chapter Contribution

Unlikely the majority of the existing literature, in which UPDRS tasks are analyzed singularly, in this chapter we focus on the comparative evaluation of the LA, S2S, and G tasks. The same approach uses for the study of the G task has been extended to the LA and S2S tasks, through an experimental analysis of the data from 34 PD patients and the UPDRS evaluations of three expert neurologists [2, 4]. A common, low-complexity BSN, formed by three IMUs (two on the thighs and one on the chest) has been used for characterizing the considered tasks by extracting and analyzing the kinematic features associated with their typical movement patterns, in both time and frequency domains. The most relevant features has been identified and analyzed for quantifying the motor performance of patients belonging to the different UPDRS classes. The extracted features and the subjective evaluations by neurologists have been then used to train an automatic UPDRS scoring system, with the aim to automatically assess the patients' motor performance matching as closely as possible the

medical evaluation criteria. The performance of the automatic assessment has been analyzed and discussed proposing a comparative outlook with the inter-neurologist assessment. We have also investigated the correlation between the UPDRS scores assigned to the tasks by both the neurologists and our automatic system, introducing a an aggregate UPDRS score as a significant concise metric which can provide additional information to neurologists for deriving insights on the overall level of impairments of patients and on the relative "weight" of each task in the assessment of the gravity of the symptoms. Finally, the feasibility of an application for remote rehabilitation and monitoring of PD patients in a tele-medicine environment is discussed and a possible efficient implementation approach is proposed.

## 3.2 Related Work

In Section 1.3.2, we have pointed out how the kinematic analysis of specific motor tasks through different motion capture and sensing technologies, such as optoelectronic systems and inertial-based BSN, has been widely studied for various clinical applications. In recent years, the spread of inexpensive and accurate wearable devices is boosting the interest of the medical community in these kind of systems. With regard to PD, most of the research studies, from both a medical and an engineering perspective, has focused on the kinematic characterization of single motor tasks, the quantification of motor complications severity, such as tremors and dyskinesia, and/or on the evaluation of patients' performance in different PD conditions (On/OFF states). For what concerns the considered tasks, the G task has been widely studied, as shown in Section 2.2, whereas just a few works on the LA [98, 99, 100, 30] and the S2S [101, 97, 96] tasks are present in the literature. To the best of our knowledge only limited attention has been devoted to investigation of the relationship between different UPDRS tasks characterized through motion capture technologies. In [102], the correlations between lower extremity functional performance and the UPDRS scores has been investigated for early-stage Parkinsonians, showing that UPDRS motor and total scores may be good predictors of overall lower extremity function. Stochl et al. [103] investigated the structure of PD symptoms in terms of the motor symptom

evaluations defined in UPDRS - Part III. Five main latent symptoms factors were identified and the correlations between the UPDRS scores assigned to the various tasks were reported. Similarly, in [104] a statistical analysis of the UPDRS motor scores was performed, using classical evaluation methods by neurologists and considering PD patients in both ON (i.e., the intervals during which the medication is effective) and OFF (i.e., the intervals during which the medication is not effective) conditions, in order to identify latent relationships between UPDRS tasks and combine the tasks in "macro-groups" related to similar PD symptoms. Five of these groups, denoted as "factors," have been identified (namely, gait/posture, tremor, rigidity, left extremities bradykinesia, and right extremities bradykinesia). The correlations (i) between the UPDRS scores assigned by neurologists to the introduced "macro-groups" of tasks and (ii) between them and an aggregate UPDRS score are also presented, showing that the macro-groups can be assessed separately and provide information about different aspects of the disease. In our opinion, a comparative analysis of multiple UPDRS tasks, based on a unified approach for both the kinematic characterization and the automatic UPDRS scoring, can be interesting in order to highlight their relationship with the different aspects of the PD and their contribution in the overall evaluation of the disease progression.

## 3.3 Experimental Set-up

### 3.3.1 Hardware

The BSN designed for the acquisition of the inertial signals used for the characterization of the LA, S2S, and G tasks is formed by three Shimmer 2r nodes, one on the chest and one per thigh, attached to the body with Velcro straps and it is shown in Figure 3.1. We remark that the sensing platform, the devices' positioning, the acquisition framework, and the setting configuration are the same used for analyzing singularly the G task, as explained in Section 2.3.

The placement of the sensors has been chosen taking into account two main motivations: (i) the need to analyze the three tasks without changing the configuration of the nodes in order to minimize the patients' stress and simplify the acquisition

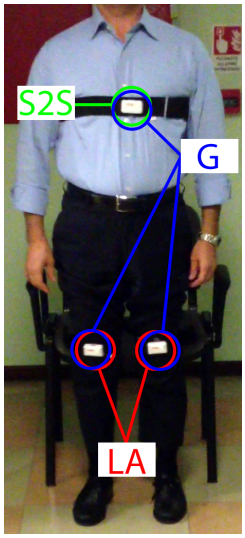


Figure 3.1: The inertial BSN designed for the evaluation of the three UPDRS tasks of interest (LA, S2S, G): the subsets of nodes used in each task are marked with different colors.

procedure, allowing sequential execution of the three tasks; (ii) the higher accuracy and reliability of IMUs in measuring inclinations and accelerations, rather than positions or displacements. With the current BSN configuration, indeed, all the kinematic parameters in the LA and S2S tasks are extracted from inclination and/or angular velocities measured with the nodes on the thighs and on the chest, respectively; at the opposite, in the G task, the majority of the features are extracted from acceleration signals directly measured by the sensor placed on the trunk.

### 3.3.2 Validation

As for the G task, the data acquired with the inertial BSN and the extracted kinematic features have been compared with those measured with the Vicon optoelectronic system, for validation purposes, also in the LA and S2S tasks. In [30], we have first demonstrated the equivalence between heel' and thigh' kinematics. More precisely, the three-dimensional orientations of the Shimmer nodes placed on the thighs are estimated, with reference to the Earth frame, through the Madgwick orientation es-

timation filter (see Section 1.2.4). For each leg, the orientation component in the sagittal plane, corresponding to the inclination $\theta$ (dimension: [deg]) of the thigh, is extracted, together with the thigh's angular velocity $\omega$ (dimension: [deg/s]). These signals are then compared to those estimated with the optoelectronic system, taking into account the angles and the angular velocities extracted by the three-dimensional position of reflective markers placed on the subject's heels. The obtained results show a very high correlation between the two measurements (approximately equal to 0.98), motivating the use of $\theta$ and $\omega$ for the kinematic characterization of the LA task. The same approach has been applied, in the S2S task, for determining the correlation between trunk inclinations estimated with the IMU and those extracted from the optical reference system, showing similar results [96]. The validation of the parameters used for the characterization of the G tasks has been discussed in Section 2.5.1. In general, the signals/parameters extracted through the IMUs and the Vicon system have a very high level of correspondence and can be considered accurate enough for the purposes of this work.

### 3.3.3 Subjects

For maintaining the consistency with the analysis performed for the G task, the set of subjects considered in this extended work has been kept unchanged and consists in 34 PD patients (22 males and 12 females). The average age is equal to 67.4 years (ages between 31 and 79 years) with a standard deviation equal to 11.6 years wheres the average Modified Hoehn and Yahr Scale score for the subjects was 1.6 (standard deviation equal to 0.47, minimum score score equal to 1, maximum score equal to 3) on the 1-to-5 scale (higher scores indicate more severe impairments and more advanced stages of the disease).

### 3.3.4 Acquisition Procedure

The positioning of the sensors on the patient's bosy is shown in Figure 3.1. We tried to align the the $x$, $y$, and $z$ axes of the Shimmer 2r node's coordinate reference system, shown in Figure1.9 (a), to the upward-downward, right-left, and forward-backward

directions, respectively. In order to help clinicians to correctly align the nodes to the patient's anatomical structure, the developed acquisition software has been provided with a functionality that allows to check the sensors' placement: if the alignment is within a confidence range (heuristically defined), the examiner is allowed to proceed in the acquisition procedure; otherwise, a warning message is shown and the procedure is stopped until the sensors' placement is correctly modified by the examiner.

The data acquisitions were carried out by asking the patient to execute the LA, S2S, and the G tasks sequentially. In each task, only the signals recorded by a proper subset of nodes of the BSN were considered—the subsets of Shimmer devices used for the evaluation of the single tasks are shown in Figure 3.1 using different colors. For the LA task acquisitions, only the two devices placed on the thighs were used, whereas for the S2S task only the trunk-mounted node was considered. In the G task, all the BSN IMUs were used to achieve a complete characterization of the complex gait movement.

A total of 47 (94 for the LA task, considering separately RLA and LLA) acquisitions per task has been collected from the 34 patients, since some of them performed the sequence of tasks in distinct PD conditions (ON/OFF states) or at different times corresponding to different motor fluctuation phases. Under these conditions, indeed, the motor performance of a same subject and, consequently, its evaluation by the physicians, may vary in such a consistent way that considering each trial as an independent sample does not introduce bias in the analysis. Although the number of patients has been kept the same considered in the previous chapter for the single evaluation of the G task, we remark that in the multi-task analysis the number of recorded trials has decreased from 55 to 47 for two reasons: (i) the 4 control patients included in the previous work have not been considered in the unified analysis; (ii) we kept only the trials in which the sequence of task, namely, LA, S2S, and G, was execute correctly.

The UPDRS evaluation of the collected trials has been carried out independently by three neurologist with expertise in movement disorders. A non-inter scale, with intermediate scores ($\cdot.5$), has been used–this allows the clinicians to increase the evaluation range and to label the trials in which they were undecided between consecutive

(integer) UPDRS classes. The consensus score, denoted as $\text{UPDRS}_{\text{Mean}}$, is defined as the arithmetic average of the scores assigned by the three neurologists to each trial, rounded to the nearest (integer or intermediate) UPDRS value. This methodology has been already used in the literature to combine the assessments of multiple neurologists in a single concise score [105], enhancing the robustness of the evaluation and reducing the distortion caused by the inter-rater variability [80].

The distributions of the UPDRS scores assigned by the three neurologists to the 47 trials and the related $\text{UPDRS}_{\text{Mean}}$ are shown in Figure 3.2. By observing the figure, it is possible to notice slight difference among the evaluation criteria used by the neurologists. In particular, neurologist 1 uses more than the other two the intermediate scores, whereas neurologist 2 tends to assign higher scores than the other two in the LA task. Moreover, the distribution of the UPDRS scores in the 3 tasks seems to be a Gaussian-like distribution centered in correspondence to a dominant UPDRS class, which depends on both the neurologist and the task. Finally, the distribution of the $\text{UPDRS}_{\text{Mean}}$ score, as expected, is smoother than the UPDRS scores of the single neurologists and the scores in the LA, S2S, and G tasks show Gaussian-like distributions centered in 1.5, 0.5, and 1 respectively. In a statistically "ideal" scenario, the distribution should be uniform across all the UPDRS classes. Obviously, in the real case this is very unlikely because patients with high levels of motor impairments (high UPDRS classes) have more difficulties in going to the clinics for undergoing the assessment sessions.

## 3.4 Kinematic Features Extraction

In the following, a concise description of the features' extraction procedure for each of the considered tasks is provided.

### 3.4.1 LA Task

The movement involved in the LA task can be accurately described using both the inclination ($\theta$, dimension: [deg]) and the angular velocity ($\omega$, dimension: [deg/s]) of the thighs in the sagittal plane, measured by the Shimmer nodes on the legs. An

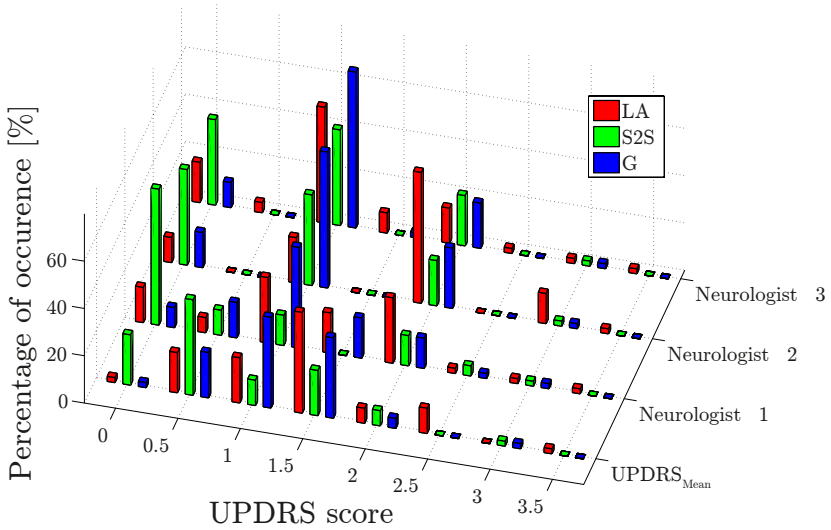


Figure 3.2: Trials distribution for all the considered tasks.

illustrative portion of the inclination signal $\theta$ of one thigh, for two consecutive LA repetitions, denoted as $r$-th and $(r+1)$-th ($r \in \{1,2,\ldots,9\}$), is shown in Figure 3.3. Through an automatic segmentation procedure, three fundamental time epochs, denoted as $t_S(r)$, $t_E(r)$, and $t_P(r)$ and associated, respectively, with the start, the end, and the epoch of maximal thigh inclination of the $r$-th LA repetition, are identified. Starting from these epochs, various parameters can be straightforwardly calculated. The results obtained in [30] have shown that, in the time domain, the most relevant features for the kinematic characterization of the LA task are: the angular amplitude $\Theta$ (dimension: [deg]); the angular speed of execution $\Omega$ (dimension: [deg/s]); the pause between consecutive executions $P$ (dimension: [s]); the regularity of execution $R$ (dimension: [s]); and the repetition frequency $F$ (dimension: [Hz]). In the frequency domain, upon the computation of the amplitude spectra of the Discrete Fourier Transforms (DFTs) of $\theta$ and $\omega$, denoted as $X_\theta$ and $X_\omega$, respectively, the powers of the inclination spectrum ($P_{X_\theta}$) and the angular velocity spectrum ($P_{X_\omega}$) have been identified as the most relevant features. Further details on the parameters extraction procedure in the LA task can be found in [30].

In Table 3.4, the expressions used for computing, the $r$-th repetition, the most

Table 3.4: Summary of the most relevant features considered for the LA task. The names of the parameters taken into account for the experimental results are marked in bold. In the last column, the correlation coefficients between the features and the $\text{UPDRS}_{\text{Mean}}$ score are shown (the best for each task is highlighted in bold). Correlation coefficients ($r$-values) with associated $p$-values (not shown here) greater than 0.05 are considered as non significant (n.s.).

| Name | Definition | Dimension | $r$-value |
|---|---|---|---|
| Angular amplitude | $\Theta(r) \triangleq \frac{\Theta_{\text{A}}(r)+\Theta_{\text{D}}(r)}{2}$ | [deg] | n.s. |
| **Angular speed of execution** | $\Omega(r) \triangleq \frac{\Theta_{\text{A}}(r)+\Theta_{\text{D}}(r)}{T(r)}$ | [deg/s] | **-0.50** |
| **Pause of execution** | $P(r) \triangleq t_{\text{S}}(r+1) - t_{\text{E}}(r)$ | [s] | 0.27 |
| **Regularity of execution** | $R(r) \triangleq t_{\text{P}}(r+1) - t_{\text{P}}(r)$ | [s] | 0.49 |
| **Repetition frequency** | $F \triangleq \frac{10}{t_{\text{E}}(10)-t_{\text{S}}(1)}$ | [Hz] | -0.36 |
| **Thigh inclination spectrum power** | $P_{X_\theta} \triangleq \frac{1}{N}\sum_{h=0}^{N-1}\left(X_{\theta,h}\right)^2$ | adimensional | -0.46 |
| **Thigh angular velocity spectrum power** | $P_{X_\omega} \triangleq \frac{1}{N}\sum_{h=0}^{N-1}\left(X_{\omega,h}\right)^2$ | adimensional | -0.34 |

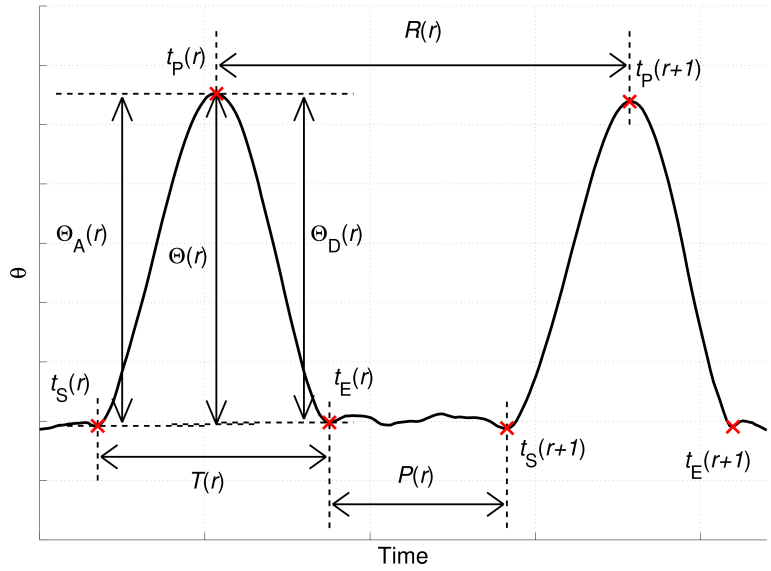


Figure 3.3: Typical pattern in the inclination signal $\theta$ of one thigh during the LA task for two consecutive repetitions. The fundamental time events are denoted with red crosses and the intuitive representation of the most relevant features is also shown.

meaningful parameters in the LA task are shown. When not specified, in the following we refer to the average values of the features $\Theta$, $\Omega$, $P$, and $R$, obtained by averaging, over all consecutive repetitions, the values measured in each repetition and denoted, respectively, as $\Theta_{\text{mean}}$, $\Omega_{\text{mean}}$, $P_{\text{mean}}$, and $R_{\text{mean}}$.

### 3.4.2 S2S Task

The characterization of the S2S task, given its simplicity, relies only on the inclination signal estimated through the chest-mounted sensor. As for the thighs' nodes in the LA task, the three-dimensional orientation of the Shimmer device placed on the trunk is estimated and the inc $\theta$lination of the torso in the sagittal plane, denoted as $\theta$ (dimension: [deg]), is measured, as described in details in [96]. In Figure 3.4, the typical shape of the trunk inclination signal during the S2S task is shown. The characterization of the movement is achieved by identifying, through a simple automatic segmentation procedure, the following time labels: (i) the starting epoch $t_{\text{S}}$ of the S2S (i.e., when the chest starts bending forward); (ii) the epoch of maximal bending of the chest $t_{\text{P}}$ (placed around the middle of the S2S exercise); and (iii) the ending epoch $t_{\text{E}}$ of the S2S (i.e., when the chest returns in the vertical position). Starting from these key instants, 12 features, shown in Table 3.5, have been calculated. In particular, the features refer to the duration $T$ (dimension: [s]), the angular amplitude $\Theta$ (dimension: [deg]), and the speed of execution $\Omega$ (dimension: [deg/s]) of the S2S exercise. Moreover, the difference $D$ between the forward and the backward bending phases is computed for all the considered variables. In [96], the subset of features, among the 12 extracted, which has turned out to be the most significant for the characterization of the S2S task, includes $T$, $T_{\text{B}}$, $T_{\text{F}}$, $D_T$, $\Theta$, and $\Omega$ (highlighted in bold in Table 3.5).

### 3.4.3 G Task

The movements involved in the G task are inherently more complex than those associated with LA and S2S tasks and, for this reason, the characterization of gait through kinematic features is more challenging. In Chapter 2, an in-depth analysis of the G task in PD patients has been presented, considering features in both time and fre-

Table 3.5: Summary of the most relevant features considered for the S2S task (see the caption in Table 3.4 for the details of the used notation and column values' interpretation).

| Name | Definition | Dimension | $r$-value |
|---|---|---|---|
| **Forwards bending duration** | $T_{\mathrm{F}} \triangleq t_{\mathrm{P}} - t_{\mathrm{S}}$ | [s] | 0.58 |
| **Backwards bending duration** | $T_{\mathrm{B}} \triangleq t_{\mathrm{E}} - t_{\mathrm{P}}$ | [s] | 0.56 |
| **Total duration** | $T \triangleq T_{\mathrm{F}} + T_{\mathrm{B}} = t_{\mathrm{E}} - t_{\mathrm{S}}$ | [s] | **0.62** |
| **Forwards/backwards duration difference** | $D_T \triangleq T_{\mathrm{F}} - T_{\mathrm{B}}$ | [s] | 0.47 |
| Forwards bending amplitude | $\Theta_{\mathrm{F}} \triangleq \theta(t_{\mathrm{P}}) - \theta(t_{\mathrm{S}})$ | [deg] | 0.35 |
| Backwards bending amplitude | $\Theta_{\mathrm{B}} \triangleq \theta(t_{\mathrm{P}}) - \theta(t_{\mathrm{E}})$ | [deg] | 0.25 |
| **Average bending amplitude** | $\Theta \triangleq \frac{\Theta_{\mathrm{F}} + \Theta_{\mathrm{B}}}{2}$ | [deg] | 0.33 |
| Forwards/backwards bending amplitude difference | $D_\Theta \triangleq \Theta_{\mathrm{F}} - \Theta_{\mathrm{B}}$ | [deg] | 0.20 |
| Forwards bending speed | $\Omega_{\mathrm{F}} \triangleq \frac{\Theta_{\mathrm{F}}}{T_{\mathrm{F}}}$ | [deg/s] | -0.33 |
| Backwards bending speed | $\Omega_{\mathrm{B}} \triangleq \frac{\Theta_{\mathrm{B}}}{T_{\mathrm{B}}}$ | [deg/s] | -0.21 |
| **Average bending speed** | $\Omega \triangleq \frac{\Theta_{\mathrm{F}} + \Theta_{\mathrm{B}}}{T} = \Omega_{\mathrm{F}} \frac{T_{\mathrm{F}}}{T} + \Omega_{\mathrm{B}} \frac{T_{\mathrm{B}}}{T}$ | [deg/s] | -0.32 |
| Forwards/backwards bending speed difference | $D_\Omega \triangleq \Omega_{\mathrm{F}} - \Omega_{\mathrm{B}}$ | [deg/s] | -0.14 |

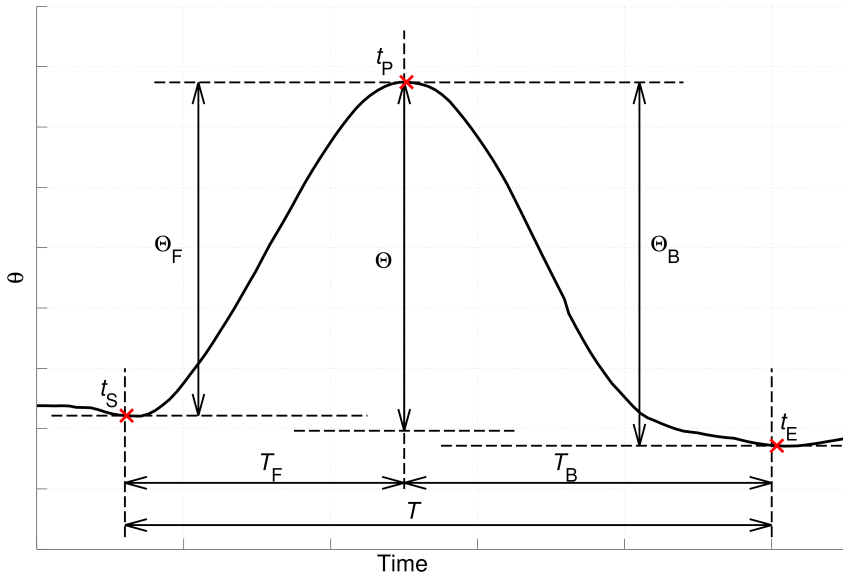


Figure 3.4: The torso inclination signal $\theta$ during the S2S task. The time instants corresponding to the starting epoch, the epoch of maximal bending of the chest, and the ending epoch are represented with red crosses. The intuitive representation of the most relevant kinematic features is also shown.

Table 3.6: Summary of the most relevant features considered for the G task (see the caption in Table 3.4 for the details of the used notation and column values' interpretation).

| **Name** | **Definition** | **Dimension** | ***r*-value** |
|---|---|---|---|
| Gait Cycle Time | $GCT_{R/L}(k) = HS_{R/L}(k+1) - HS_{R/L}(k)$ | [s] | 0.30 |
| **Stance Time** | $ST_{R/L}(k) \triangleq 100 \times \frac{TO_{R/L}(k) - HS_{R/L}(k)}{GCT_{R/L}(k)}$ | % of GCT | n.s. |
| Initial Double Support | $IDS(k) \triangleq 100 \times \frac{TO_L(k) - HS_R(k)}{GCT(k)}$ | % of GCT | 0.29 |
| Terminal Double Support | $TDS(k) \triangleq 100 \times \frac{TO_R(k) - HS_L(k)}{GCT(k)}$ | % of GCT | n.s. |
| **Double Support** | $DS(k) \triangleq IDS(k) + TDS(k)$ | % of GCT | n.s. |
| **Limp** | $Limp(k) \triangleq \lvert IDS(k) - TDS(k) \rvert$ | % of GCT | 0.30 |
| Step Length | $StepL_{R/L}(k) \triangleq K2\sqrt{2\ell h_{R/L}(k) - h_{R/L}(k)^2}$ | % of height | -0.59 (mean) |
| **Stride Length** | $SL(k) \triangleq StepL_R(k) + StepL_L(k)$ | % of height | **-0.60** |
| **Step Velocity** | $StepV_R(k) \triangleq \frac{StepL_R}{HS_L(k) - HS_R(k)}$ | % of height/s | -0.59 |
| **Thigh Range of Rotation** | $Thigh\ \ RoR_R(k) \triangleq \max_i \theta(i) - \min_i \theta(i) \quad i \in GCT_R(k)$ | [deg] | -0.49 |
| **Cadence** | $C \triangleq \frac{60f}{d_1}$ | [steps/minute] | n.s. |
| **Step Regularity** | $R_{\text{step}} \triangleq A_{\text{unbiased}}(d_1)$ | adimensional | -0.58 |
| **Symmetry** | $S \triangleq \frac{R_{\text{step}}}{R_{\text{stride}}}$ | adimensional | n.s. |
| Spectrum power for accelerations | $P_{a_{\text{vert/y/z}}} \triangleq \frac{1}{N}\sum_{k=0}^{N-1}(X_{a_{\text{vert/y/z}},k})^2$ | adimensional | -0.38 (mean) |
| **Total spectrum power** | $P_{\text{sum}} \triangleq P_{a_{\text{vert}}} + P_{a_y} + P_{a_z}$ | adimensional | -0.43 |

quency domains. Some of the most representative are shown in Table 3.6. Among a total number of 29 parameters, only a subset of 11 elements, marked in bold in the table, has been considered for the final characterization of the task. The reduced set of features for the G task is the following: $\{GCT_{\text{mean}}, ST_{\text{mean}}, DS, Limp, SL, StepV_{\text{mean}}, C, R_{\text{step}}, S, Thigh\ RoR_{\text{mean}}, P_{\text{sum}}\}$.

### 3.4.4 Automatic Classification Approach

As highlighted at the beginning of this chapter (Section 3.1), one of the main goal of the proposed system is to provide a tool for the automatic UPDRS evaluation of the considered motor tasks, based on the assessment of the relevant kinematic features outlined in Section 3.4. To this end, a well-known supervised machine learning approach has been used for the data analysis, the training and the validation of a classification system, and the evaluation of its performance. In the following, the details of the used techniques are given.

#### Principal Component Analysis

The relevant kinematic features characterizing each task may be partially correlated and the information they provide on the task of interest may be redundant. In order to reduce the features' dimensionality and redundancy, while retaining most of the information content of the original data, Principal Component Analysis (PCA) is applied on the collections of kinematic features defined for each task. Before applying PCA, the original data are first centered at their means (which are set equal to 0) and rescaled to have unit standard deviation. For the automatic classification procedure presented in the following, both original and "PCA-projected" data will be considered as input.

#### Classification Algorithms and Performance Anaysis

The supervised learning approach used for the training of the automatic UPDRS evaluation system relies on the use of the consensus UPDRS score ($\text{UPDRS}_{\text{Mean}}$), i.e., on the arithmetic average of the UPDRS scores assigned by the three neurologists to

each trial. The same three classification algorithms used for the G tasks and described in Section 2.5.3, namely NCC, $k$NN, and SVM, have been considered in the unified system. The chosen classifiers have different characteristics in terms of complexity and effectiveness and, thus, in our opinion they cover in an appropriate way the spectrum of classification algorithms available in the literature. The learning process has been validated against bias and overfitting through a leave-one-out cross-validation method is chosen. In particular, this means that each point of both the original and "PCA-projected" dataset is used, in turn, as a new (unknown) point to be classified, while the remaining samples are used to train the classifiers. The output of the classification procedure is an estimated UPDRS value, generally denoted as $\widehat{u}_M$, for every trial of each task. The system performance is evaluated considering the absolute[3] classification error $e_M$, defined as follows:

$$e_M \triangleq |\widehat{u}_M - u_M| \qquad u_M, \widehat{u}_M \in \{0, 0.5, 1, 1.5, 2, 2.5, 3, 3.5, 4\}$$

where $u_M$ is the value of $\text{UPDRS}_{\text{Mean}}$ for the considered trial.

Different configurations, in terms of features combinations and system parameters, have been considered and exhaustively tested in order to identify those which allow to achieve the best classification performance. For each task, the Cumulative Distribution Function (CDF) of the error $e_M$ is computed considering the results of the classification procedure obtained using, as inputs for the three classifiers (NCC, $k$NN, and SVM): (i) all the possible combinations of kinematic features with original data; (ii) increasing number of principal components (up to the number of features in the original dataset) when PCA-projected data are considered. Furthermore, when $k$NN is used as classification algorithm, values of $k$ between 1 and 10 are used. The Area under the Curve (AuC) of the CDF of $e_M$ is selected as a representative performance optimization metric, since maximizing this value corresponds to minimizing the overall absolute classification error. Among all the CDFs obtained for all considered parameters' combinations, those which maximize the AuC are selected to determine the system configuration which achieves the best classification performance.

[3]The absolute value of the classification error is considered because we are interested in quantifying the absolute deviation between automatically estimated and neurologist-assigned UPDRS scores.

## 3.5 Results

### 3.5.1 Kinematic Characterization

By analyzing the kinematic characteristics of gait in relation to the clinical assessment by neurologists, in Chapter 2 we have observed a strong connection between some of the extracted kinematic features and the UPDRS scores assigned to the G trials. In order to extend the investigation, in the following, the link between the most meaningful parameters for the characterization of the LA, S2S, and G tasks and the four UPDRS score sequences (namely, the three by the neurologists and the consensus score, $\text{UPDRS}_{\text{Mean}}$) is discussed.

In Figures 3.5, 3.6, and 3.7, the average values, over all trials belonging to each UPDRS class (from 0 to 4), of the most relevant features for the LA, S2S, and G tasks, respectively, are shown, through radar plots, considering the UPDRS scores given by the three neurologists and the $\text{UPDRS}_{\text{Mean}}$. Each parameter has been normalized and rescaled in order to assume a value between 0 and 1, where 0 represents the worst case and 1 the best case—best and worst are feature-specific. As expected, it can be observed that, beyond the inter-neurologist variability, in each task, the overall motor performance of the patients, in terms of its associated kinematic parameters, tends to worsen for increasing UPDRS scores. An intuitive way to interpret the overall motor ability of each group of patients in performing the specific task, by simply looking at the plots, consists in considering the area enclosed by the colored lines associated to UPDRS classes: the smaller the area, the worse the motor performance. It is easy, at this point, to observe how the UPDRS class 0 achieve the best performance in almost all the considered features and in every task, whereas the higher UPDRS classes (from 2.5 to 3.5) have significantly worse performances. In order to show how much every single feature is related to the UPDRS score, we compute the Pearson's correlation coefficient (denoted also as $r$-value) between the kinematic parameters and the $\text{UPDRS}_{\text{Mean}}$ values of each task. In the last column of Tables 3.4, 3.5, and 3.6, the $r$-values for all the most relevant features are shown, highlighting in bold those which have the highest correlation with the $\text{UPDRS}_{\text{Mean}}$ score of the considered task.

We note that correlations with the corresponding $p$-value[4] higher than 0.05 are considered as non significant (n.s.). Furthermore, the sign of the correlation coefficients makes it possible to discern if the value of the considered feature increases (positive sign) or decreases (negative sign) for increasing UPDRS score.

For the LA task, the average values per UPDRS class is obtained considering both RLA and LLA trials. Looking at Figure 3.5, it can be observed that the decreasing trend for increasing UPDRS score is evident in all the considered features. Values belonging to the extremes UPDRS classes (e.g., UPDRS scores equal to 0 or 3/3.5) are clearly separated from the others, while values associated with the intermediate UPDRS classes (e.g., UPDRS scores equal to 1, 1.5, or 2) tend to overlap, in some cases, in the same region of the plot. This behavior is consistent with clinical evaluations of PD patients, when distinguishing between intermediate levels of impairments may be difficult. Considering the correlations between LA features and UPDRS score, the parameter which has the highest (absolute) $r$-value is $\Omega_{\text{mean}}$.

Similarly to the LA case, in the S2S task, the performance degradation for increasing UPDRS score is evident, as shown in Figure 3.6. The parameters for which this trend is clearer are those related to the duration of the S2S single rising, namely: $T$, $T_F$, and $T_B$. As expected, these parameters achieve the highest correlation values with respect to the UPDRS score and are those that better characterize the S2S task.

The interpretation of the features associated the G task have been widely discussed in Section 2.5.2. We briefly recall the main observations. The general performance trend is decreasing with increasing UPDRS score, but with some exceptions: in Figure 3.7, for example, it can be observed that the "best" performance in some of the temporal features is achieved by the average values associated with UPDRS class 3. This is due to the fact that PD patients who present *festinating gait*, i.e., a gait pattern alteration typical of Parkinsonians, characterized by a quickening and shortening of normal strides, perform short steps with a very high cadence, thus leading to values in temporal parameters and cadence that may be interpreted as "good" even for

[4]We recall that the $p$-value represents the probability that the observed differences, in the sample data which are being tested, are due to random sampling errors and not to true differences between populations [106].

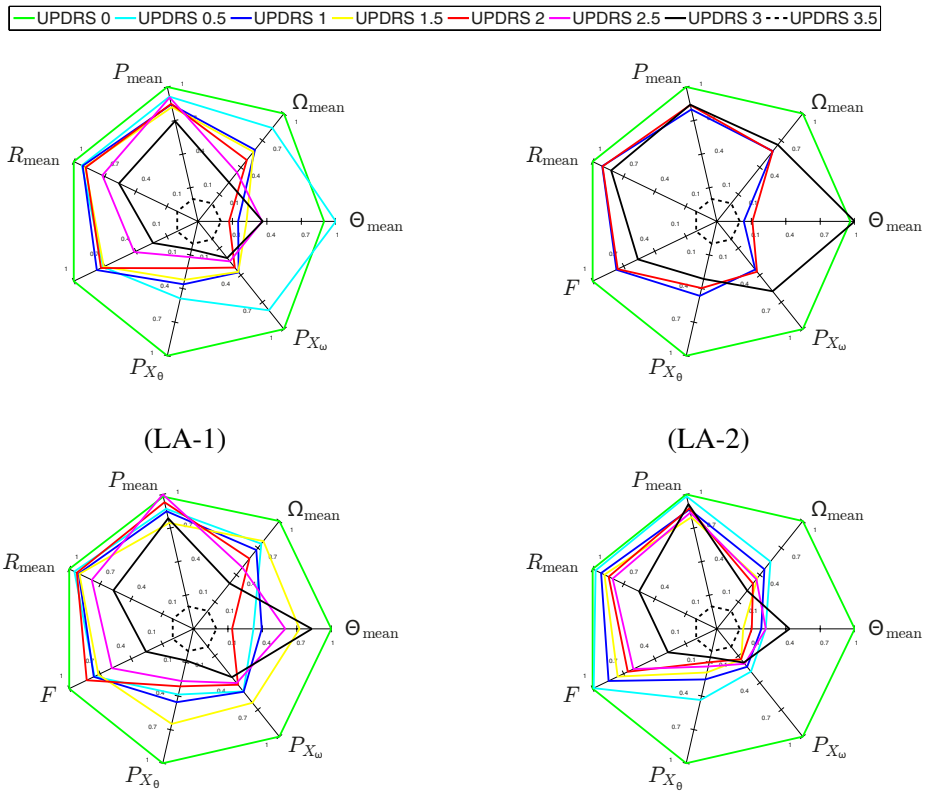


Figure 3.5: Radar plots of the average normalized features grouped by UPDRS class in the LA task considering the UPDRS scores by neurologist 1 (LA-1), neurologist 2 (LA-2), neurologist 3 (LA-3), and the $\text{UPDRS}_{\text{Mean}}$ (LA-M).

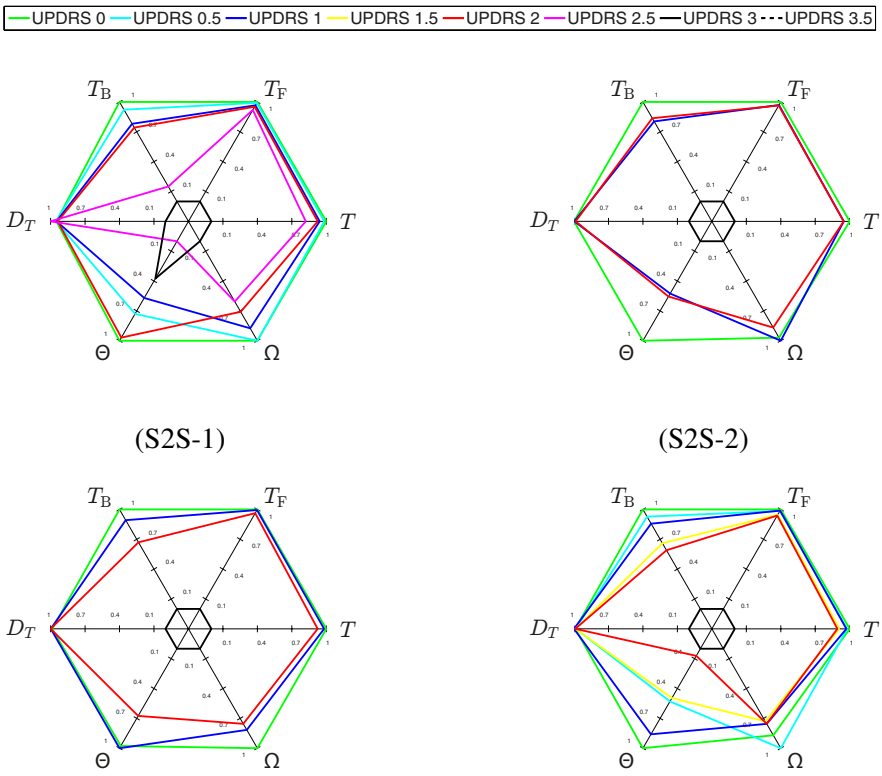


(S2S-1) (S2S-2)

(S2S-3) (S2S-M)

Figure 3.6: Radar plots of the average normalized features grouped by UPDRS class in the S2S task considering the UPDRS scores by neurologist 1 (S2S-1), neurologist 2 (S2S-2), neurologist 3 (S2S-3), and the $\text{UPDRS}_{\text{Mean}}$ (S2S-M).

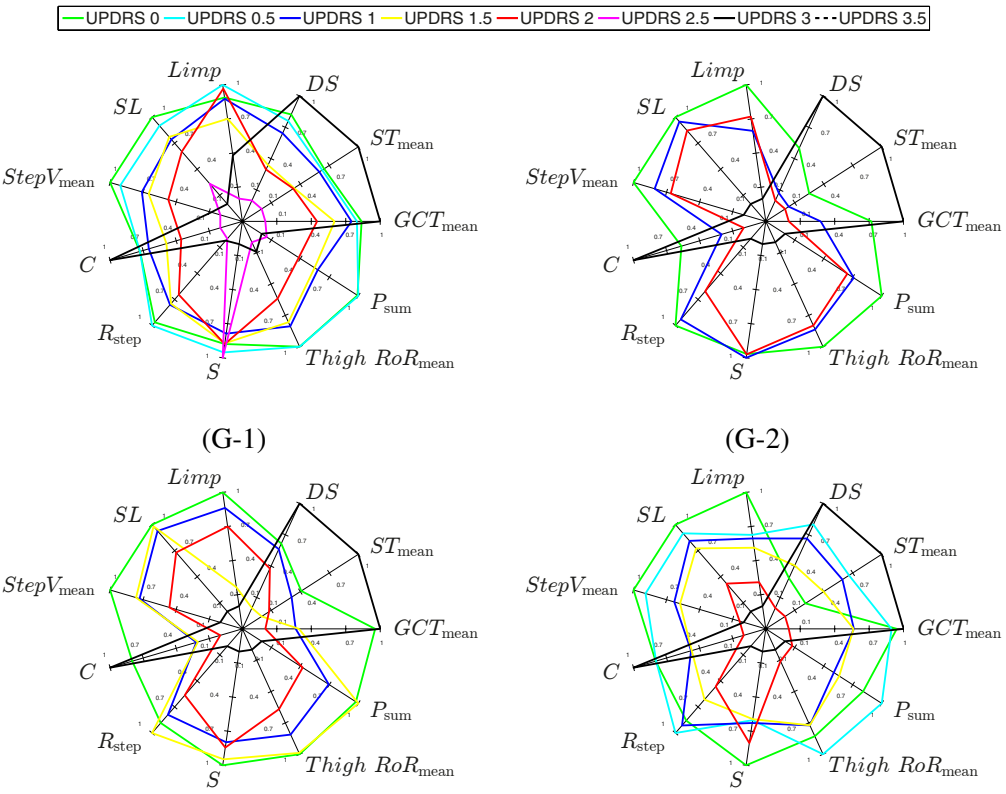


(G-1) (G-2)

(G-3) (G-M)

Figure 3.7: Radar plots of the average normalized features grouped by UPDRS class in the G task considering the UPDRS scores by neurologist 1 (G-1), neurologist 2 (G-2), neurologist 3 (G-3), and the $\text{UPDRS}_{\text{Mean}}$ (G-M).

high UPDRS scores. Spatial parameters, flexion/extension excursions of the thighs, and step regularity are those which show the clearest decreasing trends in function of UPDRS values. This consideration, besides being consistent with the clinical observations of parkinsonian walking, is also confirmed by the good correlation values (absolute values approximately equal to 0.6) between kinematic parameters, such as $SL$, $StepV_{\text{mean}}$, $R_{\text{step}}$, and $Thigh\ RoR_{\text{mean}}$, and the $\text{UPDRS}_{\text{Mean}}$ score of the G task. Finally, the feature $P_{\text{sum}}$, which is representative of the overall "power" associated with the patient's movements during gait, clearly decreases monotonically from UPDRS 0 to UPDRS 3, showing also a moderate correlation ($r$-value equal to -0.43) with the UPDRS score.

### 3.5.2 Automatic Detection

As anticipated in Section 3.4.4, an exhaustive testing of the automatic UPDRS scoring system has been carried out in order to find the parametric configuration which allows to achieve, for each task, the best classification performance, i.e., which maximizes the AuC of the CDF of the error $e_M$. The optimal system configuration, including the best classification algorithm and the best combination of features, is shown, for each task, in Table 3.7. The observed results show that in all tasks the best classifier is $k$NN, with $k$ set to 3 (LA and S2S) or 6 (G). Furthermore, it can be observed that the number of features associated with the best performance increases for increasing complexity of the task movement patterns. For completeness, we remark that the subset of features which allows to achieve the best performance in the G task is different to the one obtained in Section 2.5.3, even though the number of elements in the subset, the classifier, and its configuration ($k$ = 6) remained the same. This is due to the fact that, in the unified analysis, the number of trials considered for the extraction of the kinematic features and the training of the automatic system is different from the one used for analyzing the G task singularly, as explained in Section 3.3.4.

In Figure 3.8 (a), the CDFs corresponding to the optimized parametric configurations of the automatic UPDRS scoring system in each task are shown. The *accuracy* of the automatic system (corresponding to CDFs' values at $e = 0$) ranges from approximately 43% in the LA and S2S tasks to 62% in the G task. The percentage of

Table 3.7: Combination of parameters corresponding to the best performance of the automatic UPDRS scoring system for each task.

| Task | Classifier | Set of features |
|---|---|---|
| LA | $k$NN ($k = 3$) | $\{\Omega_{\text{mean}}, F\}$ |
| S2S | $k$NN ($k = 3$) | $T$ |
| G | $k$NN ($k = 6$) | $\{DS, R_{\text{step}}, Thigh\ RoR_{\text{mean}}\}$ |

trials classified with $e \leq 0.5$ is over 81% in all the considered tasks (LA: 83%; S2S: 81%; and G: 94%) while more than 94% of the samples are classified with $e \leq 1$ (LA: 97%; S2S: 94%; and G: 98%). Moreover, it can be observed that the classification error is never greater than 1.5.

For a more detailed characterization of the misclassification errors made by the automatic system, in Tables 3.8, 3.9, and 3.10, the confusion matrices associated with the automatic scoring of the LA, S2S, and G tasks, respectively, are shown. It can be observed that the automatic systems has the tendency to bias, in all cases, the estimated UPDRS scores around a dominant class, according to the Gaussian-like distribution of the $\text{UPDRS}_{\text{Mean}}$ score highlighted in Section 3.3.4 and shown in Figure 3.2. The UPDRS classes with a small number of samples are almost "ignored" by the classifier and the samples associated with them are labeled with a UPDRS value nearer to the dominant class, thus determining a general underestimation of actual UPDRS score. This behavior is a clear consequence of the non-homogeneity of the UPDRS evaluations of the various neurologists.

From the presented confusion matrices, other performance indexes, such as the *precision*, the *sensitivity*, and the *specificity*, can be calculated. In Table 3.11, the average values of these performance indexes across all the UPDRS classes are shown. From these results, one could conclude that the automatic system performs poorly and it is not able to provide a reliable estimation of the UPDRS score. However, we remark that the computed statistics take into account only the samples correctly classified ($e_M = 0$), which may be not the proper why to quantify the goodness of the system. By observing the CDF shown in Figure 3.8 (a), indeed, it can be noticed

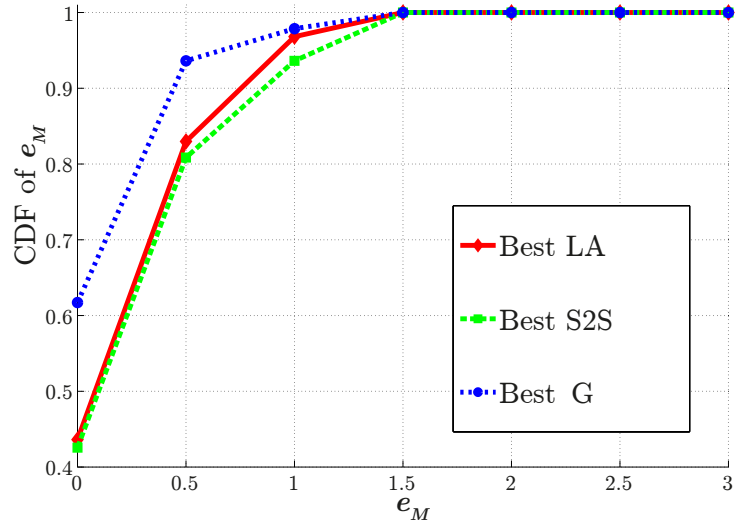


(a)

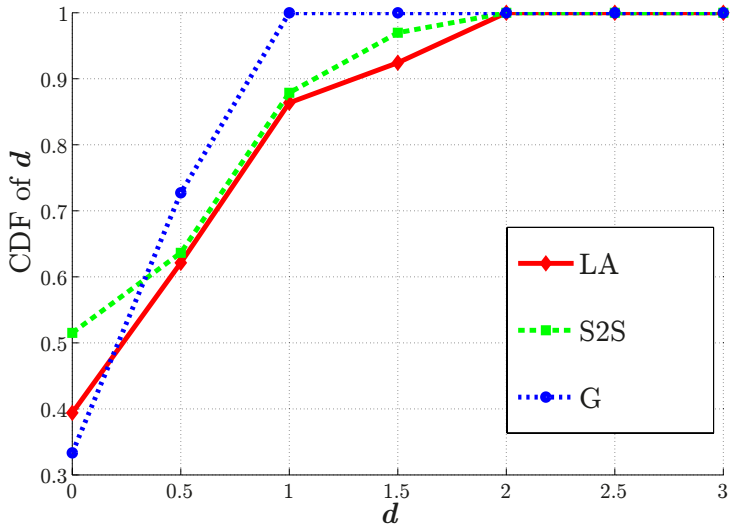


(b)

Figure 3.8: CDFs of (a) the automatic classification error $e_M$ for the best performance achieved in each task and (b) the (absolute) difference $d$ in the UPDRS scoring between neurologist 1 and 2.

Table 3.8: Confusion matrix for the LA task automatic UPDRS scoring procedure.

| | | Predicted score | | | | | | | |
|---|---|---|---|---|---|---|---|---|---|
| | [%] | **0** | **0.5** | **1** | **1.5** | **2** | **2.5** | **3** | **3.5** |
| Actual score | **0** | **0** | 50 | 50 | 0 | 0 | 0 | 0 | 0 |
| | **0.5** | 8 | **54** | 23 | 15 | 0 | 0 | 0 | 0 |
| | **1** | 0 | 23 | **18** | 53 | 6 | 0 | 0 | 0 |
| | **1.5** | 0 | 5 | 16 | **65** | 11 | 3 | 0 | 0 |
| | **2** | 0 | 17 | 0 | 58 | **25** | 0 | 0 | 0 |
| | **2.5** | 0 | 0 | 0 | 50 | 10 | **40** | 0 | 0 |
| | **3** | 0 | 0 | 0 | 50 | 0 | 50 | **0** | 0 |
| | **3.5** | 0 | 0 | 0 | 0 | 0 | 100 | 0 | **0** |

Table 3.9: Confusion matrix for the S2S task automatic UPDRS scoring procedure.

| | | Predicted score | | | | | | | |
|---|---|---|---|---|---|---|---|---|---|
| | [%] | **0** | **0.5** | **1** | **1.5** | **2** | **2.5** | **3** | **3.5** |
| Actual score | **0** | **100** | 0 | 0 | 0 | 0 | 0 | 0 | 0 |
| | **0.5** | 47 | **31** | 1 | 1 | 0 | 0 | 0 | 0 |
| | **1** | 40 | 40 | **20** | 0 | 0 | 0 | 0 | 0 |
| | **1.5** | 34 | 0 | 22 | **22** | 22 | 0 | 0 | 0 |
| | **2** | 34 | 0 | 0 | 66 | **0** | 0 | 0 | 0 |
| | **2.5** | - | - | - | - | - | **-** | - | - |
| | **3** | - | - | - | - | 100 | 0 | **0** | 0 |
| | **3.5** | - | - | - | - | - | - | - | **-** |

Table 3.10: Confusion matrix for the G task automatic UPDRS scoring procedure.

| | | Predicted score | | | | | | | |
|---|---|---|---|---|---|---|---|---|---|
| | [%] | **0** | **0.5** | **1** | **1.5** | **2** | **2.5** | **3** | **3.5** |
| Actual score | **0** | **0** | 0 | 100 | 0 | 0 | 0 | 0 | 0 |
| | **0.5** | 0 | **45** | 55 | 0 | 0 | 0 | 0 | 0 |
| | **1** | 0 | 0 | **78** | 22 | 0 | 0 | 0 | 0 |
| | **1.5** | 0 | 6 | 25 | **69** | 0 | 0 | 0 | 0 |
| | **2** | 0 | 0 | 0 | 100 | **0** | 0 | 0 | 0 |
| | **2.5** | - | - | - | - | - | **-** | - | - |
| | **3** | 0 | 0 | 0 | 100 | 0 | 0 | **0** | 0 |
| | **3.5** | - | - | - | - | - | - | - | **-** |

Table 3.11: Summary of the classification performance statistics (average values across all the UPDRS classes).

| Task | Accuracy | Precision | Sensitivity | Specificity |
|---|---|---|---|---|
| LA | 43.62% | 34.55% | 25.17% | 84.52% |
| S2S | 42.55% | 28.00% | 25.63% | 77.51% |
| G | 61.70% | 66.48% | 31.83% | 88.03% |

that the performance of the system improves significantly considering the samples classified with $e_M \leq 0.5$. In this case, the ability of the automatic system in estimating an adequate UPDRS score can be considered acceptable.

To explain the reasons behind this behavior, a comparative analysis between the performance achieved by the developed system and the inter-rater variability of the neurologists in the UPDRS task assessment has been carried out. In Figure 3.8 (b), the CDFs of the (absolute) difference $d$ between the UPDRS scores assigned by neurologists 1 and 2 in the three tasks are shown. The agreement in the evaluations ranges from 33% in the G task to 52% in the S2S task whereas the difference in the UPDRS scores between the two neurologists is lower than or equal to 1 in approximately 90% of the trials (100% for the G task). Similar results have been obtained from the comparison of the evaluations by neurologists 1 and 3 and by neurologists 2 and 3—the corresponding CDFs are not shown here. Comparing Figure 3.8 (a) and (b), it is possible to observe very similar trends in the CDFs of the estimation error $e_M$ and the difference of neurologists' evaluations $d$. It can thus be concluded that the variability in the UPDRS scoring between the automatic system and the neurologists seems to be comparable with the inter-rater variability between clinicians. In other words, the proposed automatic classification system is "accurate" enough to mimic the evaluation performance of medical personnel.

Obviously, a larger set of patients, a more uniform distribution of the patients in all the UPDRS classes, and additional evaluations by more neurologists would make the proposed system performance analysis more meaningful from a statistical perspective.

### 3.5.3 Correlations and $\text{UPDRS}_{\text{Total}}$

One of the key aspects of the proposed approach is the evaluation of multiple tasks relying on the same procedures for data acquisition, processing, and analysis. In our opinion, important insights on the validity of the proposed system and the contribution given by each task in the overall motor performance's assessment process can be derived by investigating the relationship between the considered tasks. For this reason, a comparative analysis of the correlations between the UPDRS evaluation carried out by doctors and the one performed by our automatic UPDRS scoring system is presented in the following.

A preliminary consideration of the relationship between the scores assigned to the different tasks can be made by looking at Figure 3.2: it can be easily observed that the distributions of UPDRS scores assigned by the neurologists and the $\text{UPDRS}_{\text{Mean}}$ score vary significantly from one task to another. This means that the motor performance achieved by a patient in one task is not necessarily related to those obtained in another task. In Figure 3.9, this observation is additionally investigated performing a comparison between the $\text{UPDRS}_{\text{Mean}}$ scores (cases from (a) to (f)) and the UPDRS values assigned by the automatic system (cases from (g) to (l)), considering pairs of tasks.[5] Each trial is labeled with a pair of UPDRS values, corresponding to the UPDRS scores assigned to it in the two considered tasks. In each subplot, the "clusters" of trials labeled with the same pair of UPDRS scores and, thus, overlapping on the same portion of the plane, are shown as black points, whose size is proportional to the number of trials belonging to the cluster. Moreover, the linear regression line, i.e., the best-fitting straight line obtained with the least squares method, is also shown in red. For all the considered pairs of tasks, an increasing trend in UPDRS scores for both tasks can be observed, although for each UPDRS value assigned to one task, several UPDRS values can be assigned to the other task.

In the "edge" case in which the relationship between the evaluation of motor performance in two different tasks is perfectly linear, the regression line would be on the diagonal or parallel to it. For some pairs of tasks, such as those shown in Figure 3.9

[5] For the LA task, comparisons with both RLA and LLA UPDRS scores are shown separately.

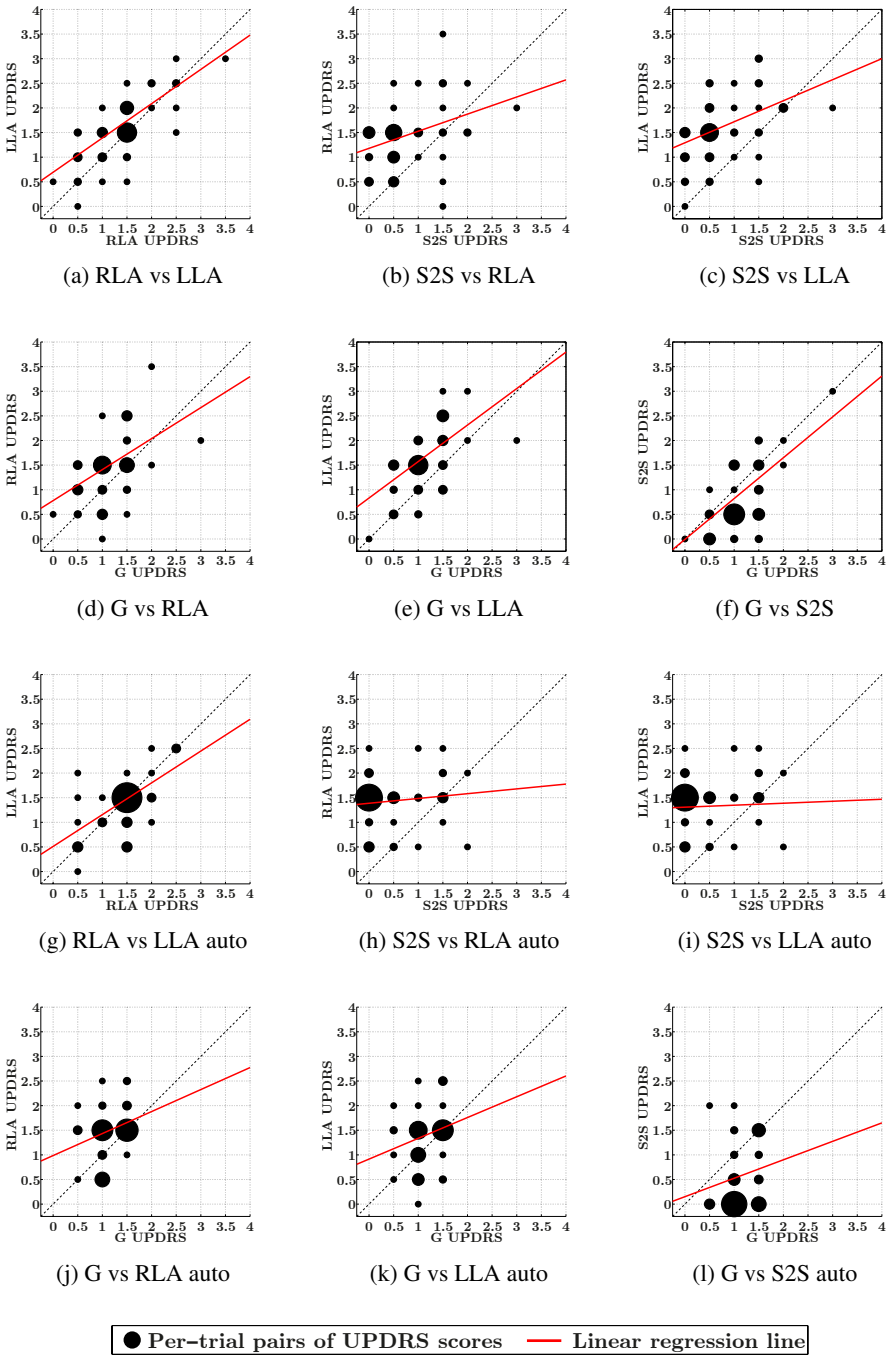


(a) RLA vs LLA (b) S2S vs RLA (c) S2S vs LLA

(d) G vs RLA (e) G vs LLA (f) G vs S2S

(g) RLA vs LLA auto (h) S2S vs RLA auto (i) S2S vs LLA auto

(j) G vs RLA auto (k) G vs LLA auto (l) G vs S2S auto

Figure 3.9: Comparison between UPDRS values assigned to each trial for different pairs of UPDRS tasks considering: in the upper half of the figure ((a), (b), (c), (d), (e) and (f)) the $\text{UPDRS}_{\text{Mean}}$ scores; in the lower half of the figure ((g), (h), (i), (j), (k) and (l)) the UPDRS values estimated through the automatic scoring system. Each point corresponds to a "cluster" of trials labeled with the same pair of UPDRS values and its size is proportional to the number of trials belonging to the same cluster.

(a), (d), (e), and (f), the linear relationship between the UPDRS scores is evident and, consequently, the regression line lies near the diagonal. In these cases, the values assigned in both tasks, in fact, are likely to be similar, indicating both comparable difficulties experimented by patients in the two tasks and a uniform metric used by the neurologists to assess them. In other cases, especially those including the S2S task, it can be observed that, while in one task (either LA or G) the trials are labeled with increasing UPDRS scores, in the S2S task the patient is still able to achieve a good performance and, consequently, the trials are labeled with a UPDRS equal to 0 or 0.5. This leads to an accumulation of points near the 0 and 0.5 UPDRS classes for the S2S task, which also influences the slope of the linear regression line, making it "flatter." Considering the automatically estimated UPDRS scores (cases from (g) to (l)), this behavior is even more evident: the linear relationship between tasks is always weaker than in the neurologist-assessed cases. This is due to the fact that the automatic scoring system, as anticipated in Subsection 3.5.2, tends to slightly underestimate the values of the UPDRS scores with respect to those assigned by doctors, increasing the concentration of the scores around the dominant UPDRS class of each task. In Figure 3.9 (h) and (i), for example, the slope of the regression line is almost horizontal, highlighting the un-correlation between the considered tasks. A high number of trial, indeed, are labeled with UPDRS scores equal to 1.5 and 0 in the LA and the S2S tasks, respectively. This reduction in the UPDRS scores range and the overlapping of the trials in certain regions of the plots contribute to making the dependence between the scoring of the pair of tasks less evident. Another factor which determines the degree of correlation between tasks is the accumulation of UPDRS score around the dominant class of each task. In Subsection 3.3.4, we have observed that the $\text{UPDRS}_{\text{Mean}}$ scores has a Gaussian distribution centered in 1.5, 0.5, and 1 for the LA, the S2S, and the G tasks, respectively. In Figure 3.9, it can be observed that the points with the largest size are always in correspondence of these UPDRS classes.

The considerations made by visually investigating pair of tasks in Figure 3.9, can be reinforced by analyzing numerically the correlation between the considered tasks. At this point, we also introduce an aggregate UPDRS score, denoted as $\text{UPDRS}_{\text{Total}}$, given by the sum of the $\text{UPDRS}_{\text{Mean}}$ scores assigned to the RLA, LLA, S2S, and G

tasks. The summation of the UPDRS scores assigned to different combinations of tasks [84, 102, 104], is a common practice used in the literature to predict the overall functional capabilities of PD patients. From our viewpoint, $\text{UPDRS}_{\text{Total}}$ is a concise parameter representing the overall level of motor impairments of a patient in the considered tasks. In Table 3.12, the correlations between the $\text{UPDRS}_{\text{Mean}}$ scores in the various tasks and between them and $\text{UPDRS}_{\text{Total}}$ are shown. As in Subsection 3.5.1, the Pearson's correlation coefficient (i.e., the $r$-value) is used, considering as significant only the parameters with associated $p$-value $\leq 0.05$. It can be observed that the correlation between the UPDRS scores of each task and the aggregate score is high (from 0.76 to 0.87), indicating that $\text{UPDRS}_{\text{Total}}$ significantly represents, in a concise way, the motor performance level measured by each task. The correlations between pairs of tasks, instead, range from 0.75 (between RLA and LLA, which are likely to be strongly correlated since they refer to the same exercise) to 0.37 between RLA and S2S—this is representative of the poor correlation between those tasks. The latter result is expected because, from a medical viewpoint, each UPDRS task aims to assess a specific PD symptom and the "performance" achieved by patients may vary consistently from one exercise to another [104, 107]. However, in some cases, such as in the comparison between S2S and G UPDRS scores, the $r$-value is still relevant because both tasks refer to the same "macro-group" of PD symptoms (in this case to the "Gait/Posture" group) and may share some characteristics [104].

In the same way, in Table 3.13, the correlation values (obtained by pair-wise comparisons of the UPDRS scores estimated with the automatic UPDRS scoring system in each task, and the associated $\text{UPDRS}_{\text{Total}}$) are presented. The obtained results still show relatively high $r$-values (although slightly lower the those of the neurologist-assessed cases) between tasks and the $\text{UPDRS}_{\text{Total}}$ score. Also the correlation between RLA and LLA remains high. For all the other pairs of tasks, instead, the correlations become non significant. This is due to the fact that, as observed in Figure 3.9 (h)-(l), the automatically estimated UPDRS scores are often underestimated and tend to overlap in correspondence to the dominant UPDRS class of each task, making the linear dependence between the UPDRS values in the pairs of tasks weaker.

For completeness, Table 3.14 shows the correlations between the neurologist-

Table 3.12: Correlations between $UPDRS_{Mean}$ scores.

| | Total | RLA | LLA | S2S | G |
|---|---|---|---|---|---|
| Total | 1.00 | | | | |
| RLA | 0.82 | 1.00 | | | |
| LLA | 0.87 | 0.75 | 1.00 | | |
| S2S | 0.76 | 0.37 | 0.46 | 1.00 | |
| G | 0.82 | 0.51 | 0.60 | 0.66 | 1.00 |

Table 3.13: Correlations between UPDRS scores assigned by the automatic UPDRS scoring system.

| | Total | RLA | LLA | S2S | G |
|---|---|---|---|---|---|
| Total | 1.00 | | | | |
| RLA | 0.77 | 1.00 | | | |
| LLA | 0.74 | 0.63 | 1.00 | | |
| S2S | 0.58 | n.s. | n.s. | 1.00 | |
| G | 0.54 | 0.29 | n.s. | n.s. | 1.00 |

Table 3.14: Correlations between $UPDRS_{Mean}$ scores and automatically estimated UPDRS scores.

| Total | RLA | LLA | S2S | G |
|---|---|---|---|---|
| 0.79 | 0.74 | 0.54 | 0.55 | 0.60 |

assigned and the automatically assigned UPDRS scores. In $UPDRS_{Total}$ and RLA cases, the correlation is high (0.79 and 0.74 respectively) while in the LLA, S2S, and G tasks lower values are observed (0.54, 0.55, and 0.60, respectively), indicating a higher sensitivity to classification errors.

Finally, the $UPDRS_{Total}$ values, calculated considering both (a) the $UPDRS_{Mean}$ and (b) the trials' scoring by the automatic system, are visualized through barplots in Figure 3.10. Each bar represents the $UPDRS_{Total}$, with the contributions of the score assigned to the single tasks highlighted with different colors, calculated for each trial. The values are ordered in ascending order to highlight the data trend for increasing values of $UPDRS_{Total}$. The (red) exponential curves, obtained by minimum mean square error fitting, represent smoothed versions of the aggregate scores' trends. By looking at the plots, to main observations can be made: (i) as mentioned above,

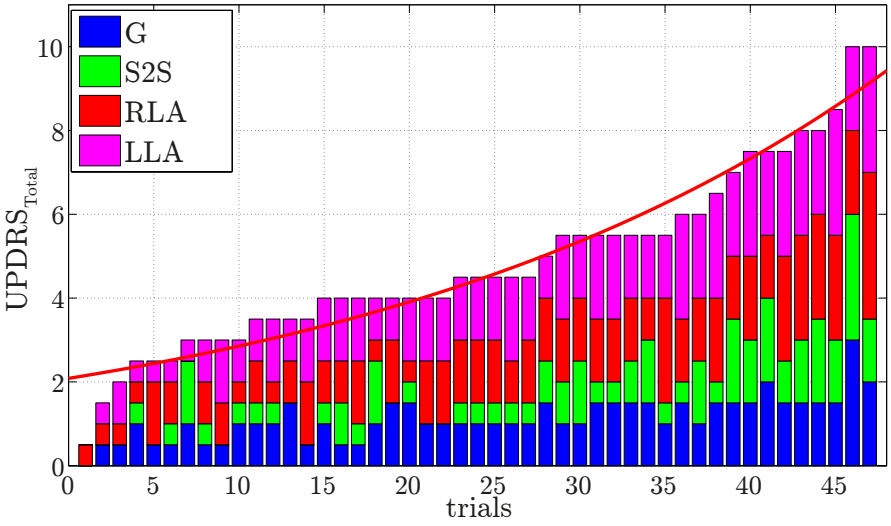


(a)

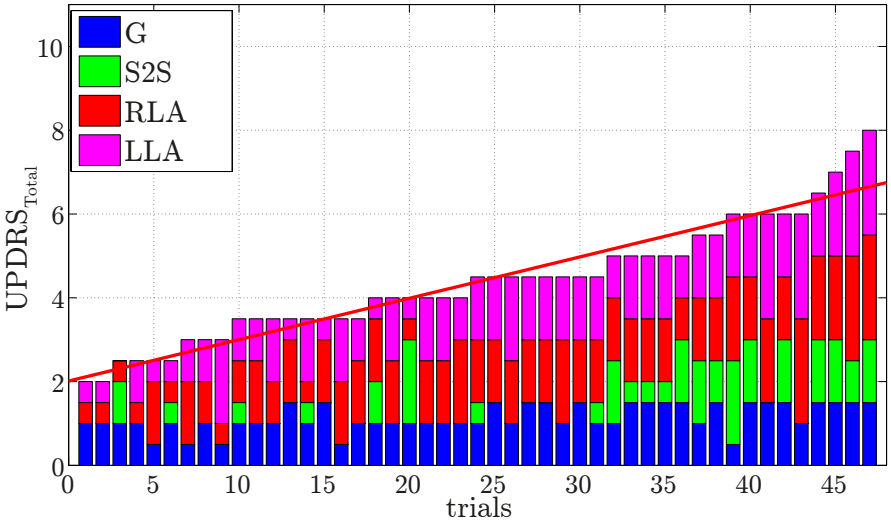


(b)

Figure 3.10: Bar plots representing the values of UPDRS$_{Total}$ for all the trials considering (a) the associated UPDRS$_{Mean}$ scores and (b) the UPDRS values assigned by the automatic scoring system. Contributes by each task are shown with different colors.

also in this case is possible to notice that the automatic classification system tends to assign UPDRS scores in accordance to the dominant UPDRS class of each task. This behavior leads to generally lower values of $\text{UPDRS}_{\text{Total}}$ and to a more reduced variability in the aggregate score for the automatic system, which is also emphasized by a lower slope of exponential fitting curve in Figure 3.10 (b). (ii) the contribution given by the S2S scores to $\text{UPDRS}_{\text{Total}}$ is almost negligible (between 0 and 0.5 in 90% of the trials) for aggregate scores lower than 5, especially when the automatic system is used.

These experimental observations confirm the effectiveness of the LA and G tasks in representing the progression of motor impairments in PD patients and also highlight the "non-challenging" nature of the S2S task for patients with mild symptoms. Nevertheless, the UPDRS score assigned to the S2S task becomes very important to distinguish between Parkinsonians with moderate and severe motor complications, when the $\text{UPDRS}_{\text{Total}}$ is used as evaluation metric.

## 3.6 Applications

### 3.6.1 A Tele-medicine System for the Remote Monitoring of PD Patients

The characteristics of the designed system make it suitable for real applications in the e-health scenario, such as tele-medicine systems for remote monitoring of PD. The objective recording of motor fluctuations in a home environment throughout the day, unlike a time-limited and "randomly-timed" clinical evaluation in an out-patient environment, could provide more reliable information to neurologists and allow a more accurate assessment and management of the symptoms.

For example, considering a typical scenario in the L-DOPA therapy management of PD patients, in which the drug is split in 4 or 5 doses, timed according on the evidence of the motor diary filled out by the patient (which often lacks reliability), it can be easily understood how the opportunity to highlight an accurate daily profile of motor fluctuations could help the neurologists to define a personalized timing and dosing of medical treatment, thus improving the therapy effectiveness. Moreover, patients would feel more comfortable and motivated to do their exercises in a familiar

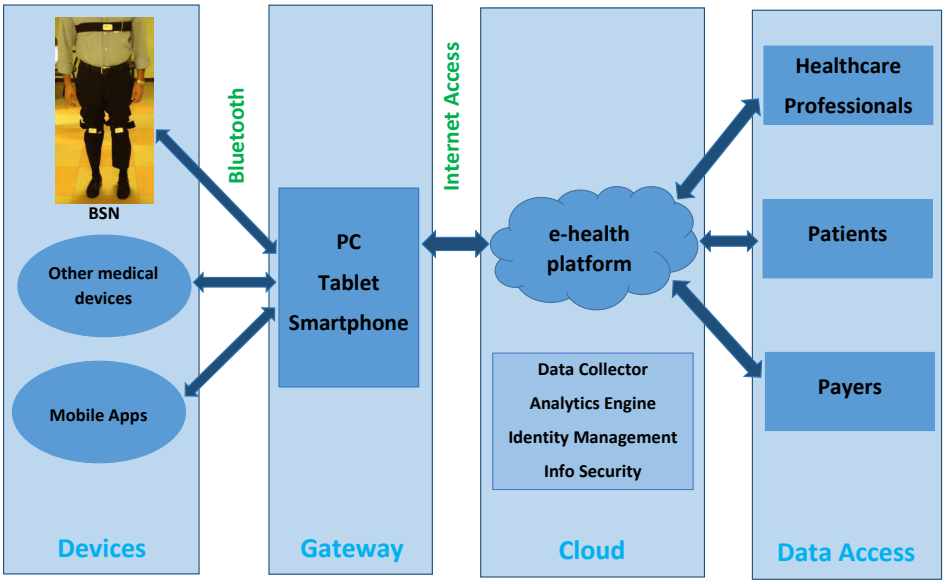


Figure 3.11: General architecture of a cloud-based e-health platform.

environment, saving time and money by avoiding to go to an ambulatory for each visit. Doctors, on the other hand, could reach a larger number of subjects, who, otherwise, could not be followed continuously from movement disorder specialists and rely on a more accurate and up-to-date clinical picture of patients.

A general and simplified architecture for a cloud-based e-health platform is shown in Figure 3.11. Four main levels can be defined to describe the functionalities of the platform. The *device* level includes all the devices used as sensing technology, such as sensors for analyzing the movements, measuring blood pressure or glucose level, electrocardiographs, electromyographs, etc., or as tool for retrieving useful information about the patients' medical condition (e.g., a mobile app used as electronic diary by patients). The data measured by the sensing devices are then sent through Personal Area Network (PAN) protocols, such as Bluetooth, to the *gateway* level, where the information is collected ad processed using more powerful devices, such as personal

computers, tablets or smartphones, connected to the Internet. At this point, the processed data are forwarded through the web to the cloud-based core of the e-health platform, identified by the *cloud* level, where the most relevant operations, such as those related to information storage, data analysis, identity management, and security, take place. Finally, in the *data access* level, all the possible users of the system, which can be the patients and their relatives, the medical professionals, the system administrators, the health-care payers, etc., are allowed to access and visualize, with proper permission policies, the information they need. Since the e-health systems market is quite fragmented and poorly standardized, the best strategy for a practical implementation of the proposed PD monitoring application could be to integrate it into an existing e-health platform [108, 109], exploiting the APIs provided by the platform. The integration could be done, for example, at the *gateway* level, by adding a proper software component for the analysis of the data recorded by the IMU-based BSN. The processed data could then be managed according to the platform requirements, in the same way as the other data collected by the platform.

### 3.6.2 Efficient Implementation

So far, we have designed and tested our system in order to investigate its feasibility and performance, without considering constraints in terms of computational power or time consumption. In a real application scenario, as the one discussed in Section 3.6.1, the system would be subject to several limitations. An efficient design and implementation would be thus required in order to reduce the complexity and, consequently, the required computational resources, while still retaining the ability to achieve good (although not optimal) performance. To this end, the performance variations between the optimal system configuration and other "suboptimal," but simpler, alternatives are now discussed.

In Table 3.15, the performance reductions (in percentage), obtained by comparing the AuC of the CDF of the error $e_M$ associated with the best parametric configuration with the AuCs of "suboptimal" alternatives, are shown. The best configurations obtained for the three tasks, previously shown in Table 3.7, are denoted in Table 3.15 as Best LA (AuC equal to 92.29%), Best S2S (AuC equal to 90.96%), and Best G

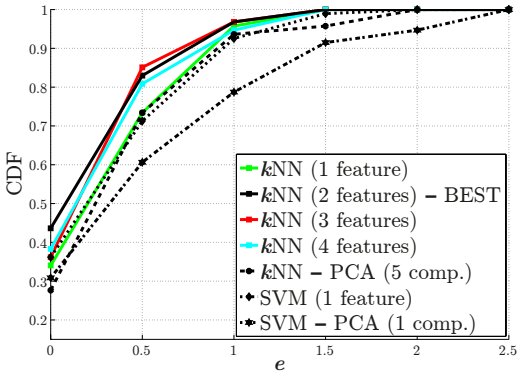


(a)

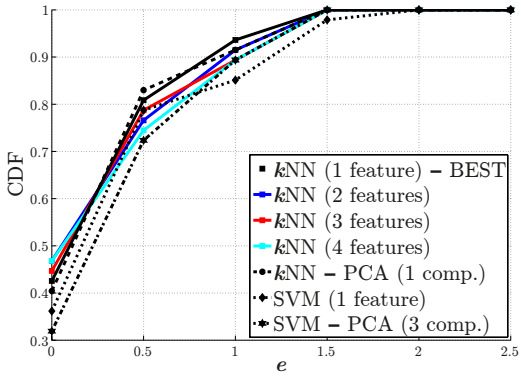


(b)

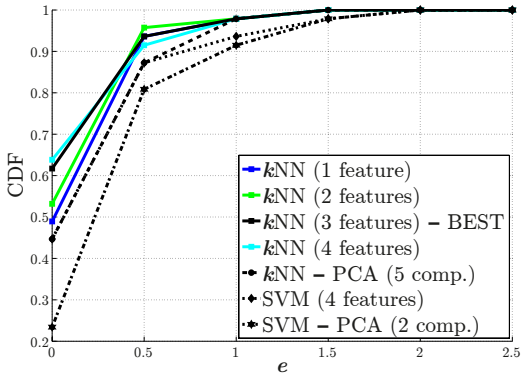


(c)

Figure 3.12: CDFs associated with different system configurations in the (a) LA, (b) S2S, and (c) G tasks. The best CDF is represented with a solid black line.

Table 3.15: Reductions in the AuC of the CDF of $e_M$ comparing the various parametric configurations with the optimal one.

| Number of features or principal comp. | Method | | | |
|---|---|---|---|---|
| | $k$NN | $k$NN-PCA | SVM | SVM-PCA |
| | | **LA** | | |
| 1 | -2.79 % | -5.20 % | -3.76 % | -10.99 % |
| 2 | **Best LA** | -5.01 % | -5.31 % | -11.57 % |
| 3 | -0.29 % | -7.23 % | -4.82 % | -12.72 % |
| 4 | -1.25 % | -5.49 % | -5.59 % | -14.27 % |
| 5 | -1.15 % | -4.53 % | -6.07 % | -14.94 % |
| | | **S2S** | | |
| 1 | **Best S2S** | -0.19 % | -2.92 % | -3.50 % |
| 2 | -0.77 % | -2.92 % | -4.28 % | -4.48 % |
| 3 | -0.97 % | -1.94 % | -2.92 % | -3.31 % |
| 4 | -1.55 % | -1.55 % | -3.11 % | -5.84 % |
| 5 | -1.36 % | -1.55 % | -4.67 % | -3.70 % |
| | | **G** | | |
| 1 | -1.11 % | -4.46 % | -6.69 % | -8.36 % |
| 2 | -0.37 % | -4.08 % | -5.20 % | -7.06 % |
| 3 | **Best G** | -4.83 % | -4.27 % | -9.47 % |
| 4 | -0.19 % | -3.71 % | -3.71 % | -7.80 % |
| 5 | -0.37 % | -4.27% | -4.08 % | -8.00 % |

(AuC equal to 95.39%) and highlighted in bold. Moreover, in Figure 3.12, the CDFs associated with the $k$NN algorithm applied to an increasing number of features (from 1 to 4) of the original data and the best configurations obtained using (i) $k$NN and PCA, (ii) SVM on the original dataset, and (iii) SVM on the "PCA-projected" data, are shown to provide a visual counterpart of the data presented in Table 3.15. As shown in Section 3.5.2, it can be observed that the best classification algorithm is the $k$NN in all the considered tasks. This kind of classifier does not require an explicit training phase, as it keeps all the dataset points (true neurologist-based scores) to take decisions in the "online" phase. This so-called "lazy learning" approach, how-

ever, implies high memory consumption and computational power to check all the training set elements for each classification round. On the other hand, the SVM algorithm achieves performance similar to (actually, slightly worse than) the one of the *k*NN method but with a more efficient learning procedure. In fact, SVM, after a more complex training phase, builds a compact classification model which can be used to easily identify the class of the test data, by simply checking in which partition of the features space the unlabeled sample lies. The relative reduction (in percentage), considering the best configuration in the SVM case for all the three tasks, is very limited, ranging from 2.92 % (S2S task) to 3.76 % (LA task).

Another possible strategy to lower the complexity of the automatic classification procedure is to reduce the dimensionality of the features dataset used as input for the classifiers. Looking at Table 3.15, it can be observed that the performance reduction, considering only one or two features (original data) for the *k*NN algorithm, is almost always below 2.80 %. In the SVM case as well, the performance degradation, with respect to the best SVM case, using only one feature is minimal. Dimensionality reduction in the presence of PCA tends to worsen the overall performance with both *k*NN and SVM methods. From these considerations, it can be concluded that, although the best classification performance is achieved by the *k*NN algorithm, the SVM classifier, applied to features of the original dataset, could be a more attractive choice for real-world applications, because of (i) higher efficiency (in terms of computational resources consumption) and (ii) minimal classification accuracy reduction with respect to *k*NN.

## 3.7 Conclusion

We have proposed an innovative approach for kinematic characterization of the LA, S2S, and G tasks through the same BSN with three nodes, together with automatic UPDRS assessment of the trials carried out by PD patients.

The results obtained in Subsection 3.5.1 indicate clearly that, in each task, some of the extracted kinematic features are strongly related to the UPDRS scores. The parameters which have turned out to be the most significant are the angular speed of

execution ($\Omega$) for the LA task, the total duration ($T$) for the S2S task, and the stride length ($SL$) for the G task. Moreover, an evident decreasing in the overall motor performance for patients belonging to different UPDRS classes has been highlighted, considering both the evaluations by multiple neurologists and the $\text{UPDRS}_{\text{Mean}}$ score. These findings are consistent with the observations made by the doctors in clinical environments.

Regarding the automatic UPDRS scoring system, the results presented in Subsection 3.5.2 have highlighted that the best classification performance is achieved using $k$NN as the classifier on the selected kinematic features, using an increasing number of features and increasing values of $k$ for increasing complexity of the tasks. The accuracy of the system ranges from 43% (in the LA and S2S tasks) to 62% (in the G task) but the classification error is lower than or equal to 1 in more than 94% of the cases. The comparison between the evaluation error of the automatic system and the inter-rater variability of the neurologists has shown similar performance trends, allowing us to consider the accuracy of the proposed UPDRS scoring system acceptable. Nevertheless, the automatic system tends to underestimate the actual UPDRS scores and to concentrate the predicted UPDRS values in correspondence to dominant UPDRS classes. This is not an intrinsic limitation of the proposed approach. In fact, it could be overcome by considering a statistically more significant dataset (i.e., a larger set of patients, with a more homogeneous distribution across all UPDRS classes). In addition, increasing the number of neurologists involved in the evaluation could reduce the bias in the assessment of UPDRS motor tasks.

In Subsection 3.5.3, the comparative analysis of the correlations suggests that the motor performance of PD patients may vary consistently between different tasks and, thus, the associated correlations may range from low (0.37, poor correlation) to high (0.75, good correlation) values. The correlation between UPDRS scores in distinct tasks becomes weaker (almost always negligible) when the automatic system is considered. This is another consequence of the fact that the automatic system tends to bias the evaluation around the dominant UPDRS classes. However, this result complies with findings in the medical literature [104], according to which the correlation between different tasks is likely to be poor or moderate because each task has been

defined with the aim to evaluate a specific aspect or symptom of the PD.

The obtained results have shown a good correlation between $UPDRS_{Total}$ and all the UPDRS scores of all the tasks (slightly lower correlations for the automatically-assessed tasks). This concise index can provide neurologists useful information about the overall condition and the functional capabilities of patients, integrating the evaluations made considering the single UPDRS scores in each task. The contribution of the S2S task in the aggregate score, for example, seems to be significant to distinguish patients with slight and mild symptoms from those who manifest moderate or severe impairments. This observation can be related to the characteristics of the movement typical of the S2S task, which involves the simultaneous activation of several control mechanisms (visual, posture, and balance) and worsens with the progress of the disease. .

Finally, the integration of the proposed system in a real cloud-based e-health platform for the development of a tele-medicine application for continuous monitoring of PD patients has been discussed, with focus on a possible system architecture and possible strategies for an efficient implementation of the proposed functionalities.

### 3.7.1 Future Work

Although the results obtained by the proposed system seem to be promising, further investigations are needed to overcome its current limitations. In particular, the implemented automatic UPDRS scoring system can be improved by considering a larger and, thus, statistically more relevant dataset, together with clinical evaluations of additional neurologists. Moreover, new UPDRS tasks may be considered and integrated in the automatic characterization and evaluation process. Using the same BSN and the same processing approach, indeed, tasks such as the Toe-tapping (UPDRS item 3.7), Freezing of Gait (UPDRS item 3.11), Postural Stability (UPDRS item 3.12), and Posture (UPDRS item 3.13), may be included in the analysis, providing a complete tool for the assessment of all the UPDRS item related to posture and lower limbs motor performance. A complete system, able to evaluate also the tasks associated to the upper limbs movements, would require additional sensors to be placed on the arms or the wrists. In any case, also in the current configuration, another interesting research

direction consists in investigating the patterns in motor fluctuations, i.e., the variation in the severity of the motor symptoms, across the whole day and for prolonged time period, in order to build an accurate model of the actual patient's situation.

# Chapter 4

# Quantitative Evaluation of Gait in Post-stroke patients

*The only thing I know is this:*
*I am full of wounds and still standing on my feet.*

– Nikos Kazantzakis

The analysis carried out of PD has shown the potential of BSN-based systems for the charactezation of functional motor tasks. Gait is undoubtly the most representative activity for evaluating the general level of motor impairment under several aspects. In post-Stroke patients, the analysis of the walking patterns is a key tool, for both the assessment and the rehabilitation processes. In this chapter, two BSN-based approaches, with different level of complexity and details, for the GA in post-stroke insividuals are presented. As the works described in the previous chapters, also this study is conducted within the *VRehab* project.

## 4.1 Introduction

### 4.1.1 Stroke

Stroke occurs when the supply of blood to the brain is either interrupted or reduced. When this happens, the brain does not get enough oxygen or nutrients which causes brain cells to die. Strokes can be classified into two major categories: ischemic and hemorrhagic. Ischemic strokes are the most common (around the 85% of the cases) and are caused by blockages or narrowing of the arteries that provide blood to the brain, causing severely reduced blood flow (i.e., ischemia). These blockages are often caused by blood clots, which can form either in the arteries connecting to the brain, or in other blood vessels before being swept through the bloodstream and into narrower arteries within the brain. Hemorrhagic strokes occur when a blood vessel in the brain leaks or ruptures. The blood loss deprives brain cells of blood and can damage them by increasing the pressure within the brain or the space between the brain and the skull. The ruptures can be caused by conditions such as hypertension, trauma, blood-thinning medications and aneurysms (i.e., weaknesses in blood vessel walls). If the flow of blood to the brain is only briefly interrupted, the stroke is defined as Transient Ischemic Attack (TIA).

Stroke is the third cause of mortality worldwide, with almost 6.7 millions of deaths in 2012 [110] and the leading cause of adult long-term disabilities. Depending on which region of the brain is damaged, complications may include:

- Hemiparesis: it is a unilateral paresis or weakness of the entire left or right side of the body. In its most severe form, i.e., when the paralysis of half of the body is complete, it is defined as Hemiplegia;
- Difficulty talking or swallowing: damages in the cerebral cortex and the lost of control of mouth and throat muscles can result in difficulties in talking clearly (dysarthria), swallowing/eating (dysphagia), or using and interpreting oral and written language (aphasia);
- Memory, thinking, and emotional difficulties: stroke survivors can experiment memory deficits, disorganized thinking, confusion, depression and problems in

controlling their emotions;

- Altered or painful sensations: pain, numbness, iper-sensitivity, altered or reduced sensory perception may also appear after a stoke event;

- Changes in behavior and self-care ability: people who have had strokes may become more withdrawn and less social or more impulsive and may need help in many of their daily activities, losing their independence.

Worldwide, stroke consumes about 2-4% of total health-care costs, and in industrialized countries stroke accounts for more than 4% of direct health-care costs [111]. Approximately one third of stroke survivors will have permanent physical impairments and will require high level of assistance in their every-day life [112]. For this reason, suddenly after the emergency treatment, the rehabilitation process should begin.

Immediate rehabilitation after a stroke event has a key role in helping patients to recover their functional capabilities and independence. Stroke rehabilitation is a combined and coordinated use of medical, social, educational, and vocational measures to retrain a person who has suffered a stroke to his/her maximal physical, psychological, social, and vocational potential, consistent with physiologic and environmental limitations [113]. The rehabilitation process often include different activities, such as speech therapy and occupational therapies, supporting groups (for helping both patients and their family to overcome the practical and emotional difficulties), and physical therapy. The latter aims at improving patient's independent mobility and focus on enhancing the ability to use the affected side limbs and the overall motor functionalities. In particular, regaining the ability to walk, at least in the domestic environment, is one of the main goals of both post-stroke patients and clinicians [114]. The objective evaluation of the recovery progression is crucial in order to assess the effectiveness of physical rehabilitation therapies, from the early days after the stoke occurs, at the hospital, and even more after several months, in patients' free-living environments.

### 4.1.2 Chapter Contribution

The usefulness of the quantitative analysis of gait, as a tool for providing meaningful information to clinicians, has been extensively discussed in general and for the specific case of PD, in Section 1.3.2 and Chapter 2, respectively. We pointed also out that IMU-based GA is currently the most adopted alternative approach to classical GA systems, because it is cost-effective, reliable, and easy-to-use.

Starting from these premises, in this chapter, a system for quantitative GA in post-stroke patients, based on the use of two different BSN configurations, is presented. In particular, we first describe a preliminary system relying on a multi-sensor BSN for a complete but not practical evaluation of walking patterns. Then, we focus on a novel, single IMU-based approach for an efficient, simple, flexible but also accurate characterization of both normal and hemiparetic gait [5]. The implemented single-sensor system allows us to extract a complete set of temporal features by a robust step detection method and an accurate stride segmentation procedure. Moreover, a revised version of two well-known methods for spatial parameters estimation is proposed. In both cases, we introduce dynamic calibration constants in order to reduce the estimation errors due to step asymmetry and inter-subject variability.

## 4.2 Related Work

The use of inertial sensing as mo-cap technology for monitoring and assessing the physical rehabilitation process in post-stroke patients is widespread in both medical and engineering literature. Different works have focused their attention on the evaluation, through wearable IMUs, of upper limbs movements [115, 116, 117, 118], postural adjustments [119], and general motor functionalities using standardized rating scales [43]. For what concerns GA, optoelectronic [120, 121, 122] systems, low-cost insole sensors for measuring GRF [123, 124, 125, 126], mobility assistive devices [127], manual investigation of videotaped walking sessions [128], and even smartphones [129] have been used for extracting different sets of parameters for characterizing gait patterns under various points of view. As for the PD case, discussed in Section 2.2, several approaches have appeared, in recent years, relying on IMU-

based BSNs for analyzing gait in post-stroke patients. For example, Fang et al. used two IMUs attached to the subject's thigh and shank (on the paretic side) to extract a reduced set of features, such as step length, hip and knee angles, and the gait regularity based on the autocorrelation of the accelerometric signals [130]. In [131], Mizuike and colleagues investigated the relationship between patients' motor recovery level and a specific set of raw walking features, such the normalized Root Mean Square (RMS), as a measure of gait smoothness, and the autocorrelation as a measure of stride similarity and regularity, associated to accelerometric signals measured using a tri-axial accelerometer mounted on the belt. Yang et al. developed a system based on two gyroscopes placed on the shanks for assessing post-stroke gait in terms of walking speed and temporal gait symmetry [132]. Their algorithm performed well when the angular velocities measured during hemiparetic patients walking were similar to those of the healthy subjects but it failed in the cases in which the gait patterns were too different. Finally, in [133], two accelerometers on the ankles were used to extract gait features, such as stride length, cadence, (right and left) entropy, swing to stride ratio (SSR), and normal/hemiparetic side symmetry. These parameters were monitored across all the rehabilitation process, from the moment patients were first admitted to the hospital until discharge, in order to show their recovery progression.

The methods proposed so far in the literature provide limited sets of spatio-temporal parameters (with respect to those returned by classical GA systems) or are able to compute high level information about the regularity and symmetry of gait. However, most of the inertial sensor-based algorithms for general or disease-specific GA are designed to assess symmetric gait and are not suitable for the evaluation of hemiparetic gait (typical of post-stroke patients), which is characterized by asymmetric and irregular walking patterns. For these reasons, the system proposed in the following aims at quantitatively characterizing gait through a complete and accurate set of parameters, taking into account and trying to overcome the limitations related to the typical aspects of hemiparetic gait (i.e., step asymmetry and inter-subject variability).


Figure 4.1: The multi-sensor BSN formed by 6 Shimmer 3 IMUs.

## 4.3 Multi-sensor System

In a preliminary evaluation phase, a multi-sensor BSN has been considered with the goal of providing a full and detailed characterization of gait. Having the possibility to rely on several (6) sensing nodes, the system can estimate a wide set of spatio-temporal and kinematic parameters, in both healthy and impaired gait.

### 4.3.1 Experimental Set-up

The BSN configuration adopted in the multi-sensor version of the system is shown Figure 4.1. Each sensing node is a Shimmer 3 equipped with accelerometer, gyroscope, and magnetometer, all tri-axial (for details about the Shimmer 3 platform refer to Section 1.2.5). The IMUs are attached to the subject's body with Velcro straps, trying to align their $x$ axis, the $y$ axis, and the $z$ axis with the right-left, upward-downward, and forward-backward directions, respectively. In particular, the nodes are placed in the following positions: one on the chest (1), one on the dominant/affected side thigh (2), two on the shanks (3 and 4), two on the feet (5 and 6).

The BSN sensors are synchronized and connected through Bluetooth to a PC,

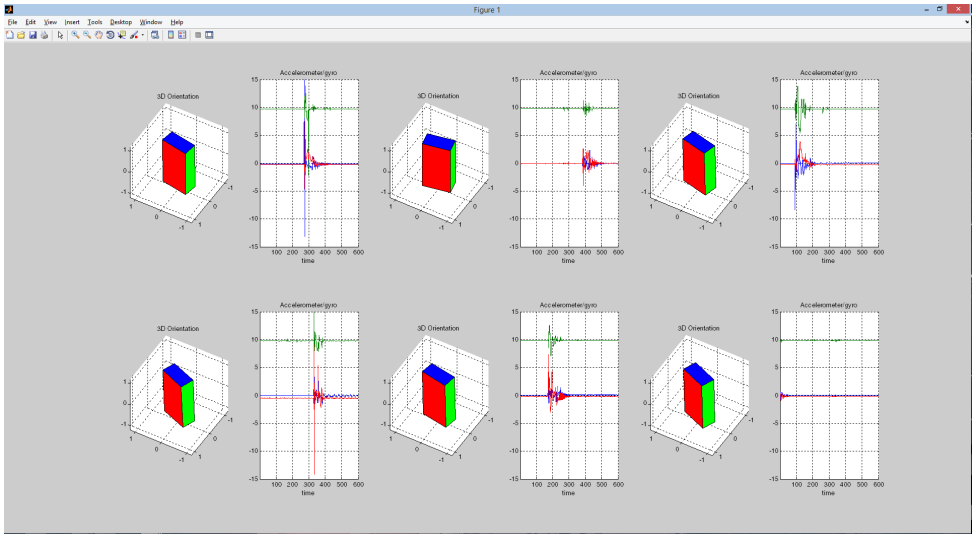


Figure 4.2: Screenshot of the acquisition software GUI implemented in MATLAB.

on which a specific software, developed using the MATLAB framework, collects and elaborates the streamed data. A screenshot of the acquisition software GUI is shown in Figure 4.2. It can be noticed that, beside the raw data from the IMUs, the 3-dimensional orientation of each node is also computed using the Magdwick algorithm [27].

### 4.3.2 Gait Characterization

After the acquisition procedure, the collected signals are processed and different parameters for the characterization of gait are computed. The first step of the feature extraction routine consists in segmenting gait in its fundamental phases by detecting the $HS$ and $TO$ instants for each leg. Three distinct algorithms have been implemented to this end: (i) the same method based on trunk accelerometry described in Chapter 2 for GA in PD patients; (ii) the algorithm proposed by Sabatini et al. in [61], which relies on gyroscope signals recorded with the sensors on the feet; (iii) the method based on the shanks' angular rate described by Aminian et al. in [59]. The latter has been selected in the final prototype due to its simplicity, reliability, and accuracy. Similarly,

for the estimation of the spatial parameters, various well-known algorithms, based on different combinations of sensors have been implemented and tested. We selected the method proposed in [55] (used also for step lengths computation in the system for GA in PD patients, as described in Section 2.4.1). Finally, the inclination in the sagittal, transverse, and frontal planes of the body segments on which the sensing nodes are positions has been calculated.

### 4.3.3 Results

Due to the preliminary nature of the prototype, we only conducted tests on control subjects and with limited ground truth references (video recording of the sessions and measurement of the traveled distance). In any case, the comparison between temporal features extracted by the proposed system and the manual segmentation of video recordings has shown an accuracy level consistent with the one reached by Aminian et al. in the original algorithm implementation. Also the error in spatial parameters (step/stride lengths/velocities) compared favorably with the results presented in the original literature. The kinematic parameters have been only validated by comparing the obtained measures with the usual ranges of motion/rotation of the considered body segments in healthy subjects. The result of the feature extraction procedure is a report, exportable in *pdf* and *html* formats, which summarize through a dashboard interface the motor performance achieved by the subject during the walking task. Screenshots of the result GUI are shown in Figure 4.3.

Although the achieved preliminary results were promising, the multi-sensor system was not further developed because of its complexity, which would have made it impractical for an actual use in clinical environments. For this reason, we focused on the single sensor solution described in the following.

## 4.4 Single-sensor System

A solution based on a single sensor has several advantages compared to one relying on multiple nodes: it is more practical, easy-to-use, and comfortable to wear for patients; it requires less set-up time and less data processing; it is suitable for

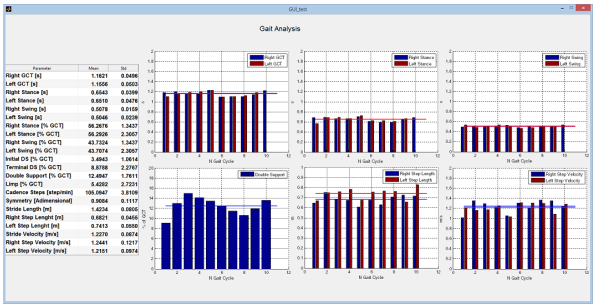


(a)

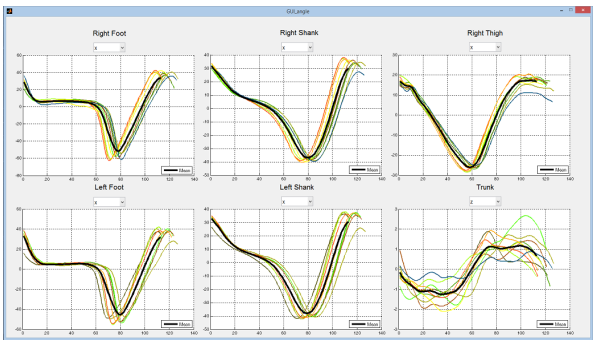


(b)

Figure 4.3: Screenshots of the GUI for the visualization of the GA results: (a) the summary of the spatio-temporal parameters; (b) the plots showing the inclinations of various body segments

applications in unconstrained environments, such as patients' home during daily living activities. On the other hand, the main drawbacks are: the loss of details (some features, such as the inclination of the body segments, cannot be computed) and accuracy (the system is more sensitive to noise and errors); an higher complexity of the algorithms used for features extraction (the relation between the raw signals and the parameters of interest is less intuitive). However, we believe that the positive aspects of a single-sensor system are more attractive than its limitations, motivating further investigations in this direction.

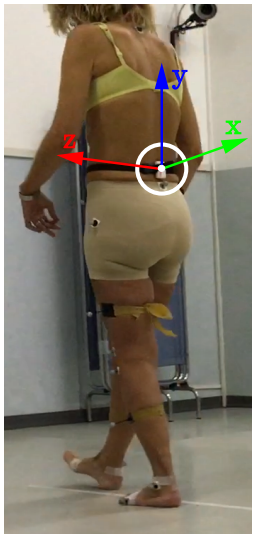


Figure 4.4: The considered acquisition testbed formed by a single wearable IMU, positioned in correspondence to the third lumbar vertebra—the alignment between sensor's axes and body reference system is also shown.

### 4.4.1 Experimental Set-up

#### Hardware

As for the multi-sensor configuration, the IMU used in single-node BSN is a Shimmer 3 device. The position of the sensor on the patient's body and the alignment between sensor's axes and body reference system are shown in Figure 4.4. For validation purposes, data from a multi-factorial mo-cap system (ELITE 2002, BTS Bioengineering, Italy, `http://www.btsbioengineering.com/`) are collected simultaneously to the inertial measures. The mocap system is formed by: 8 cameras, operating at 100 Hz, which are able to estimate the 3D position of reflective markers attached to a subject's body with a maximum error of 3 mm; and 2 force plates for the measurement of GRFs.

#### Subjects and acquisition procedure

The set of subjects considered in this study consists of 5 post-stroke patients with hemiparesis and 3 healthy controls. Although the selected hemiparetic individuals present different gait impairment levels, all of them were able to walk without assistive devices. The characteristics of both the test groups are detailed in Table 4.1.

Trial acquisitions have been carried out in a clinical GA laboratory at the "Maggiore della Carità" University Hospital, Novara (Italy). The IMU is fixed with a Velcro-strap belt in correspondence to the third lumbar vertebra (L3), as shown in Figure 4.4, trying to align the positive x, y, and z axes of the node's coordinate reference system to the left, upward, and forward directions, respectively. During tests, all subject are also equipped with 17 reflective markers placed on the lower limbs, in order to allow the optoelectronic mo-cap system to collect data for the validation procedure. Once the inertial sensor and the reflective markers are correctly placed on the subject's body, the actual acquisition procedure begins. In each trial, the subject, initially standing in a rest position, is asked by the examiner to start walking at a comfortable and self-selected speed and to stop just before the end of the walkway, whose length is approximately equal to 10 m. Multiple trials have been acquired for all subjects (except one), collecting a total of 16 trials (10 for hemiparetic and 6 for healthy individuals, respectively).

### 4.4.2 Gait Characterization

#### Temporal Parameters Estimation

In order to obtain the complete segmentation of gait phases, the accurate detection of the Heel Strike ($HS$) (i.e., the instant at which the foot touches the ground) and the Toe-off ($TO$) (i.e., the instant at which the foot leaves the ground) instants for both legs is required. We remark that, for hemiparetic gait, $HS$ and $TO$ events should be more generally intended as initial and terminal foot contacts, respectively, since the part of the foot in contact with the ground at the beginning and the end of a stance phase may differ from the heel and the toe. The $HS$/$TO$ notation is maintained for consistency with classical GA literature and with the notation used in the

Table 4.1: Subjects characteristics.

| | Sex | Age | Height | Hemiparetic Side | # of trials |
|---|---|---|---|---|---|
| Patient1 | F | 40 | 1.69 | Left | 1 |
| Patient2 | M | 66 | 1.73 | Right | 2 |
| Patient3 | M | 49 | 1.67 | Left | 2 |
| Patient4 | M | 58 | 1.68 | Left | 2 |
| Patient5 | F | 65 | 1.58 | Right | 3 |
| (Mean±std) | | 55.6±11.05 | 1.67±0.05 | - | - |
| Control1 | M | 28 | 1.81 | - | 2 |
| Control2 | M | 27 | 1.78 | - | 2 |
| Control3 | M | 42 | 1.74 | - | 2 |
| (Mean±std) | | 32.3±8.38 | 1.77±0.03 | - | - |

previous chapters. Hemiparetic gait patterns are usually highly asymmetric and exhibit large variability across subjects, since post-stroke patients use different strategies to achieve the goal of walking[112, 134]. For these reasons, the detection of the aforementioned events in hemiparetic GA is non-trivial and classical stride segmentation algorithms based on trunk-mounted IMU-sensors do not perform properly. The novel proposed approach aims at overcoming the limitations of the existing methods, providing accurate and robust estimation of temporal gait parameters for both hemiparetic and normal gaits. The steps of the new implemented algorithm are detailed in the following.

First of all, the 3-dimensional orientation of the sensor in the Earth frame is computed through the Madgwick's orientation filter [27] and a gravity compensation procedure is applied, thus obtaining the linear accelerations in both Earth and sensor coordinate frames. The resulting signals are initially analyzed in the frequency domain in order to extract some meaningful information related to the overall motor characteristics of the whole gait trial. In particular, the linear accelerations components, with reference to the sensor frame, in the vertical and frontal directions, denoted as $\boldsymbol{a}_{\mathrm{y}}$ and $\boldsymbol{a}_{\mathrm{z}}$, respectively, are considered. The medio-lateral component $\boldsymbol{a}_{\mathrm{x}}$ has been ignored because the experimental results have shown that it is not significantly related to the

actual gait performance of the tested subjects. These signals are preliminary low-pass filtered with a fourth-order zero-lag Butterworth filter with bandwidth equal to 8 Hz and properly processed in order to exclude initial and final acceleration/deceleration phases, which may introduce additional noise. The DFTs of the collected signals are computed using a FFT algorithm. For the signal $\boldsymbol{a}_{\mathrm{y}}$, with length in sample equal to N, the $k$-th component of the spectrum $\boldsymbol{X}_{a_{\mathrm{y}}} = \{X_{a_{\mathrm{y}}}(k)\}_{k=0}^{N-1}$ can be computed as follows:

$$X_{a_{\mathrm{y}}}(k) = \sum_{n=0}^{N-1} a_{\mathrm{y}}(n) e^{-jk\frac{2\pi}{N}n} \qquad k = 0, ..., N-1.$$

The corresponding amplitude spectrum, denoted as $\boldsymbol{X}_{\mathrm{ampl},a_{\mathrm{y}}}$, is:

$$\boldsymbol{X}_{\mathrm{ampl},a_{\mathrm{y}}} = |\boldsymbol{X}_{a_{\mathrm{y}}}|.$$

where $|\cdot|$ represents the magnitude of a complex number.

In the same way, the spectrum of the frontal accelerations ($\boldsymbol{X}_{a_{\mathrm{z}}} = \{X_{a_{\mathrm{z}}}(k)\}_{k=0}^{N-1}$) and its amplitude spectrum $\boldsymbol{X}_{\mathrm{ampl},a_{\mathrm{z}}} = \{|X_{a_{\mathrm{z}}}(k)|\}_{k=0}^{N-1}$ can be computed.

Illustrative amplitude spectra are shown in Figure 4.5 for both a healthy (control) subject and a post-stroke (hemiparetic) patient. It can be observed that, for hemiparetic individuals, the amplitude spectra are scattered across all the frequencies lower than 4 Hz, with two dominant peaks in correspondence to the stride ($f_{\mathrm{stride}}$) and the step ($f_{\mathrm{step}}$) frequencies, respectively. In the healthy subject case, instead, most of the spectra are concentrated around a single main peak, corresponding to the step frequency $f_{\mathrm{step}}$—the stride frequency is "hidden", owing to the good gait symmetry. In the post-stroke patient case, the low regularity of the walking patterns causes noisier and sparser spectra, whereas the asymmetry between paretic and non-paretic side steps leads to have two dominant periods, coinciding with step and stride cycles, respectively. In the healthy subject case, instead, the dominant periodicity coincides with the step cycle, since the regularity and the symmetry between right and left steps is very high.

As observed in Section 2.4.2 for the PD case, the gait's spectral characteristics can be translated into an intuitive feature, denoted as spectrum power $P$, representative of the "power" associated with a gait trial: the more symmetric and regular the

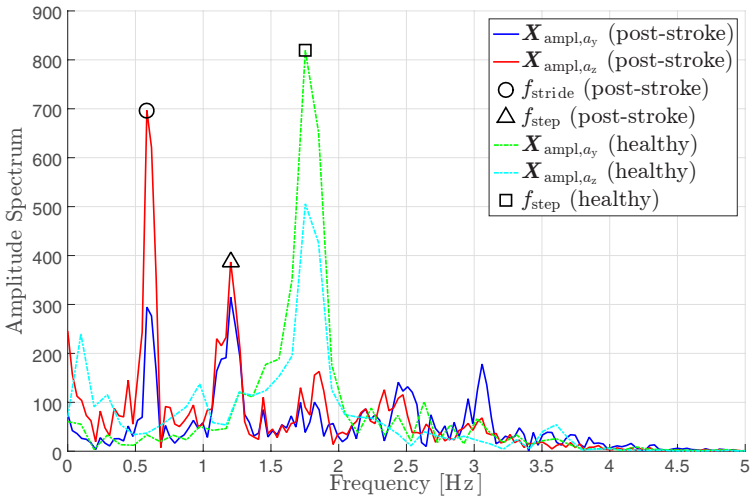


Figure 4.5: Amplitude spectra corresponding to the acceleration components $\boldsymbol{a}_{\text{y}}$ and $\boldsymbol{a}_{\text{z}}$ for both a post-stroke patient and a healthy subject. The step/stride frequencies are highlighted.

walking pattern, the "more powerful" the movement. For the signal $\boldsymbol{a}_{\text{y}}$ (acceleration in the vertical direction), the corresponding spectrum power $P_{\boldsymbol{a}_{\text{y}}}$ can be computed as follows:

$$P_{a_{\text{y}}} \triangleq \frac{1}{N}\sum_{k=0}^{N-1}(X_{\text{ampl},a_{\text{y}}}(k))^2.$$

Similarly, the spectrum power of the frontal acceleration $\boldsymbol{a}_{\text{z}}$, denoted as $P_{a_{\text{z}}}$, can be computed. Finally, we introduce the overall power $P_{\text{sum}}$, defined as: =

$$P_{\text{sum}} = P_{a_{\text{y}}} + P_{a_{\text{z}}}.$$

which takes into account the powers of frontal and the vertical components, i.e., it captures the "overall" gait power. This intuitive "feature" will be used in the next steps of the algorithm for the calibration of subject-dependent constants.

In many existing IMU-based algorithms for GA, the first phase consists in identifying, usually with peak detection the accelerometer and/or gyroscope signals, a first approximate region in correspondence to a $TO$ or $HS$ instant. Then, the search procedure is refined using smaller search intervals for accurate estimation of $HS$s and

*TO*s [59, 55]. In hemiparetic gait, the asymmetry, low cadence, and high variability across steps and subjects make even approximate step identification non-trivial.

The new method for step detection proposed in this work is based on a Simple Moving Average (SMA) with a dynamic and "power"-dependent window size. Initially, the Euclidean norm of the linear acceleration, denoted as $\boldsymbol{a}_{\text{norm}}$, is computed as follows:

$$a_{\text{norm}}(k) = \|a(k)\| = \sqrt{a_{\text{x}}^2(k) + a_{\text{y}}^2(k) + a_{\text{z}}^2(k)} \quad k = 0, ..., N-1.$$

The SMA is then calculated on the $\boldsymbol{a}_{\text{norm}}$ signal, considering a window with size (in terms of number of samples) $M$, which is automatically selected and dynamically updated per subject. In particular, the signal $\boldsymbol{a}_{\text{SMA}}$ is obtained using the following SMA:

$$a_{\text{SMA}}(k) = \begin{cases} \frac{1}{M}\sum_{m=0}^{M-1}\|a(k-m)\| & k \geqslant M \\ \frac{1}{k}\sum_{m=0}^{k-1}\|a(k-m)\| & 1 \leq k < M \end{cases} \tag{4.1}$$

The SMA window size $M$ is chosen subject-dependent in order to guarantee the adaptation of the algorithm to different walking patterns. For healthy subjects, a small window size is needed for detecting the sudden changes in the acceleration values due to high step cadence and signal magnitude. At the opposite, for increasing gait impairments levels, the window size $M$ should be larger to consider, as a single movement, the weak and irregular accelerations involved in the paretic-side leg progression. To make the selection of the value of $M$ automatic, we intuitively set the SMA window size as follows:

$$M = \left\lfloor \frac{P_{\text{ref}}}{P_{\text{sum}}} \cdot M_{\text{ref}} \right\rfloor \tag{4.2}$$

where $P_{\text{ref}}$ is a reference spectrum power value (corresponding to the average value of $P_{\text{sum}}$ for healthy subjects) and $M_{\text{ref}}$ is the window size used for healthy individuals. On the basis of the experimental trials, a value $M_{\text{ref}} = 12$ (corresponding to $\frac{12}{102.4 \text{ Hz}} \cong$ 120 ms) has been selected.

The signal $\boldsymbol{a}_{\text{SMA}}$ calculated with the proper window size is further processed in order to have zero mean and removing the high-frequency oscillations (low-pass filtering it with a fourth-order zero-lag Butterworth filter with cut-off frequency of 8

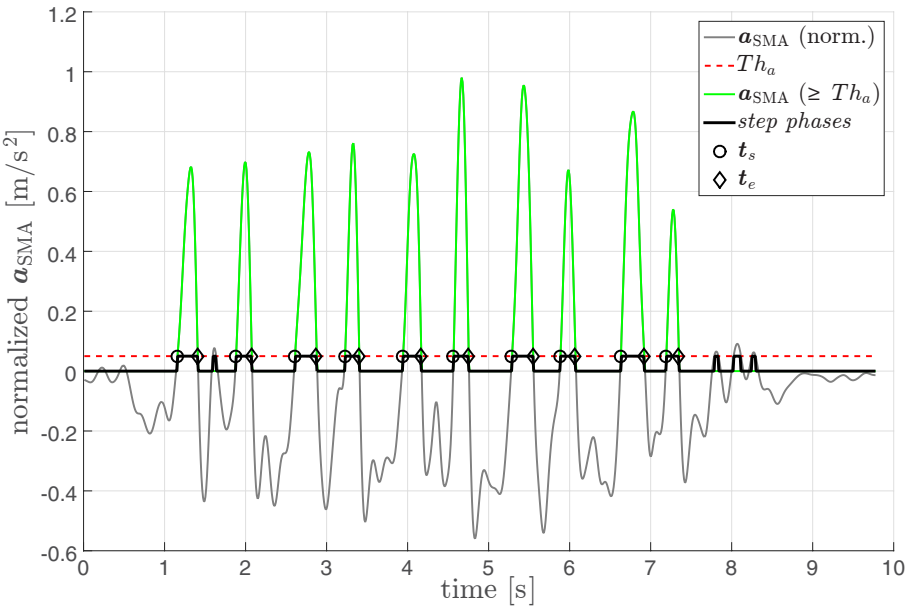


Figure 4.6: Normalized $\boldsymbol{a}_{\mathrm{SMA}}$ of a hemiparetic patient for the step detection procedure. The signal portions above $Th_a$, highlighted in green, identify candidate step phases. For each of them, the first and the last samples above the threshold are marked as $\boldsymbol{t}_s$ and $\boldsymbol{t}_e$, respectively. Candidate step phases with duration greater than $D_{\mathrm{min}}$ are considered as valid steps.

Hz). The resulting (normalized) $\boldsymbol{a}_{\mathrm{SMA}}$ signal is shown in Figure 4.6. When it is above a given threshold $Th_a$, empirically set equal to 0.05 m/s$^2$, a candidate *step phase* is identified. The starting and ending instants of the $N_{\mathrm{step}}$ detected step phases, denoted as $\boldsymbol{t}_s = \{t_s(i)\}_{i=1}^{N_{\mathrm{step}}}$ and $\boldsymbol{t}_e = \{t_e(i)\}_{i=1}^{N_{\mathrm{step}}}$, are set in correspondence to the first and the last samples above $Th_a$, respectively. The identified intervals with duration longer than $D_{\mathrm{min}} = 0.3$ s are considered as valid step phases; otherwise, they are discarded.

The next step of the algorithm consists in performing an accurate search of the *HS* and the *TO* instants inside the interval $[t_s(i), t_e(i)]$ defined for the $i$-th step phase ($i \in \{1, \ldots, N_{\mathrm{step}}\}$). In particular, the $i$-th *HS* is set in correspondence to a local maximum in the frontal acceleration $\boldsymbol{a}_z$, within the interval $[t_s(i) - 0.05\ \mathrm{s}, t_s(i) + 0.05\ \mathrm{s}]$. The intuition behind this assumption is the fact that $\boldsymbol{a}_{\mathrm{SMA}}$, being the result of the

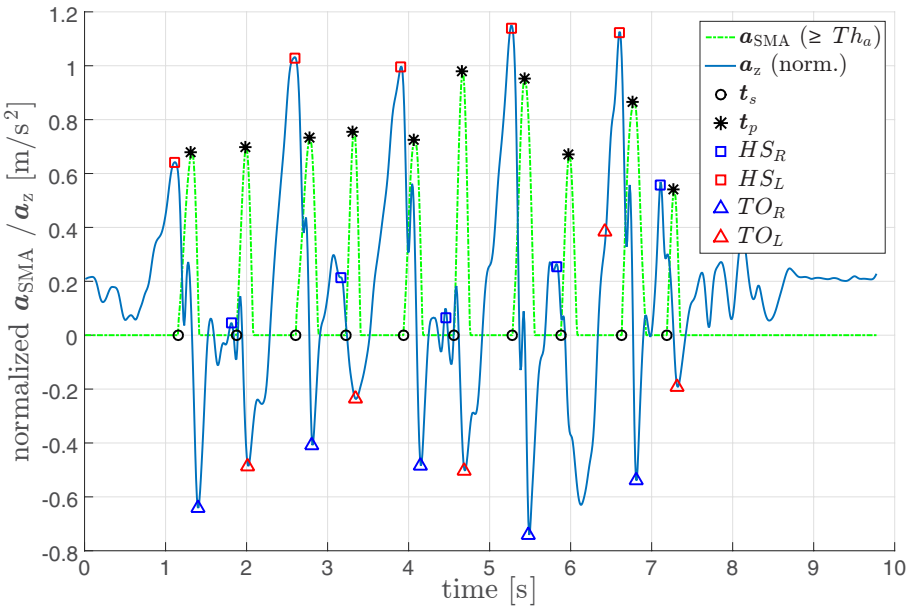


Figure 4.7: For each step phase detected through $\boldsymbol{a}_{\text{SMA}}$, a refined searching of $HS$ and $TO$ events is performed. In the frontal acceleration $\boldsymbol{a}_{\text{z}}$, $HS$s and $TO$s are searched in proximity of $\boldsymbol{t}_s$ and $\boldsymbol{t}_p$ instants, respectively. The identified events are then labeled as right and left considering the information provided by the medio-lateral acceleration $\boldsymbol{a}_{\text{x}}$.

SMA defined in (4.1), has local maxima shifted ahead by $M$ samples with respect to $\boldsymbol{a}_{\text{z}}$. When the magnitude of $\boldsymbol{a}_{\text{SMA}}$ starts increasing, it means that the Euclidean norm of the acceleration signal has increased in the window of the previous $M$ samples, because the body is accelerating forward and upward. After reaching a local maximum, denoted as $t_p(i)$, the magnitude of $\boldsymbol{a}_{\text{SMA}}$ starts decreasing, because the body has already entered the stationary phase of the gait (double support) and the acceleration components have reached local minima (just before the $TO$ instant). This observation motivates the search of the exact $TO$ instant in the region around $t_p(i)$. More precisely, $TO$s are searched in $\boldsymbol{a}_{\text{z}}$ and within the interval $[t_p(i) - 0.02 \text{ s}, t_p(i) + 0.08 \text{ s}]$. The identified fundamental instants are then labeled as right/left $HS$s and $TO$s considering the slope $m$ of the line passing through the projection of each consecutive

$(HS(i), TO(i))$ pair in the medio-lateral acceleration $\boldsymbol{a}_{\mathrm{x}}$. If $m < 0$, then a left gait cycle is starting, so that $HS(i)$ is labeled as a left $HS$ ($HS_L(i)$) and the contra-lateral $TO(i)$ as a right $TO$ ($TO_R(i)$); if $m > 0$, the instants are inversely labeled as $HS_R(i)$ and $TO_L(i)$. Once all the $HS$ and $TO$ instants have been identified, the gait parameters defined in Section 1.3.2, namely $GCT_{R/L}$, $ST_{R/L}$, $SW_{R/L}$, $IDS$, $TDS$, $DS$, and the step cadence $C_{step}$ can be computed.

### Spatial Parameters Estimation

Most of the scientific works which deal with IMU-based hemiparetic GA focus on the estimation of temporal features or provide simple and approximative spatial parameters information, e.g., by dividing the traveled distance by the total walking time [135, 123]. Accurate estimation of spatial parameters for hemiparetic gait, indeed, is a challenging task due to the asymmetric, irregular, and inconsistent walking patterns, especially when a single sensor mounted on the trunk is used.

Since double integration of acceleration is not a suitable solution, because of drift and measurement noise, we start considering two well known algorithms for step length estimation in symmetric gait with a single sensor attached on the trunk, which relate the vertical displacement/acceleration of the subject's Center Of Mass (COM) to the forward distance traversed at each step: (i) the "inverted pendulum model" method, described by Zijlstra et al. in [55]; and (ii) the Weinberg algorithm presented in [136].

As anticipated in Section 2.4.1, for each step cycle, the Zijlstra method relates the vertical displacement $h$ of the COM (approximated, for simplicity, with the movement of the sensor placed on the lower trunk) to the step length, denoted as $StepL$, according to the following equation:

$$StepL_z = K_z\sqrt{2\ell h - h^2} \tag{4.3}$$

where $\ell$ is the subject leg's length (dimension: [m]) and $K_z$ is an empirically calibrated constant (adimensional). The displacement $h$ can be obtained by double integrating and properly high-pass filtering the linear vertical acceleration $\boldsymbol{a}_{\mathrm{y}}$ on the limited time interval of a *step cycle*.

The Weinberg algorithm, on the other hand, is based on a similar intuition and empirically relates the trunk vertical acceleration with the step length according to the following equation:

$$StepL_w = K_w \sqrt[4]{a_{\mathrm{M}} - a_{\mathrm{m}}} \tag{4.4}$$

where $a_{\mathrm{M}}$ and $a_{\mathrm{m}}$ are the maximum and the minimum values of the low-pass filtered vertical acceleration $\boldsymbol{a}_{\mathrm{y}}$ and $K_w$ (dimension: $[\sqrt[4]{\mathrm{m}^3} \cdot \sqrt{\mathrm{s}}]$) is another subject-dependent constant expedient for calibration and unit conversion purposes. It can be observed that both Zijlstra and Weinberg algorithms need a manual calibration step (through $K_z$ and $K_w$, respectively) to fit the peculiar characteristics of the testing subject in order to correctly estimate the spatial parameters. Moreover, both of them assume gait to be symmetric: this is not the case in hemiparetic patients, so that these algorithms cannot be used. We thus propose modified versions of Zijlstra and Weinberg algorithms, which consider the typical characteristics of hemiparetic gait, i.e., asymmetry and irregularity, and automatically set the calibration constants in order to deal with the inter-patient variability.

In order to better characterize the individual condition of each patient and set up a consistent calibration constant for spatial parameters' estimation, in both the modified algorithms, the "power" $P$, introduced in Subsection 4.4.2, is considered as a concise parameter representative of the patient's walking impairment level. This value, together with the leg length $\ell$, allows to tune Zijlstra and Weinberg algorithms without the need of a manual and time-consuming calibration step. In particular, the Zijlstra formula is modified as follows, distinguishing between steps of the hemiparetic and the normal side, denoted as $StepL_{z,\mathrm{hem}}$ and $StepL_{z,\mathrm{nor}}$, respectively:

$$StepL_{z,\mathrm{hem}} = K_{z,\mathrm{hem}} \sqrt{2\ell h_{\mathrm{hem}} - h_{\mathrm{hem}}^2} \tag{4.5}$$

$$StepL_{z,\mathrm{nor}} = K_{z,\mathrm{nor}} \sqrt{2\ell h_{\mathrm{nor}} - h_{\mathrm{nor}}^2} \tag{4.6}$$

where: $K_{z,\mathrm{hem}}$ and $h_{\mathrm{hem}}$ are the calibration constant and the vertical displacement for paretic side steps, respectively; $K_{z,\mathrm{nor}}$ and $h_{\mathrm{nor}}$ are the same parameters for the non-paretic side steps. The following simple linear models are used to map the values of $P_{\mathrm{sum}}$ into the calibration constants introduced in (4.5) and (4.6):

$$K_{z,\text{hem}} = \alpha_{\text{hem}} \cdot \frac{P_{\text{ref}}}{P_{\text{sum}}} + \beta_{\text{hem}} \tag{4.7}$$

$$K_{z,\text{nor}} = \alpha_{\text{nor}} \cdot \frac{P_{\text{ref}}}{P_{\text{sum}}} + \beta_{\text{nor}} \tag{4.8}$$

where: the ratio between reference and subject's spectrum powers is the same defined in (4.2); and the linear models' coefficients ($\{\alpha_{\text{hem}}, \beta_{\text{hem}}\}$ and $\{\alpha_{\text{nor}}, \beta_{\text{nor}}\}$ for paretic and non-paretic sides, respectively) are empirically defined in a preliminary tuning phase (according to the experimental evidences) and remain fixed across all subjects. The choice behind these values is motivated by the intuition that the relationship between COM vertical and horizontal displacements, considering a step of the affected side, is weakened by the hemiparetic patients' tendency to rise the paretic-side hip during the swing phase, as a consequence of a compensatory movement needed to complete the forward progression[112]. This behavior introduces "noisy" COM vertical movements. Using a lower value of $K_z$ for the paretic side allows to reduce this phenomenon and to estimate more precisely, the step lengths of both sides.

For what concerns the extended version of the Weinberg algorithm, the only modification concerns the subject-dependent calibration constant, denoted as $K_{w,\text{mod}}$, which is automatically calculated with the following two-variable linear model, considering both $P_{\text{sum}}$ and the leg length $\ell$:

$$K_{w,\text{mod}} = \alpha_{w,P} \cdot \frac{P_{\text{ref}}}{P_{\text{sum}}} + \alpha_{w,\ell} \cdot \ell + \beta_w \tag{4.9}$$

where the model coefficients $\{\alpha_{w,P}, \alpha_{w,\ell}, \beta_w\}$, as for (4.7) and (4.8) cases, are empirically defined (just once) to achieve the best fit with the actual step lengths across different individuals. Once all the step lengths have been computed with the proposed modified Zijlstra and Weinberg algorithms, stride lengths ($StrideL_{R/L}$) and velocities ($StrideV_{R/L}$) can be easily calculated.

### 4.4.3 Results

The performance evaluation of the prosed algorithms is carried out comparing the gait spatio-temporal parameters, calculated through the reference optoelectronic system,

Table 4.2: Temporal parameters estimation results.

| | Post Stroke patients | | | Healthy Subjects | | |
|---|---|---|---|---|---|---|
| Feature [dimension] | Mean±Std | RMSE | $R$ | Mean±Std | RMSE | $R$ |
| $P_{\text{sum}}$ [adim.] | $2352 \pm 717$ | - | - | $3858 \pm 278$ | - | - |
| $M$ [samples] | $22.8 \pm 6.47$ | - | - | $15.5 \pm 3.44$ | - | - |
| $GCT_R$ [s] | $1.45 \pm 0.11$ | 0.03 | 0.97 | $1.27 \pm 0.19$ | 0.02 | 0.99 |
| $GCT_L$ [s] | $1.47 \pm 0.13$ | 0.04 | 0.96 | $1.30 \pm 0.21$ | 0.02 | 1.00 |
| $ST_R$ [% of GCT] | $69.3 \pm 7.2$ | 2.60 | 0.97 | $63.2 \pm 1.6$ | 2.02 | 0.99 |
| $ST_L$ [% of GCT] | $67.8 \pm 6.7$ | 2.89 | 0.94 | $64.1 \pm 2.4$ | 1.91 | 0.99 |
| $SW_R$ [% of GCT] | $30.7 \pm 7.2$ | 2.60 | 0.94 | $36.8 \pm 1.6$ | 2.02 | 0.90 |
| $SW_L$ [% of GCT] | $32.2 \pm 6.7$ | 2.89 | 0.92 | $35.9 \pm 2.4$ | 1.91 | 0.93 |
| $IDS$ [% of GCT] | $18.9 \pm 3.5$ | 4.02 | 0.57 | $13.1 \pm 1.5$ | 1.25 | 0.92 |
| $TDS$ [% of GCT] | $18.5 \pm 3.5$ | 3.74 | 0.64 | $14.9 \pm 3.1$ | 1.97 | 0.94 |
| $DS$ [% of GCT] | $37.4 \pm 4.4$ | 4.01 | 0.80 | $28.2 \pm 4.2$ | 2.48 | 0.96 |
| $C_{step}$ [steps/min] | $82.1 \pm 5.6$ | 1.02 | 0.99 | $98.3 \pm 11.8$ | 0.63 | 1.00 |

with those estimated by the IMU-based approaches. The Root Mean Square Error (RMSE) and the Pearson's correlation coefficient, denoted as $R$, between the features measured with the two methods are considered as performance metrics.

In Table 4.2, the main results, in terms of *temporal parameters*' estimation, obtained with the proposed algorithm are shown. In the first two rows, the average values of the main parameters used in the initial step detection procedure, namely $P_{\text{sum}}$ and the SMA window size $M$, are shown, for both post-stroke and healthy subjects. Is it possible to observe that the average $P_{\text{sum}}$ in healthy subjects is considerably higher than in hemiparetic patients, highlighting the effectiveness of this concise parameter in representing the overall level of gait impairments. The temporal parameter values (mean±standard deviation), estimated using the power-dependent SMA window size, are shown in the lower part of Table 4.2, together with the performance metrics RMSE and $R$. As expected, the estimated hemiparetic gait characteristics reflect irregular and asymmetric walking patterns, according to the clinical observations. Post-stroke subjects, indeed, show higher $GCT$, $ST$, and $DS$ values and significantly lower step cadence than controls. Moreover, single patient analyses, which are not

Table 4.3: Spatial parameters estimation results.

| | Post Stroke patients | | | Healthy Subjects | | |
|---|---|---|---|---|---|---|
| Feature [dimension] | Mean±Std | RMSE | $R$ | Mean±Std | RMSE | $R$ |
| $K_{z,\text{hem}}$ | $0.66 \pm 0.08$ | - | - | - | - | - |
| $K_{z,\text{nor}}$ | $0.87 \pm 0.12$ | - | - | - | - | - |
| $K_{w,\text{mod}}$ | $0.25 \pm 0.04$ | - | - | $0.47 \pm 0.04$ | - | - |
| $StepL_{z,R}$ [m] | $0.32 \pm 0.08$ | 0.03 | 0.92 | - | - | - |
| $StepL_{z,L}$ [m] | $0.35 \pm 0.08$ | 0.03 | 0.93 | - | - | - |
| $StepL_{w,R}$ [m] | $0.33 \pm 0.09$ | 0.04 | 0.89 | $0.69 \pm 0.07$ | 0.05 | 0.81 |
| $StepL_{w,L}$ [m] | $0.34 \pm 0.08$ | 0.04 | 0.91 | $0.70 \pm 0.06$ | 0.06 | 0.82 |
| $StrideV_{z,R}$ [m/s] | $0.45 \pm 0.12$ | 0.03 | 0.97 | - | - | - |
| $StrideV_{z,L}$ [m/s] | $0.43 \pm 0.10$ | 0.03 | 0.95 | - | - | - |
| $StrideV_{w,R}$ [m/s] | $0.46 \pm 0.13$ | 0.03 | 0.97 | $1.12 \pm 0.22$ | 0.08 | 0.98 |
| $StrideV_{w,L}$ [m/s] | $0.43 \pm 0.11$ | 0.03 | 0.95 | $1.06 \pm 0.22$ | 0.07 | 0.98 |

shown here, highlight a consistent increasing in the non-paretic limb *ST* feature, as a consequence of the gait asymmetry [112]. Comparing the performance of the proposed system with that of the BTS mo-cap system, the RMSE ranges between 20 ms and 40 ms for the *GCT*, from 1.25% to 4.02% of the GCT for stride phase parameters, and it is approximately equal to 1 step/min for the step cadence feature. The correlation coefficient between reference and estimated features' values is very high ($R > 0.90$) for all the parameters, except those of post-stroke patients' double support phases (namely, *IDS*, *TDS*, and *DS*), which range from 0.5 to 0.8.

For what concerns the *spatial parameters*, we first present the coefficients' values of the linear models used for the calibration constants' automatic computation, as described in Subsection 4.4.2. For the modified Zijlstra algorithm, the values of $K_{z,\text{hem}}$ in (4.7) are obtained with $\alpha_{\text{hem}} = -0.04$ and $\beta_{\text{hem}} = 0.75$, whereas $K_{z,\text{nor}}$ in (4.8) is computed using $\alpha_{\text{nor}} = -0.085$ and $\beta_{\text{nor}} = 1.03$. The two-variable linear regression model (4.9) used for computing $K_{w,\text{mod}}$ in both post-stroke and healthy subjects uses the following coefficients: $\alpha_{w,P} = 0.006$, $\alpha_{w,\ell} = 2.31$, and $\beta_w = -1.85$. In the first two rows of Table 4.3, the average values of the proposed step length estimators' calibration constants are shown. In the remaining rows of Table 4.3, step length and stride

velocity values, computed using the modified versions of both Zijlstra and Weinberg algorithms, are shown. As reported by several clinic studies [134], step/stride length and velocity are crucial features to assess the walking ability level of post-stroke individuals. It can be observed, in fact, that the average value of all the hemiparetic features is approximately doubled in healthy subjects. For post-stroke patients, the RMSEs of $StepL$ and $StrideV$ are around 3 cm and 3 cm/s, respectively, considering both the modified Zijlstra and Weinberg algorithms. For the healthy group of subjects, the asymmetric version of Zijlstra step length estimator is not applicable, since their gait patterns are symmetric, whereas the $StepL$ and $StrideV$ RMSEs obtained using the modified Weinberg method are approximately equal to 5 cm and 7 cm/s, respectively. As for the temporal parameters, the correlation coefficient values is very high ($R \geq 0.89$) for all the spatial features of both groups, except for the $StepL_{w,R/L}$ values of healthy subjects, for which the correlation coefficient is slightly lower (around 0.82).

The high correlation between reference and estimated spatio-temporal parameters is clearly shown in Figure 4.8. Most of the points, whose $(x,y)$ coordinates are the values measured by the optoelectronic and the IMU-based systems, respectively, are located near the dotted diagonal line, which represents the ideal case with perfect correlation. As previously remarked, $DS$ for post-stroke patients and $StepL_w$ for healthy subjects are the parameters which show the lowest correlations with the corresponding reference values. This is due to the fact that, in hemiparetic individuals the detection of the actual $TO$ instants can be missed in some cases, anticipating or delaying it of a few tens of milliseconds. At the opposite, for the healthy subjects the regression model for the computation of $K_w$ is slightly polarized toward the correct estimation of step lengths in the hemiparetic case, reducing the accuracy for normal walking subjects.

Finally, an overall view on the accuracy achieved by the proposed methods is given in Figure 4.9, visualizing with box plots the characteristics (median, quartiles and extreme values) of the most relevant estimated spatio-temporal parameters and comparing them with the features extracted from the reference mo-cap system – both post-stroke and healthy subjects' values are included in the computation of each box

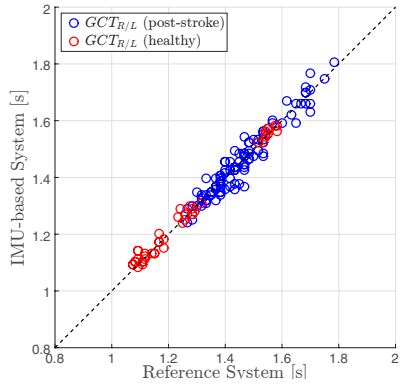


(a) *GCT*

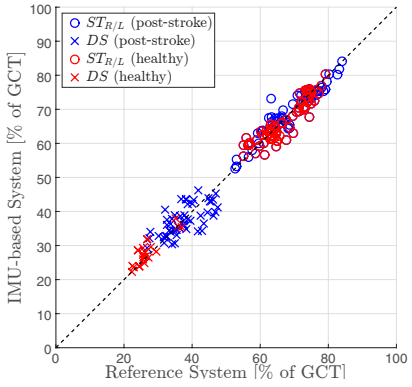


(b) *ST* and *DS*

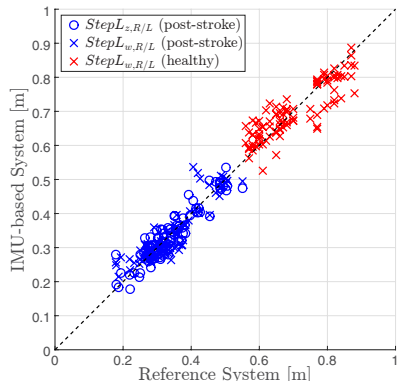


(c) *StepL*

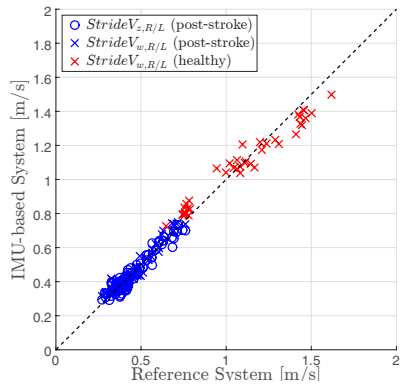


(d) *StrideV*

Figure 4.8: Comparison between features values calculated through the optoelectronic reference system and those estimated with the proposed IMU-based methods for post-stroke (red markers) and healthy (blue markers) subjects: (a) *GCT*, (b) *ST* and *DS*, (c) *StepL*, and (d) *StrideV*.

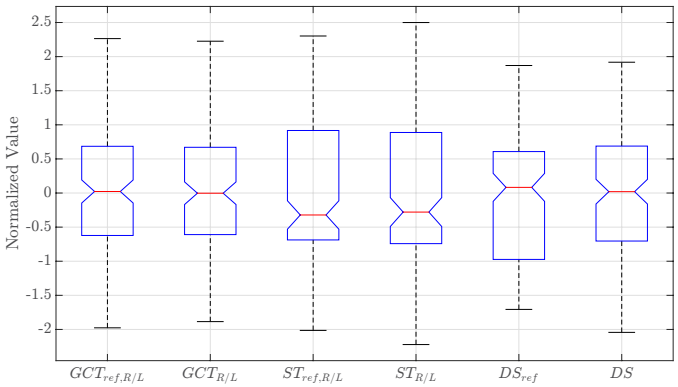


(a) Temporal parameters

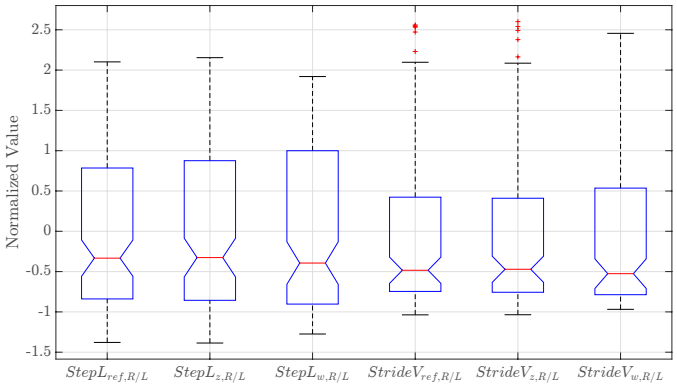


(b) Spatial parameters

Figure 4.9: Boxplots of some representative (a) temporal and (b) spatial parameters.

plot. Once again, it can be observed that the similarity between reference and estimated values is very high, with a slight decreasing in accuracy only for *DS* ans $StepL_w$ features.

The obtained results in both temporal and spatial parameters extraction are consistent with other works in the literature focused on hemiparetic GA of post-stroke patients [135, 123]. Moreover, the achieved accuracy compares favorably with other general-purpose IMU-based GA algorithms, for both pathological and normal walking assessment [59, 55].

## 4.5 Conclusion

In this chapter, we proposed two inertial BSN methods for quantitative GA in post-stroke patients. The first preliminary solution, based on a multi-sensor BSN, has been implemented. It is capable to provide accurate and detailed information for the characterization of gait but, due to its complexity and low practicality, its development has been interrupted. The second approach, based on a single wearable IMU placed on the lower trunk, has led to the implementation of a low-cost system for accurate estimation of gait spatio-temporal parameters, suitable for both post-stroke and healthy subjects. In this context, a novel algorithm for temporal parameter computation, which relies on automatically set subject-dependent calibration constants to overcome the inter-individual variability, has been implemented. Similarly, two variations of well-known step length estimation algorithms have been proposed, in order to deal with the asymmetry and irregularity typical of hemiparetic gait. The comparison between estimated parameters and gait features extracted through a reference mo-cap system has shown a very good overall accuracy (with correlation coefficient $R > 0.9$ for almost all the considered features) of the proposed methods for both hemiparetic patients and controls. The results obtained for the single-sensor version are promising and the low-complexity of the proposed approach makes it a suitable solution for achieving inexpensive quantitative characterization of both healthy and hemiparetic gait. This system could be useful both in clinics, helping physicians to obtain a more objective and accurate assessment of patients' impairment levels, and

in free living environments, enabling a long-term monitoring of their motor capabilities during every-day life. In both cases, the proposed approach represents a valuable solution for providing more detailed and up-to-date information to the medical personnel, thus, enhancing the effectiveness of rehabilitation strategies.

### 4.5.1 Future Work

Undoubtedly, the results presented so far are still preliminary and further investigations are needed to confirm their robustness and validity. Performing additional test on a larger and more heterogeneous set of subjects would led to more meaningful results from a statistical point of view. Additionally, investigating the possibility to link kinematic features to clinical evaluation scales, in a way similar to the one described in Chapter 2 and Chapter 3 for the PD case, with the aim to implement, through machine learning techniques, a system for the automatic evaluation of motor performance, would add more value to the proposed approach. For example, clinical rating scales, such as the Functional Ambulation Category (FAC) the Gait Deviation Index (GDI), or the Wisconsin Gait Scale (WGS), used for the assessment of pos-stroke patients motor/gait capabilities, might be taken into account for the development of an automatic classifier of gait performance. Finally, future works will also investigate the possibility to implement the proposed methods on commercially available devices, such as wearables and smartphones.

# Bibliography

[1] F. Parisi, G. Ferrari, M. Giuberti, L. Contin, V. Cimolin, C. Azzaro, G. Albani, and A. Mauro, "Low-complexity inertial sensor-based characterization of the UPDRS score in the gait task of Parkinsonians," in *Proceedings of the 9th International Conference on Body Area Networks*, pp. 69–75, ICST (Institute for Computer Sciences, Social-Informatics and Telecommunications Engineering), 2014.

[2] F. Parisi, G. Ferrari, V. Cimolin, M. Giuberti, C. Azzaro, G. Albani, L. Contin, and A. Mauro, "On the correlation between UPDRS scoring in the leg agility, sit-to-stand, and gait tasks for parkinsonians," in *Wearable and Implantable Body Sensor Networks (BSN), 2015 IEEE 12th International Conference on*, pp. 1–6, 2015.

[3] F. Parisi, G. Ferrari, M. Giuberti, L. Contin, V. Cimolin, C. Azzaro, G. Albani, and A. Mauro, "Inertial BSN-based Characterization and Automatic UPDRS Evaluation of the Gait Task of Parkinsonians," *IEEE Transactions on Affective Computing*, vol. 7, no. 3, pp. 258–271, 2016.

[4] F. Parisi, G. Ferrari, M. Giuberti, L. Contin, V. Cimolin, C. Azzaro, G. Albani, and A. Mauro, "Body-Sensor-Network-Based Kinematic Characterization and Comparative Outlook of UPDRS Scoring in Leg Agility, Sit-to-Stand, and Gait Tasks in Parkinson's Disease," *IEEE journal of biomedical and health informatics*, vol. 19, no. 6, pp. 1777–1793, 2015.

[5] F. Parisi, G. Ferrari, A. Baricich, M. D'Innocenzo, C. Cisari, and A. Mauro, "Accurate gait analysis in post-stroke patients using a single inertial measurement unit," in *Wearable and Implantable Body Sensor Networks (BSN), 2016 IEEE 13th International Conference on*, pp. 335–340, 2016.

[6] G. A. Borelli, J. Bernoulli, N. Elinger, and C. J. a Jesu, *De motu animalium*. Apud Petrum Gosse, 1743.

[7] A. Wong, "Low-cost visual/inertial hybrid motion capture system for wireless 3d controllers," 2007.

[8] Y. Tao, H. Hu, and H. Zhou, "Integration of vision and inertial sensors for 3d arm motion tracking in home-based rehabilitation," *The International Journal of Robotics Research*, vol. 26, no. 6, pp. 607–624, 2007.

[9] C. Joguet, D. David, and Y. Caritu, "Pen-like, natural graphic gesture capture disposal, based on a microsystem," in *Proc. of Smart Objects Conference SOC'03, Grenoble, France*, Citeseer, 2003.

[10] I. Skog and P. Händel, "A low-cost gps aided inertial navigation system for vehicle applications," in *Signal Processing Conference, 2005 13th European*, pp. 1–4, 2005.

[11] M. Brodie, A. Walmsley, and W. Page, "Fusion motion capture: a prototype system using inertial measurement units and gps for the biomechanical analysis of ski racing," *Sports Technology*, vol. 1, no. 1, pp. 17–28, 2008.

[12] E. R. Bachmann, "Inertial and magnetic tracking of limb segment orientation for inserting humans into synthetic environments," tech. rep., DTIC Document, 2000.

[13] E. Foxlin, M. Harrington, and G. Pfeifer, "Constellation: a wide-range wireless motion-tracking system for augmented reality and virtual set applications," in *Proceedings of the 25th annual conference on Computer graphics and interactive techniques*, pp. 371–378, ACM, 1998.

[14] I. W. Griffiths, *Principles of biomechanics & motion analysis*. Lippincott Williams & Wilkins, 2006.

[15] D. Beard, R. Soundarapandian, J. O'connor, and C. Dodd, "Gait and electromyographic analysis of anterior cruciate ligament deficient subjects," *Gait & Posture*, vol. 4, no. 2, pp. 83–88, 1996.

[16] B. T. Cole, S. H. Roy, C. J. De Luca, and S. H. Nawab, "Dynamical learning and tracking of tremor and dyskinesia from wearable sensors," *IEEE Transactions on Neural Systems and Rehabilitation Engineering*, vol. 22, no. 5, pp. 982–991, 2014.

[17] K. Maenaka, "Mems inertial sensors and their applications," in *Networked Sensing Systems, 2008. INSS 2008. 5th International Conference on*, pp. 71–73, 2008.

[18] J. E. Lenz, "A review of magnetic sensors," *Proceedings of the IEEE*, vol. 78, no. 6, pp. 973–989, 1990.

[19] R. E. Kalman, "A new approach to linear filtering and prediction problems," *Journal of basic Engineering*, vol. 82, no. 1, pp. 35–45, 1960.

[20] A. M. Sabatini, "Quaternion-based extended kalman filter for determining orientation by inertial and magnetic sensing," *IEEE Transactions on Biomedical Engineering*, vol. 53, no. 7, pp. 1346–1356, 2006.

[21] J. L. Marins, X. Yun, E. R. Bachmann, R. B. McGhee, and M. J. Zyda, "An extended kalman filter for quaternion-based orientation estimation using marg sensors," in *Intelligent Robots and Systems, 2001. Proceedings. 2001 IEEE/RSJ International Conference on*, vol. 4, pp. 2003–2011, 2001.

[22] E. Kraft, "A quaternion-based unscented kalman filter for orientation tracking," in *Proceedings of the Sixth International Conference of Information Fusion*, vol. 1, pp. 47–54, 2003.

[23] H. J. Luinge and P. H. Veltink, "Measuring orientation of human body segments using miniature gyroscopes and accelerometers," *Medical and Biological Engineering and computing*, vol. 43, no. 2, pp. 273–282, 2005.

[24] N. Yadav and C. Bleakley, "Accurate orientation estimation using ahrs under conditions of magnetic distortion," *Sensors*, vol. 14, no. 11, pp. 20008–20024, 2014.

[25] Y. Tian, H. Wei, and J. Tan, "An adaptive-gain complementary filter for real-time human motion tracking with marg sensors in free-living environments," *IEEE Transactions on Neural Systems and Rehabilitation Engineering*, vol. 21, no. 2, pp. 254–264, 2013.

[26] L. Ojeda and J. Borenstein, "Flexnav: Fuzzy logic expert rule-based position estimation for mobile robots on rugged terrain," in *Robotics and Automation, 2002. Proceedings. ICRA'02. IEEE International Conference on*, vol. 1, pp. 317–322, 2002.

[27] S. O. H. Madgwick, "An efficient orientation filter for inertial and inertial/magnetic sensor arrays," tech. rep., Department of Mechanical Engineering, University of Bristol, Bristol, UK, 2010.

[28] A. Burns, B. R. Greene, M. J. McGrath, T. J. O'Shea, B. Kuris, S. M. Ayer, F. Stroiescu, and V. Cionca, "SHIMMER - a wireless sensor platform for noninvasive biomedical research," *IEEE Sensors Journal*, vol. 10, no. 9, pp. 1527–1534, 2010.

[29] M. Schulze, T. Calliess, M. Gietzelt, K. Wolf, T. Liu, F. Seehaus, R. Bocklage, H. Windhagen, and M. Marschollek, "Development and clinical validation of an unobtrusive ambulatory knee function monitoring system with inertial 9dof sensors," in *2012 Annual International Conference of the IEEE Engineering in Medicine and Biology Society*, pp. 1968–1971, 2012.

[30] M. Giuberti, G. Ferrari, L. Contin, V. Cimolin, C. Azzaro, G. Albani, and A. Mauro, "Assigning UPDRS Scores in the Leg Agility Task of Parkinsoni-

ans: Can It Be Done through BSN-based Kinematic Variables?," *IEEE Internet of Things Journal*, vol. 2, no. 1, pp. 41–51, 2015.

[31] D. Roetenberg, C. T. Baten, and P. H. Veltink, "Estimating body segment orientation by applying inertial and magnetic sensing near ferromagnetic materials," *IEEE Transactions on Neural Systems and Rehabilitation Engineering*, vol. 15, no. 3, pp. 469–471, 2007.

[32] L. Peppoloni, A. Filippeschi, E. Ruffaldi, and C. A. Avizzano, "A novel 7 degrees of freedom model for upper limb kinematic reconstruction based on wearable sensors," in *2013 IEEE 11th international symposium on intelligent systems and informatics (SISY)*, pp. 105–110, 2013.

[33] D. Álvarez, J. C. Alvarez, R. C. González, and A. M. López, "Ambulatory human upper limb joint motion monitoring," in *Instrumentation and Measurement Technology Conference (I2MTC), 2012 IEEE International*, pp. 15–19, 2012.

[34] A. G. Cutti, A. Giovanardi, L. Rocchi, A. Davalli, and R. Sacchetti, "Ambulatory measurement of shoulder and elbow kinematics through inertial and magnetic sensors," *Medical & biological engineering & computing*, vol. 46, no. 2, pp. 169–178, 2008.

[35] R. E. Mayagoitia, A. V. Nene, and P. H. Veltink, "Accelerometer and rate gyroscope measurement of kinematics: an inexpensive alternative to optical motion analysis systems," *Journal of biomechanics*, vol. 35, no. 4, pp. 537–542, 2002.

[36] P. Picerno, A. Cereatti, and A. Cappozzo, "Joint kinematics estimate using wearable inertial and magnetic sensing modules," *Gait & posture*, vol. 28, no. 4, pp. 588–595, 2008.

[37] E. Charry, M. Umer, and S. Taylor, "Design and validation of an ambulatory inertial system for 3-d measurements of low back movements," in *Intelligent Sensors, Sensor Networks and Information Processing (ISSNIP), 2011 Seventh International Conference on*, pp. 58–63, 2011.

[38] A. Plamondon, A. Delisle, C. Larue, D. Brouillette, D. McFadden, P. Desjardins, and C. Larivière, "Evaluation of a hybrid system for three-dimensional measurement of trunk posture in motion," *Applied Ergonomics*, vol. 38, no. 6, pp. 697–712, 2007.

[39] N. Sim, C. Gavriel, W. W. Abbott, and A. A. Faisal, "The head mouse–Head gaze estimation "In-the-Wild" with low-cost inertial sensors for BMI use," in *Neural Engineering (NER), 2013 6th International IEEE/EMBS Conference on*, pp. 735–738, 2013.

[40] S. Reinfelder, R. Hauer, J. Barth, J. Klucken, and B. M. Eskofier, "Timed up-and-go phase segmentation in parkinson's disease patients using unobtrusive inertial sensors," in *2015 37th Annual International Conference of the IEEE Engineering in Medicine and Biology Society (EMBC)*, pp. 5171–5174, 2015.

[41] J. D. Hoffman and J. McNames, "Objective measure of upper extremity motor impairment in parkinson's disease with inertial sensors," in *2011 Annual international conference of the IEEE engineering in medicine and biology society*, pp. 4378–4381, 2011.

[42] X. Jia, N. Duroseau, V. Chan, C. Ciraco, R. Wang, S. M. Nia, K. Ho, J. P. Govindavari, F. Delgosha, T. Chan, *et al.*, "Objective quantification of upper extremity motor functions in unified parkinson's disease rating scale test," in *2014 36th Annual International Conference of the IEEE Engineering in Medicine and Biology Society*, pp. 5345–5348, 2014.

[43] A. Parnandi, E. Wade, and M. Matarić, "Motor function assessment using wearable inertial sensors," in *2010 Annual International Conference of the IEEE Engineering in Medicine and Biology*, pp. 86–89, 2010.

[44] I. Carpinella, D. Cattaneo, and M. Ferrarin, "Quantitative assessment of upper limb motor function in multiple sclerosis using an instrumented action research arm test," *Journal of neuroengineering and rehabilitation*, vol. 11, no. 1, p. 1, 2014.

[45] G. Rigas, A. T. Tzallas, M. G. Tsipouras, P. Bougia, E. E. Tripoliti, D. Baga, D. I. Fotiadis, S. G. Tsouli, and S. Konitsiotis, "Assessment of tremor activity in the parkinson's disease using a set of wearable sensors," *IEEE Transactions on Information Technology in Biomedicine*, vol. 16, no. 3, pp. 478–487, 2012.

[46] S. I. Lee, J.-F. Daneault, F. N. Golabchi, S. Patel, S. Paganoni, L. Shih, and P. Bonato, "A novel method for assessing the severity of levodopa-induced dyskinesia using wearable sensors," in *2015 37th Annual International Conference of the IEEE Engineering in Medicine and Biology Society (EMBC)*, pp. 8087–8090, 2015.

[47] J. Cancela, M. Pansera, M. Arredondo, J. Estrada, M. Pastorino, L. Pastor-Sanz, and J. Villalar, "A comprehensive motor symptom monitoring and management system: the bradykinesia case," in *2010 Annual International Conference of the IEEE Engineering in Medicine and Biology*, pp. 1008–1011, 2010.

[48] B. T. Cole, S. H. Roy, and S. H. Nawab, "Detecting freezing-of-gait during unscripted and unconstrained activity," in *2011 Annual International Conference of the IEEE Engineering in Medicine and Biology Society*, pp. 5649–5652, 2011.

[49] W. Tao, T. Liu, R. Zheng, and H. Feng, "Gait analysis using wearable sensors," *Sensors*, vol. 12, no. 2, pp. 2255–2283, 2012.

[50] A. Ferrari, M. G. Benedetti, E. Pavan, C. Frigo, D. Bettinelli, P. Rabuffetti, P. Crenna, and A. Leardini, "Quantitative comparison of five current protocols in gait analysis," *Gait & Posture*, vol. 28, no. 2, pp. 207–216, 2008.

[51] W. Zijlstra, A. W. Rutgers, and T. W. V. Weerden, "Voluntary and involuntary adaptation of gait in Parkinson's disease," *Gait & Posture*, vol. 7, no. 1, pp. 53–63, 1998.

[52] D. H. Sutherland, "The evolution of clinical gait analysis part l: kinesiological emg," *Gait & posture*, vol. 14, no. 1, pp. 61–70, 2001.

[53] S. Chien, S. Lin, C., C. Liang, Y. Soong, S. Lin, Y. Hsin, C. Lee, and S. Chen, "The efficacy of quantitative gait analysis by the GAITRite system in evaluation of parkinsonian bradykinesia," *Parkinsonism and related disorders*, vol. 12, no. 7, pp. 438–42, 2006.

[54] K. Aminian, B. Najafi, K. Rezakhanlou, E. D. Andres, C. Fritsch, and P. Robert, "Temporal feature estimation during walking using miniature accelerometers: an analysis of gait improvement after hip arthroplasty," *Medical & biological engineering & computing*, vol. 37, no. 6, pp. 686–91, 1999.

[55] W. Zijlstra and A. L. Hof, "Assessment of spatio-temporal gait parameters from trunk accelerations during human walking," *Gait & Posture*, vol. 18, no. 2, pp. 1–10, 2003.

[56] A. Köse, A. Cereatti, and U. Della Croce, "Bilateral step length estimation using a single inertial measurement unit attached to the pelvis," *Journal of neuroengineering and rehabilitation*, vol. 9, pp. 1–9, 2012.

[57] S. Miyazaki, "Long-term unrestrained measurement of stride length and walking velocity utilizing a piezoelectric gyroscope," *IEEE transactions on biomedical engineering*, vol. 44, no. 8, pp. 753–9, 1997.

[58] K. Tong and M. H. Granat, "A practical gait analysis system using gyroscopes," *Medical Engineering & Physics*, vol. 21, no. 2, pp. 87–94, 1999.

[59] K. Aminian, B. Najafi, C. Büla, P. F. Leyvraz, and P. Robert, "Spatio-temporal parameters of gait measured by an ambulatory system using miniature gyroscopes," *Journal of Biomechanics*, vol. 35, no. 5, pp. 689–699, 2002.

[60] J. Barth, C. Oberndorfer, P. Kugler, D. Schuldhaus, J. Winkler, J. Klucken, and B. Eskofier, "Subsequence dynamic time warping as a method for robust step segmentation using gyroscope signals of daily life activities," in *2013 35th Annual International Conference of the IEEE Engineering in Medicine and Biology Society (EMBC)*, pp. 6744–6747, 2013.

[61] A. M. Sabatini, C. Martelloni, S. Scapellato, and F. Cavallo, "Assessment of walking features from foot inertial sensing," *IEEE Trans. on Biomedical Eng.*, vol. 52, no. 3, pp. 486–94, 2005.

[62] J. M. Jasiewicz, J. H. J. Allum, J. W. Middleton, A. Barriskill, P. Condie, B. Purcell, and R. C. T. Li, "Gait event detection using linear accelerometers or angular velocity transducers in able-bodied and spinal-cord injured individuals.," *Gait & posture*, vol. 24, no. 4, pp. 502–9, 2006.

[63] S. Sprager and M. B. Juric, "Inertial sensor-based gait recognition: a review," *Sensors*, vol. 15, no. 9, pp. 22089–22127, 2015.

[64] P. Esser, H. Dawes, J. Collett, M. G. Feltham, and K. Howells, "Assessment of spatio-temporal gait parameters using inertial measurement units in neurological populations," *Gait & posture*, vol. 34, no. 4, pp. 558–560, 2011.

[65] A. Tura, M. Raggi, L. Rocchi, A. G. Cutti, and L. Chiari, "Gait symmetry and regularity in transfemoral amputees assessed by trunk accelerations," *Journal of neuroengineering and rehabilitation*, vol. 7, no. 1, p. 1, 2010.

[66] M. D. Djurić-Jovičić, N. S. Jovičić, and D. B. Popović, "Kinematics of gait: new method for angle estimation based on accelerometers," *Sensors*, vol. 11, no. 11, pp. 10571–10585, 2011.

[67] X. Li, H. Xu, and J. T. Cheung, "Gait-force model and inertial measurement unit-based measurements: A new approach for gait analysis and balance monitoring," *Journal of Exercise Science & Fitness*, vol. 14, no. 2, pp. 60–66, 2016.

[68] A. Salarian, H. Russmann, C. Wider, P. R. Burkhard, F. J. Vingerhoets, and K. Aminian, "Quantification of tremor and bradykinesia in parkinson's disease using a novel ambulatory monitoring system," *IEEE Transactions on Biomedical Engineering*, vol. 54, no. 2, pp. 313–322, 2007.

[69] J. Bussmann, Y. Van de Laar, M. Neeleman, and H. Stam, "Ambulatory accelerometry to quantify motor behaviour in patients after failed back surgery: a validation study," *Pain*, vol. 74, no. 2, pp. 153–161, 1998.

[70] D. M. Karantonis, M. R. Narayanan, M. Mathie, N. H. Lovell, and B. G. Celler, "Implementation of a real-time human movement classifier using a triaxial accelerometer for ambulatory monitoring," *IEEE transactions on information technology in biomedicine*, vol. 10, no. 1, pp. 156–167, 2006.

[71] O. Amft and G. Tröster, "Recognition of dietary activity events using on-body sensors," *Artificial intelligence in medicine*, vol. 42, no. 2, pp. 121–136, 2008.

[72] Q. Li, J. A. Stankovic, M. A. Hanson, A. T. Barth, J. Lach, and G. Zhou, "Accurate, fast fall detection using gyroscopes and accelerometer-derived posture information," in *2009 Sixth International Workshop on Wearable and Implantable Body Sensor Networks*, pp. 138–143, 2009.

[73] J. Chen, K. Kwong, D. Chang, J. Luk, and R. Bajcsy, "Wearable sensors for reliable fall detection," in *Engineering in Medicine and Biology Society*, pp. 3551–3554, 2005.

[74] F. Bianchi, S. J. Redmond, M. R. Narayanan, S. Cerutti, and N. H. Lovell, "Barometric pressure and triaxial accelerometry-based falls event detection," *IEEE Transactions on Neural Systems and Rehabilitation Engineering*, vol. 18, no. 6, pp. 619–627, 2010.

[75] C.-C. Yang and Y.-L. Hsu, "A review of accelerometry-based wearable motion detectors for physical activity monitoring," *Sensors*, vol. 10, no. 8, pp. 7772–7788, 2010.

[76] L. M. de Lau and M. Breteler, "Epidemiology of Parkinson's disease," *Lancet Neurology*, vol. 5, no. 6, pp. 525–535, 2006.

[77] A. Priyadarshi, S. A. Khuder, E. A. Schaub, and S. S. Priyadarshi, "Environmental risk factors and parkinson's disease: a metaanalysis," *Environmental research*, vol. 86, no. 2, pp. 122–127, 2001.

[78] W. Satake, Y. Nakabayashi, I. Mizuta, Y. Hirota, C. Ito, M. Kubo, T. Kawaguchi, T. Tsunoda, M. Watanabe, A. Takeda, *et al.*, "Genome-wide

association study identifies common variants at four loci as genetic risk factors for parkinson's disease," *Nature genetics*, vol. 41, no. 12, pp. 1303–1307, 2009.

[79] C. G. Goetz, S. Fahn, P. Martinez-Martin, W. Poewe, C. Sampaio, G. T. Stebbins, M. B. Stern, B. C. Tilley, R. Dodel, B. Dubois, R. Holloway, J. Jankovic, J. Kulisevsky, A. E. Lang, A. Lees, S. Leurgans, P. A. LeWitt, D. Nyenhuis, C. W. Olanow, O. Rascol, A. Schrag, J. A. Teresi, J. J. V. Hilten, and N. LaPelle, "Movement disorder society-sponsored revision of the Unified Parkinson's Disease Rating Scale (MDS-UPDRS): Process, format, and clinimetric testing plan," *Movement Disorders*, vol. 22, no. 1, pp. 41–47, 2007.

[80] B. Post, M. P. Merkus, R. M. .de Bie, R. J. Haan, and J. D. Speelman, "Unified Parkinson's Disease Rating Scale motor examination: are ratings of nurses, residents in neurology, and movement disorders specialists interchangeable?," *Movement Disorders*, vol. 20, no. 12, pp. 1577–1584, 2005.

[81] J. E. Ahlskog and R. J. Uitti, "Rasagiline, parkinson neuroprotection, and delayed-start trials," *Neurology*, vol. 74, pp. 197–203, 2010.

[82] K. Kieburtz, "Issues in neuroprotection clinical trials in parkinson's disease," *Neurology*, vol. 66, pp. 550–557, 2006.

[83] R. A. Hauser, F. Deckers, and P. Lehert, "Parkinson's disease home diary: further validation and implications for clinical trials," *Movement Disorders*, vol. 19, pp. 1409–1413, 2004.

[84] A. Salarian, H. Russmann, F. J. G. Vingerhoets, C. Dehollain, Y. Blanc, P. R. Burkhard, and K. Aminian, "Gait assessment in Parkinson's Disease: Toward an ambulatory system for long-term monitoring," *IEEE Trans. on Biomedical Eng.*, vol. 51, no. 8, pp. 1434–1443, 2004.

[85] J. Cancela, M. Pastorino, M. T. Arredondo, M. Pansera, L. Pastor-Sanz, F. Villagra, M. A. Pastor, and A. P. Gonzalez, "Gait assessment in parkinson's disease patients through a network of wearable accelerometers in unsupervised

environments," in *2011 Annual International Conference of the IEEE Engineering in Medicine and Biology Society*, pp. 2233–2236, 2011.

[86] B. Mariani, M. C. Jiménez, F. J. Vingerhoets, and K. Aminian, "On-shoe wearable sensors for gait and turning assessment of patients with parkinson's disease," *IEEE transactions on biomedical engineering*, vol. 60, no. 1, pp. 155–158, 2013.

[87] J. Klucken, J. Barth, P. Kugler, J. Schlachetzki, T. Henze, F. Marxreiter, Z. Kohl, R. Steidl, J. Hornegger, B. Eskofier, *et al.*, "Unbiased and mobile gait analysis detects motor impairment in parkinson's disease," *PloS one*, vol. 8, no. 2, p. e56956, 2013.

[88] S. R. Hundza, W. R. Hook, C. R. Harris, S. V. Mahajan, P. A. Leslie, C. A. Spani, L. G. Spalteholz, B. J. Birch, D. T. Commandeur, and N. J. Livingston, "Accurate and reliable gait cycle detection in parkinson's disease," *IEEE Transactions on Neural Systems and Rehabilitation Engineering*, vol. 22, no. 1, pp. 127–137, 2014.

[89] S. T. Moore, H. G. MacDougall, J.-M. Gracies, H. S. Cohen, and W. G. Ondo, "Long-term monitoring of gait in parkinson's disease," *Gait & posture*, vol. 26, no. 2, pp. 200–207, 2007.

[90] D. Alvarez, R. C. González, A. López, and J. C. Alvarez, "Comparison of step length estimators from weareable accelerometer devices," in *Engineering in Medicine and Biology Society, 2006. EMBS'06. 28th Annual International Conference of the IEEE*, pp. 5964–5967, 2006.

[91] A. Delval, J. Salleron, J. Bourriez, S. Bleuse, C. Moreau, P. Krystkowiak, L. Defebvre, P. Devos, and A. Duhamel, "Kinematic angular parameters in PD: Reliability of joint angle curves and comparison with healthy subjects," *Gait & Posture*, vol. 28, no. 3, pp. 495–501, 2008.

[92] R. Moe-Nilssen and J. L. Helbostad, "Estimation of gait cycle characteristics by trunk accelerometry," *Journal of Biomechanics*, vol. 37, no. 1, pp. 121–126, 2004.

[93] G. N. Lewis, W. D. Byblow, and S. E. Walt, "Stride length regulation in Parkinson's disease: the use of extrinsic, visual cues," *Brain*, vol. 123, no. 10, pp. 2077–90, 2000.

[94] M. Švehlík, E. B. Zwick, G. Steinwender, W. E. Linhart, P. Schwingenschuh, P. Katschnig, E. Ott, and C. Enzinger, "Gait analysis in patients with parkinson's disease off dopaminergic therapy," *Archives of Physical Medicine and Rehabilitation*, vol. 90, no. 11, pp. 1880 – 1886, 2009.

[95] R. O. Duda, P. E. Hart, and D. G. Stork, *Pattern Classification and Scene Analysis. 2nd edition*. New York, NY, USA: Wiley-Interscience, 2000.

[96] M. Giuberti, G. Ferrari, L. Contin, V. Cimolin, C. Azzaro, G. Albani, and A. Mauro, "Automatic UPDRS Evaluation in the Sit-to-Stand Task of Parkinsonians: Kinematic Analysis and Comparative Outlook on the Leg Agility Task," *IEEE Journal of Biomedical and Health Informatics*, vol. 19, no. 3, pp. 803–814, 2015.

[97] D. Giansanti, G. Maccioni, F. Benvenuti, and V. Macellari, "Inertial measurement units furnish accurate trunk trajectory reconstruction of the sit-to-stand manoeuvre in healthy subjects," *Medical and Biological Eng. and Comput.*, vol. 45, no. 10, pp. 969–976, 2007.

[98] S. Patel, K. Lorincz, R. Hughes, N. Huggins, J. Growdon, D. Standaert, M. Akay, J. Dy, M. Welsh, and P. Bonato, "Monitoring motor fluctuations in patients with Parkinson's Disease using wearable sensors," *IEEE Transactions on Information Technology in Biomedicine*, vol. 13, no. 6, pp. 864–873, 2009.

[99] D. A. Heldman, D. E. Filipkowski, D. E. Riley, C. M. Whitney, B. L. Walter, S. A. Gunzler, J. P.Giuffrida, and T. O. Mera, "Automated motion sensor

quantification of gait and lower extremity bradykinesia," in *Proc. of the 34th Annual Int. Conf. of the IEEE Eng. in Medicine and Biology Society* (EMBS), (San Diego, CA, USA), pp. 1956–1959, 2012.

[100] S. Das, L. Trutoiu, A. Murai, D. Alcindor, M. Oh, F. D. la Torre, and J. Hodgins, "Quantitative measurement of motor symptoms in Parkinson's disease: A study with full-body motion capture data," in *Proc. of the 2011 Annual Int. Conf. of the Engineering in Medicine and Biology Society* (EMBC), pp. 6789–6792, 2011.

[101] S. Nuzik, R. Lamb, A. Vansant, and S. Hirt, "Sit-to-stand movement pattern. a kinematic study," *Physical Therapy*, vol. 66, no. 11, pp. 1708–1713, 1986.

[102] J. Song, B. Fisher, G. Petzinger, A. Wu, J. Gordon, and G. J. Salem, "The relationships between the unified parkinson's disease rating scale and lower extremity functional performance in persons with early-stage parkinson's disease," *Neurorehabilitation and neural repair*, vol. 23, no. 7, pp. 657–661, 2009.

[103] J. Stochl, A. Boomsma, E. Ruzicka, H. Brozova, and P. Blahus, "On the structure of motor symptoms of parkinson's disease," *Movement Disorders*, vol. 23, no. 9, pp. 1307–1312, 2008.

[104] S. D. Vassar, Y. M. Bordelon, R. D. Hays, N. Diaz, R. Rausch, C. Mao, and B. G. Vickrey, "Confirmatory Factor Analysis of the Motor Unified Parkinson's Disease Rating Scale," *Parkinson's Disease*, vol. 2012, 2012. ArticleID 719167, 10 pages.

[105] J. Stamatakis, J. Ambroise, J. Crémers, H. Sharei, V. Delvaux, B. Macq, and G. Garraux, "Finger tapping clinimetric score prediction in parkinson's disease using low-cost accelerometers," *Computational intelligence and neuroscience*, vol. 2013, p. 1, 2013.

[106] R. A. Fisher, *Statistical Methods for Research Workers*. Edinburgh: Oliver and Boyd, 1925.

[107] K. J. Brusse, S. Zimdars, K. R. Zalewski, and T. M. Steffen, "Testing functional performance in people with Parkinson disease," *Physical Therapy*, vol. 85, pp. 134–141, 2005.

[108] "Telecom Italia: Sanitá Digitale." `http://nuvolaitaliana.impresasemplice.it/digitalizzazione/sanit%C3%A0-digitale`.

[109] "Qualcomm Life: 2net Platform." `http://www.qualcommlife.com/wireless-health`.

[110] World Health Organization, "The 10 leading causes of death in the world, 2012." `http://www.who.int/mediacentre/factsheets/fs310`.

[111] G. A. Donnan, M. Fisher, M. Macleod, and S. M. Davis, "Stroke," *The Lancet*, vol. 371, no. 9624, pp. 1612 – 1623, 2008.

[112] S. J. Olney and C. Richards, "Hemiparetic gait following stroke. Part I: Characteristics," *Gait & Posture*, vol. 4, no. 2, pp. 136–148, 1996.

[113] Auri Bruno-Petrina, "Motor Recovery In Stroke," 2016. `http://emedicine.medscape.com/article/324386-overview#showall`.

[114] J. E. Harris and J. J. Eng, "Goal priorities identified through client-centred measurement in individuals with chronic stroke," *Physiotherapy Canada. Physiotherapie Canada*, vol. 56, no. 3, p. 171, 2004.

[115] H. Zhou and H. Hu, "Inertial motion tracking of human arm movements in stroke rehabilitation," in *IEEE International Conference Mechatronics and Automation, 2005*, vol. 3, pp. 1306–1311, 2005.

[116] M. Zhang, B. Lange, C.-Y. Chang, A. A. Sawchuk, and A. A. Rizzo, "Beyond the standard clinical rating scales: fine-grained assessment of post-stroke

motor functionality using wearable inertial sensors," in *2012 Annual International Conference of the IEEE Engineering in Medicine and Biology Society*, pp. 6111–6115, 2012.

[117] B. Klaassen, P. Bartels, B. van Beijnum, and H. Hermens, "The development and evaluation of an arm usage coach for stroke survivors," in *2015 9th International Conference on Sensing Technology (ICST)*, pp. 514–519, 2015.

[118] T. Schauer, T. Seel, *et al.*, "Alignment-free, self-calibrating elbow angles measurement using inertial sensors," in *2016 IEEE-EMBS International Conference on Biomedical and Health Informatics (BHI)*, pp. 583–586, 2016.

[119] R. Martinez-Mendez, M. Sekine, and T. Tamura, "Detection of anticipatory postural adjustments prior to gait initiation using inertial wearable sensors," *Journal of neuroengineering and rehabilitation*, vol. 8, no. 1, p. 1, 2011.

[120] J. Boudarham, N. Roche, D. Pradon, C. Bonnyaud, D. Bensmail, and R. Zory, "Variations in kinematics during clinical gait analysis in stroke patients," *PloS one*, vol. 8, no. 6, p. e66421, 2013.

[121] M. A. Sharaf, M. A. Arafa, and H. A. Shaker, "Optoelectronic analysis of knee motions during gait in stroke patients," *Bulletin of Faculty of Physical Therapy*, vol. 13, no. 1, 2008.

[122] L. Bensoussan, S. Mesure, J.-M. Viton, and A. Delarque, "Kinematic and kinetic asymmetries in hemiplegic patients'gait initiation patterns," *Journal of Rehabilitation Medicine*, vol. 38, no. 5, pp. 287–294, 2006.

[123] P. Lopez-Meyer, G. D. Fulk, and E. S. Sazonov, "Automatic detection of temporal gait parameters in poststroke individuals," *Information Technology in Biomedicine, IEEE Transactions on*, vol. 15, no. 4, pp. 594–601, 2011.

[124] G. Chen, C. Patten, D. H. Kothari, and F. E. Zajac, "Gait differences between individuals with post-stroke hemiparesis and non-disabled controls at matched speeds," *Gait & posture*, vol. 22, no. 1, pp. 51–56, 2005.

[125] A. M. Howell, T. Kobayashi, H. A. Hayes, K. B. Foreman, and S. J. M. Bamberg, "Kinetic gait analysis using a low-cost insole," *IEEE Transactions on Biomedical Engineering*, vol. 60, no. 12, pp. 3284–3290, 2013.

[126] L.-y. Qin, H. Ma, and W.-H. Liao, "Insole plantar pressure systems in the gait analysis of post-stroke rehabilitation," in *Information and Automation, 2015 IEEE International Conference on*, pp. 1784–1789, 2015.

[127] T. Hester, D. M. Sherrill, M. Hamel, K. Perreault, P. Boissy, and P. Bonato, "Identification of tasks performed by stroke patients using a mobility assistive device," in *Engineering in Medicine and Biology Society, 2006. EMBS'06. 28th Annual International Conference of the IEEE*, pp. 1501–1504, 2006.

[128] A. Pizzi, G. Carlucci, C. Falsini, F. Lunghi, S. Verdesca, and A. Grippo, "Gait in hemiplegia: evaluation of clinical features with the wisconsin gait scale," *Journal of rehabilitation medicine*, vol. 39, no. 2, pp. 170–174, 2007.

[129] J. Cox, Y. Cao, G. Chen, J. He, and D. Xiao, "Smartphone-based walking speed estimation for stroke mitigation," in *Multimedia (ISM), 2014 IEEE International Symposium on*, pp. 328–332, 2014.

[130] Q. Fang, Z. Zhang, and Y. Tu, "Application of gait analysis for hemiplegic patients using six-axis wearable inertia sensors," in *Industrial Electronics Society, IECON 2014-40th Annual Conference of the IEEE*, pp. 3993–3996, 2014.

[131] C. Mizuike, S. Ohgi, and S. Morita, "Analysis of stroke patient walking dynamics using a tri-axial accelerometer," *Gait & posture*, vol. 30, no. 1, pp. 60–64, 2009.

[132] S. Yang, J.-T. Zhang, A. C. Novak, B. Brouwer, and Q. Li, "Estimation of spatio-temporal parameters for post-stroke hemiparetic gait using inertial sensors," *Gait & posture*, vol. 37, no. 3, pp. 354–358, 2013.

[133] X. Xu, M. Batalin, Y. Wang, and W. Kaiser, "Gait quality evaluation method for post-stroke patients," in *2012 IEEE International Conference on Acoustics, Speech and Signal Processing (ICASSP)*, pp. 613–616, 2012.

[134] C. M. Kim and J. J. Eng, "Magnitude and pattern of 3d kinematic and kinetic gait profiles in persons with stroke: relationship to walking speed," *Gait & posture*, vol. 20, no. 2, pp. 140–146, 2004.

[135] H.-K. Lee, S.-J. Hwang, S.-P. Cho, D.-R. Lee, S.-H. You, K.-J. Lee, Y.-H. Kim, and H.-S. Choi, "Novel algorithm for the hemiplegic gait evaluation using a single 3-axis accelerometer," in *Engineering in Medicine and Biology Society, 2009. EMBC 2009. Annual International Conference of the IEEE*, pp. 3964–3966, 2009.

[136] H. Weinberg, "Using the adxl202 in pedometer and personal navigation applications," *Analog Devices AN-602 application note*, vol. 2, no. 2, pp. 1–6, 2002.

# Acknowledgments

The end of another cycle.

Beginning with elementary, middle,and high school.Later on to my Bachelor's and Master's degrees. Then finally my Ph.D. Cherishing different moments of life but inside the same story. For years aiming for just one important goal in front of you and then all the sudden, when you achieve it, you feel lost; the past is just a memory, the future is unknown. It takes a while but not that long to realize that you're just entering another cycle, a bigger one or perhaps you realize that life is interchangeable and not interrupted. That familiar sensation knocks at your door again and brings a smile to your face. You feel motivated again, strong, self-confident and eager because you have another goal to achieve, another mission to complete. All cycles have a beginning and an end, goals change, time passes but two things will always remain the same:that is your passion for the things you do and the love for the people around you.

This is why, at the end of this important chapter of my life that is coming to an end while I am standing on the threshold of a new one, I want to express all my gratitude to all the people that never left my side up to this moment.

First of all, I want to thank you:Mom and Dad, for everything. It's really difficult to express with words how thankful and appreciative I am for all you do. I can just say that I'm deeply grateful for giving me everything, all I ever needed and I will always need from you. I'm not talking about the material things, which count a little, but about authentic values, support, and love, things that you cannot buy. I'm really proud of you and I hope I made you proud as well.

Thanks to Erica, Elena, and Dalila. No one would ever think that growing up with three sisters can be such a unique and amazing experience. Going through all these cycles, with you by my side has made it much easier and funnier. I couldn't ask for anything better than this amazing sibling relationship we have. I love you.

I thank all my (humongus) family. We are far in distance but close at heart, we are loud but we know how to listen to one another, we are good at arguing but even better at restoring harmony and peace within the union of our family. But above all, we are what a real, united, family is all about, which is being there for each other every step of the way.

Thanks to all my true friends. The old and the new ones. Those near to me and those far away. Thanks to Ale, Fab, Marco, Alle, Leo, Davide, and all the others. As the proverb says: "who finds a friend finds a treasure". I feel like the richest person in the world having all of you surrounding me.

A huge "thank you!" to the girls and the guys who shared with me the last three years at the WASNLAB (or IoTLab, boh?). I would have called you colleagues three years ago but now you are like a family to me.

Thanks to all the people involved in the VRehab project. Working with you has been incredibly interesting, motivating, and instructive.

I know that usually saying "I thank my advisor" is just a formality but, in this case, I'm sincerely grateful for my mentor, Gian. Thank you for believing so much in me since the very beginning and for giving the opportunity to achieve such high leveled goals. Even though they cost me a few white hair and the constant lack of sleep. Nevertheless, it was fully worth it.

I want to dedicate a few words to the wonderful people I've met in the last months in this amazing experience in Boston. Thanks to the guys and the girls of the Motion Analysis Lab. You made my American adventure even more exceptional and enjoyable. I would say "Fancy". :)

A special thought to the Irving boys, Luca&JLu. Thank you! I never expected to find such awesome roommates, or I should better say, new friends. You made me feel at home, when my actual home was further away than ever. You made these months unforgettable. See you soon!

I would also like to express my sincere gratitude for Karl and Paolo. Thank you for your support and for giving me the chance to be in the center of the scientific world and to grow further as a scientist and as a person.

Thank you all! For real!

Now I'm ready...let the next cycle begin.